Towards Molecular Control and Rational Design of Molecules with Enhanced Entangled Two-Photon Absorption

by

Leslie Nicole Upton

A dissertation submitted in partial fulfillment
of the requirements of the degree of
Doctor of Philosophy
(Applied Physics)
in The University of Michigan
2015

Doctoral Committee:

Professor Theodore G. Goodson, III, Chair
Professor Paul R. Berman
Professor Eitan Geva
Professor Jennifer P. Ogilvie
Professor Herbert G. Winful

2015

Dedication

To my parents…for all you are and have done for me. I am here because of you.

Acknowledgements

I thank my parents, my adviser, my committee, my cohort and my friends for this would not be possible without your support, encouragement and the knowledge that you have imparted to me.

Table of Contents

List of Figures

List of Tables

List of Appendices

Abstract

We utilize entangled photons to carry out nonlinear optical spectroscopy in organic molecules with an extremely small number of photons. While much research has been devoted to utilizing quantum mechanics and quantum entanglement in areas of quantum computing, quantum information science and quantum cryptography, the goal of this research is to exploit quantum entanglement in the area of spectroscopy. One unique feature that is observed when using such non-classical fields to carry out multi-photon absorption is the *s*electivity of the entangled photon absorption process. It is found that while some molecules may not have strong classical nonlinear optical properties, due to their excitation pathways, these same excitation pathways may enhance the entangled photon processes. It is found that the opposite is also true. It is proposed that molecules that absorb via a virtual state pathway absorb entangled photons and those that absorb via a change in permanent dipole do not. A modified equation for calculating the entangled two-photon absorption cross-section is derived. Using this modified equation we calculate and compare the entangled two-photon absorption cross-section of both homo and hetero-nuclear diatomic molecules. We hope this comparison expands upon previous theoretical work in the area of entangled two-photon absorption and provides more insight into the absorption mechanisms of non-classical fields.

Chapter 1

Introduction

1.1 Scope of Dissertation

In the areas of physics, material science and chemistry there are many unanswered questions that require diverse solutions and new experimental methods. Solutions such as developing novel materials and new methods to study these materials are required. Researchers now more than ever are realizing the necessity of establishing creative ways to combine well-established fields of study in new and novel ways. One such method for tackling these questions is through bridging the fields of organic material science and quantum optics. This combination places an emphasis on utilizing and harnessing the power of non-classical fields with the enhanced optical properties of large conjugated organic molecules.

The following dissertation focuses on the details of the proposed experimental and theoretical analysis of multi-photon absorption, specifically conducting two-photon absorption (TPA) experiments, with entangled photon pairs. These non-classical fields are used to carry out low intensity nonlinear spectroscopy and may provide new insights into the role of virtual states in the field of entangled two-photon absorption (ETPA). Studying such non-linear optical effects using non-classical sources (entangled photons) generated by spontaneous parametric down-conversion could provide more insight into the intermediate/virtual states which mediate absorption in molecules and other excited state dynamics and may lead to possible applications of this novel technology. Future

work may lie in developing virtual state spectroscopy to study/probe virtual states of novel organic molecules.

The foundation of this work is based on current and previous experimental and theoretical research data in the Goodson group [1-3] and theoretical work from the Saleh and Teich [4] and Kojima and Nguyen [5]. This dissertation primarily focuses on the comparison and characterization of classical two-photon absorption (TPA) and non-classical entangled two-photon absorption (ETPA). This detailed analysis and thorough comparison of classical and non-classical nonlinear optical effects are important to fundamental scientific research and applications. This dissertation also seeks to connect work across various fields and sub-disciplines to produce a body of work that provides a more complete and cohesive integration of the work completed on classical and non-classical radiative processes.

This introduction begins with an overview of the work in classical multiphoton spectroscopy and the development of materials with large two-photon absorption cross sections, particularly the development of novel conjugated organic molecules. Next, the theoretical and experimental uses of non-classical fields to execute multiphoton interactions are explored. I will highlight the work previously completed in this group and finally highlight the gaps in the research and what will be covered in this dissertation.

To begin, the counter classical properties of quantum mechanics have baffled scientists since Plank's discovery of energy quanta [6]. In particular, while quantum mechanics seemed experimentally sound and provided experimental evidence for many quantized phenomena, the idea that these quantities exist as probabilities did not sit well with many [7]. In fact, Einstein was once quoted as saying, “Quantum mechanics is

certainly imposing. But an inner voice tells me that it is not yet the real thing. The theory says a lot, but does not really bring us any closer to the secret of the "old one." I, at any rate, am convinced that He does not throw dice [8].” Thus Einstein sought to prove the incompleteness of quantum theory in the seminal EPR paper [9]. However since, John Bell's mathematical proof that causality and locality [10] are incompatible with quantum theory with the development of Bell’s inequalities and the experimental proof of these inequalities by Clauser, Horne and Shimony [11] and also by Alain Aspect [12], many have sought to understand and harness the unique properties of entangled systems [13]. The advent of the laser made many of these experiments much more practical to carry out experimentally.

While the underlying physics of entanglement is still very counterintuitive, the concept is experimentally verifiable [12, 14]. Since the first cascade experiments and the first tests of Bell’s inequalities, the field has blossomed to include cold atom research, atomic ions, and nonlinear optics. Entanglement is now utilized quantum computing, quantum information science and quantum biology [15-17]. Thus the field of quantum optics is well-established. There are still and despite experiments that still seek to exploit loopholes in Bell’s inequalities. However, entanglement, while still not completely understood, has become a well-studied and often utilized phenomenon in quantum optics.

Despite all the work utilizing entangled systems, very little work has focused on studying and characterizing the non-classical light matter interactions in large, organic macromolecules or molecules in general. The Goodson lab has been at the forefront of studying large conjugated molecules with an emphasis on maximizing the NLO response in these molecules. Much of the work has focused on characterizing the charge transfer

characteristics and dynamics of these large molecules with multiple ultrafast techniques, such as two-photon excited fluorescence, transient absorption, single photon counting and fluorescence upconversion. This work is at the forefront of studying the effects of increased conjugation on optical properties as a function of increased number of chromophore units linearly and multi-dimensionally. As the number of units increases a cooperative enhancement effect has been shown [18, 19], yet at a certain point this enhancement effect levels off and the addition of additional units results in no further enhancement. Our group's use of ultrafast laser spectroscopic techniques allows us to study and determine structure/matter optical property relations. Many of these molecules exhibit very large NLO response and are good candidates for uses in organic photovoltaics, nonlinear microscopy and optical limiting applications. Materials with large two-photon responses will be the basis for this study of non-classical light matter interactions. We will explore the entangled two-photon pair absorption in these molecules with large two-photon absorption cross-sections.

However, such studies present several challenges. The first and perhaps the most challenging issue is that completing these studies one must know what states are excited and what types of fields those states are excited with. While large conjugated molecules do have large nonlinear responses and should therefore exhibit a large entangled two-photon response, their use presents several challenges. Unlike atomic states, large organic molecules do not have well defined energy levels and the levels can be very broad. The properties of these molecules aren't well characterized either. Most of the research devoted to these molecules is to in fact determine these properties. Also in terms of characterization, one must also characterize the non-classical fields used to carry

out these experiments, as well. What types of statistics describe these fields? Are the photons entangled? How entangled are the photons? Preparing and prepping these sensitive entangled states can be quite tedious and time consuming, but it is necessary if one is to truly gain any insight from these nonlassical light matter interaction studies. Other challenges include the low input fluxes of entangled photons generated by spontaneous parametric down conversion, which make the experimental detection of absorption from non-classical sources difficult.

This work makes a significant contribution to the field because it takes all these issues into consideration and broadens the field with both experiment and theoretical results. Because the field is very small, much of the work in the field is based on early theoretical works. However, much of the research presented in this thesis is experimental. The first experimental results presented are the two-photon absorption results of novel DCDHF chromophores and metal nanoclusters. That two-photon absorption work is the foundation of the work that makes up the bulk of the focus of this thesis which is entangled two-photon absorption. The previous ETPA set-up in the lab was reconfigured to ensure easier realignment between characterization and absorption experiments. A detailed study of molecules with differing entangled absorption properties is presented. After this was done background levels were re-measured, as well. The differing absorption properties of the molecules studied led to the hypothesis that virtual states may play more than just a key role in the absorption of entangled photons virtual states may in fact be necessary for observable ETPA. This is the first hypothesis that nearly resonant virtual/intermediate states may play such an important role in entangled two-photon absorption. This experimental work is followed up with theoretical work

comparing the entangled two-photon absorption properties of homonuclear and heteronuclear diatomic molecules to test this hypothesis.

Before diving into the literature review it is necessary to begin with a brief overview of correlation functions, two-photon absorption and entanglement. Correlation functions which lie at the heart of this research are briefly discussed. As stated earlier, it is imperative that the fields used for these studies are properly characterized and one such characterization method is correlation functions. One must understand correlation functions in order to understand these light matter interactions and how non-classical fields give rise to new and somewhat counterintuitive phenomena. Correlation functions also provide a point of reference in comparing classical and non-classical fields. A brief introduction to two-photon absorption will follow the overview of correlation functions. A brief introduction to quantum entanglement will also be discussed in Section 1.4 before. Those three sections should provide sufficient information to follow the review of the work that has been completed studying non-classical light matter interactions.

1.2 Correlation Functions

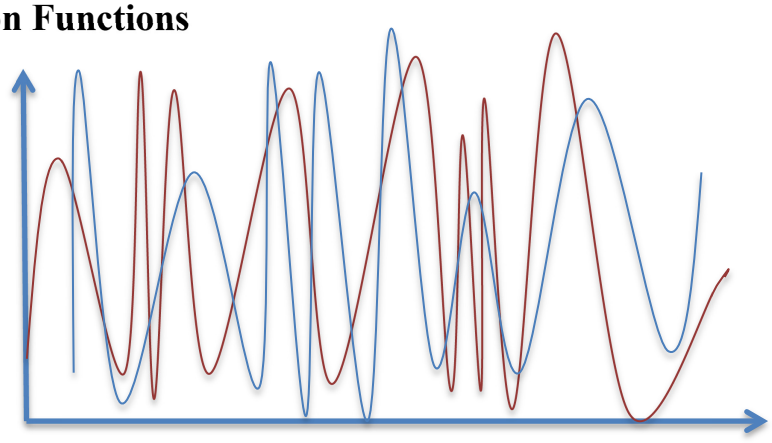

Figure 1.1 A correlation function measures the statistical correlation between random variables at different points in either space or time.

Correlation functions convey the statistical correlation of random variables at two points in space or time, and were first proposed by Roy Glauber. They are measures of fluctuations of equilibrium systems. Correlation functions are used in numerous fields to measure different types of dependencies such as spatial and temporal.

Classical intensity measurements are given by 2nd order fields. However, the entangled field must be written as a 4th order correlation function [4, 20]. The intensity correlation is measured by detecting two photons, one each at time t and t'. Quantized fields present more constraints on the quantum correlation. Using a quantum description of light, the operators do not commute and the ordering of the operators is important, which is a direct consequence of commutation relations that govern quantum mechanics. An uncertainty relation arises whenever two operators do not commute. We can measure these uncertainties for fields. This measure of the amplitude fluctuations is important because it is a measure of the correlations between the amplitudes and the intensities.

1.3 Two-Photon Absorption

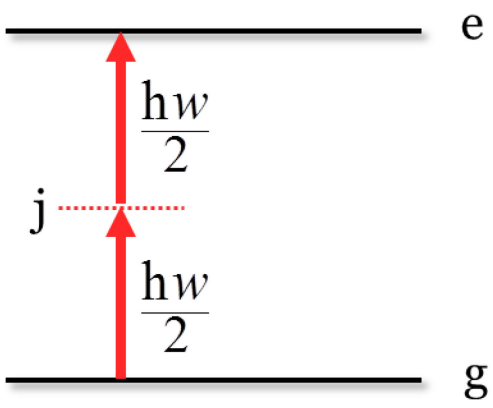

Figure 1.2. *Two-photon absorption between the ground and excited state of a two level system.*

Two-photon absorption was first theorized by Maria-Goeppert-Mayer in 1931. In her groundbreaking work she hypothesized that an atom in the ground state can be acted upon by two light quantum hν and hν', the sum of which (within the linewidth) equals the excitation threshold of the atoms $\nu + \nu' = \nu_{nm}$, and through it becomes promoted to an excited state energy $h\nu_{nm}$. Two-photon absorption occurs via some intermediate state between the ground and final excited state. However, she stated that the quadratic dependence was unfavorable because high intensities are needed for the effect to be observable. A derivation of the two-photon absorption cross-section following the method of Goeppert-Meyer, is presented in Chapter Two.

Two-photon absorption (TPA) is a non-linear optical phenomenon and is related to the third order polarizability and $\chi^{(3)}$. It differs from one-photon absorption (OPA), in that the two-photon absorption cross-section is proportional to the laser intensity squared, whereas the one-photon cross-section is linearly dependent on intensity. The two-photon absorption rate has a quadratic dependence on the input flux, $R_{TPA} \sim \varphi^2$.

Since TPA is related to the third order polarizability, the selection rules for OPA and TPA are different. Not only do selection rules differ for one photon and two-photon absorption events, but also the two-photon absorption selection rules differ for different types of molecules. In non-centrosymmetric molecules the ground to final state transition is electric dipole allowed and the transition is OPA and TPA allowed. If we write out the equation for the two-photon absorption cross-section in terms of the dipolar and two-photon terms, the dipolar term is non-zero for non-centrosymmetric molecules. In centrosymmetric molecules the one and two photon allowed transitions are mutually exclusive. Conservation of angular momentum leads to the angular momentum selection

rule terms (2, 0, -2). The parameters most important to the TPA cross-section are the ground and excited state transition dipole moments, change in dipole moment and the energy differences between states [18] and the field statistics [21].

1.3.1 Two-photon Absorption Correlations

In his work on two-photon absorption and field statistics, Mollow showed that the statistics of the exciting fields do in fact affect the two-photon transition rates [21]. Before comparing laser and chaotic light, he used second order correlation functions to derive two-photon probabilities for arbitrary fields. Without taking the dipole approximation we follow his treatment, where he begins with the Hamiltonian of the atom and the field given below:

$$H_I(t) = \frac{e}{mc} p(t) A(t) \qquad Equation\ 1.1$$

Where p(t) is the momentum operator and A(t) is the vector potential. The positive and negative frequency components of the field are given by the annihilation and creation operators:

$$A(t) = a(t) + a^{+}(t) \qquad Equation\ 1.2$$

The time evolution operator is given by:

$$U'(t) = 1 + \frac{1}{i\hbar}\int_0^t dt'^{H_I}(t') \qquad Equation\ 1.3$$

$$-\frac{1}{\hbar^2}\iint_0^t dt_1\, dt_2 \theta(t_1 - t_2) H_I(t_1) H_I(t_2)$$

The time evolution operator is then used to calculate the transition probability of an atom in its ground state.

$$P(t) \qquad \textit{Equation } 1.4$$

$$= \sum_{\varphi} \left| \left(\iint_0^t {}_F\langle \varphi | \langle f | U'(t) | 0 \rangle | \psi \rangle_F \mathfrak{L}(t_1', t_2') \right) \right|^2$$

Using second rank tensors

$$\mathcal{L}(t_1, t_2) \equiv \theta(t_1 - t_2) \left(\frac{e}{\hbar m c} \right)^2 \langle f | p(t_1) p(t_2) | 0 \rangle \qquad \textit{Equation } 1.5$$

$$= \theta(t_1 - t_2) \left(\frac{e}{\hbar m c} \right)^2 \sum_j p_{fj} p_{j0} e_1^{-i(\omega_j - \omega_f)t + i\omega_j t_2}$$

The probability can then be simplified and written as

$$P_2(t) = \sum_{\varphi} \left| \left(\iint_0^t dt_1 dt_2 \; {}_F\langle \varphi | a(t_1) a(t_2) | \psi \rangle_F \mathfrak{L}(t_1, t_2) \right) \right|^2 \qquad \textit{Equation } 1.6$$

$$= \iiiint_0^t dt_1' dt_2' dt_1 dt_2$$

$$\times \mathfrak{L}^*(t_1', t_2') \; {}_F\langle \psi | a^+(t_1') a^+(t_2') a(t_1) a(t_2) | \psi \rangle_F$$

$$\times \mathfrak{L}(t_1, t_2)$$

This can be generalized to:

$$P_2(t) = \int_0^t\int\int\int\int dt_1' dt_2' dt_1 dt_2 \times \mathfrak{L}^*(t_1', t_2') G^2(t_1', t_2'; t_1, t_2)\, \mathfrak{L}(t_1, t_2) \qquad Equation\ 1.7$$

Where $G^2(t_1', t_2'; t_1, t_2)$ is the second order correlation function:

$$G^2(t_1', t_2'; t_1, t_2) \equiv tr_F(\rho_F a^+(t_1') a^+(t_2') a(t_1) a(t_2)) \qquad Equation\ 1.8$$

Thus the probability of two-photon absorption for arbitrary fields in terms of the second order correlation function is given in Equation 1.7.

1.3.2 Design of Molecules with Large Two-Photon Absorption Cross Sections

These parameters can be tuned to design molecules with large Nonlinear optical properties. With the development of commercial applications for TPA (optical limiting, two-photon laser scanning microscopy, 3-D optical storage and two-photon induced biological caging), there has been a great demand for molecules with large TPA cross-sections. Much of Albota, Webb and Xu's work was devoted better understanding of TPA, in terms of designing highly efficient two-photon absorbers, characterizing two-photon absorption dyes for use as standards and pioneering two-photon excited fluorescence microscopy [22].

They reported design strategies for increasing symmetrical charge transfer in organic molecules. Quantum chemistry calculations utilizing multi-reference doubles configuration interactions (MRD-CI) were used to calculate energies and transition dipole

moments of the molecules. The imaginary part of the second hyperpolarizability was calculated using Sum Over States (SOS) method. They hypothesized that the experimental increase in the two-photon absorption cross-section was observed, as a result of an increase in the transition dipole moment (M_{12}) from 3.1 D to 7.2 D, an increase in the transition dipole moment (M_{01}) from 7.1 to 8.8 D and a decrease in the one-photon detuning term from 1.8 eV to 1.5 eV. This work was seminal in thinking about specific design characteristics such as increasing π-conjugation length and inducing large changes in quadruple moments for organic two-photon molecules.

1.4 Quantum Entanglement & Spectroscopy

Since the two-photon absorption rate is affected by the field statistics, it would be interesting to see how the rate is affected by the use of non-classical fields, in particular entangled photon pairs. An entangled state is a state such that the states are correlated and measuring a particle affects the outcome of the other particle with unit probability. Einstein explored the implausibility of entanglement in his paper entitled, "Can a quantum mechanical description of reality be considered complete?" famously referred to as the EPR paper. He hypothesized that quantum mechanics had to be causal and local [23]. Since, it did not appear to be so, there had to be hidden variables and such hidden variables although unknown to the observer did ensure the completeness of quantum mechanics as a theory. It was not until J.S. Bell developed a set of inequalities based on classical probabilities that it was proven that quantum mechanics does in fact violate causality and locality. Experimental data from quantum mechanics does not agree with the inequalities, disproving the idea of hidden variables. However, many experiments are still conducted to search for loopholes in Bell's inequalities [24-26]. The first

experimental proof of Bell's inequalities was conducted by CHSH, which measured the polarization correlations between pairs of optical photons [14]. However, it was Alain Aspect that developed the experimental set-up that in a sense definitively proved Bell's inequalities. Unlike CHSH, he used time varying analyzers that rotated after the particles were set into motion [12]. Now such tests are used to determine quality of the entangled states [27-29].

Entanglement has been utilized in many areas of quantum optics. However, several researchers have proposed utilizing the correlations in entangled fields to enhance spectroscopic measurements. There are several theorized effects that are hypothesized when using non-classical fields for multi-photon absorption. One such effect is a linear absorption rate at low input fluxes [30, 31]. Despite being a nonlinear process, the TPA rate with non-classical fields should have linear and not quadratic intensity dependence. This linear dependence arises from the unique nature of quantum fields.

Entangled two-photon absorption is derived from second order perturbation theory. The entangled two-photon rate is composed of a linear and quadratic component [20].

$$R_e = \sigma_e \phi + \delta_r \phi^2 \qquad Equation\ 1.9$$

Where σ_e and δ_r are

$$\sigma_e = \frac{\pi}{4A_eT_e}\omega_1^0\omega_2^0\delta\left(\varepsilon_f - \varepsilon_i - \omega_1^0 - \omega_2^0\right) \qquad Equation\ 1.10$$

$$\times \left| \sum_j D_{21}^{(j)} \frac{1 - \exp[-iT_e\Delta_1^{(j)} - T_e\kappa_j/2}{\Delta_1^{(j)} - i\kappa_j/2} \right.$$

$$\left. + D_{12}^{(j)} \frac{1 - \exp[-iT_e\Delta_2^{(j)} - T_e\kappa_j/2}{\Delta_2^{(j)} - i\kappa_j/2} \right|^2$$

and

$$\delta_r = \frac{\pi}{2}\omega_1^0\omega_2^0\delta\left(\varepsilon_f - \varepsilon_i - \omega_1^0 - \omega_2^0\right) \qquad Equation\ 1.11$$

$$\times \left| \sum_j \frac{D_{21}^{(j)}}{\Delta_1^{(j)} - i\kappa_j/2} + \frac{D_{12}^{(j)}}{\Delta_2^{(j)} - i\kappa_j/2} \right|^2$$

The entangled two-photon absorption cross-section is derived using second order perturbation theory [20]. The entangled two-photon wave-function can be given as the twin state below:

$$|twin\rangle \qquad Equation\ 1.12$$

$$= Nl \int\int d\omega_1 d\omega_2 exp\left[-\frac{(\omega_1 + \omega_2 - \omega_p)}{\Delta\omega_p^2}\right] sinc\left[\frac{l}{2\pi}(k_1 + k_2 - k_p)\right] |\omega_1\omega_2\rangle$$

The initial state of the entire system includes the interaction between the twin photon state and the atomic or molecular system in some initial state $|\psi_i\rangle$.

$$|\Psi_i\rangle = |\psi_i\rangle \otimes |twin\rangle \qquad Equation\ 1.13$$

Similarly, the final state can be written in terms of the final state of the atomic or molecular system in some initial state $|\psi_f\rangle$ and in this case the vacuum state since the twin photons are absorbed $|0,0\rangle$.

$$|\Psi_f\rangle = |\psi_f\rangle \otimes |0,0\rangle \qquad Equation\ 1.14$$

Now that the initial and final states are defined, the absorption rate can be calculated in an analogous manner to classical two-photon absorption [32, 33]. Using the interaction picture, the Hamiltonian can be written as

$$H = H_0 + H_I \qquad Equation\ 1.15$$

Where the interaction Hamiltonian is $H_I = -e\boldsymbol{\mathcal{E}}(\boldsymbol{r},t)\cdot\boldsymbol{r}$. We assume that a time evolution operator exists such that $|\Psi(t)\rangle = U_I(t)|\Psi_i\rangle$ [32]. If this is the case, then the probability amplitude that the system is in the final state $|\Psi_f\rangle = |\psi_f\rangle \otimes |0,0\rangle$ is the projection of $|\Psi(t)\rangle$ onto $|\Psi_f\rangle$. This probability amplitude is

$$\frac{\pi N l}{2A_q}\sqrt{\omega_1^0\omega_2^0}\,exp\left[-\frac{(\varepsilon_f-\varepsilon_i-\omega_p)^2}{\Delta\omega_p^2}\right] \qquad Equation\ 1.16$$

$$\times\left\{\sum_j D_{21}^{(j)}\frac{1-exp\left\{-i[T_e(\varepsilon_j-\varepsilon_i-\omega_1^0)+\left(T_0-\frac{T_e}{2}\right)(\varepsilon_f-\varepsilon_i-\omega_1^0-\omega_2^0)-T_e\kappa_j/2\right\}}{T_e(\varepsilon_j-\varepsilon_i-\omega_1^0)+\left(T_0-\frac{T_e}{2}\right)(\varepsilon_f-\varepsilon_i-\omega_1^0-\omega_2^0)-iT_e\kappa_j/2}\right.$$

$$\left.\times\sum_j D_{12}^{(j)}\frac{1-exp\left\{-i[T_e(\varepsilon_j-\varepsilon_i-\omega_1^0)+\left(T_0-\frac{T_e}{2}\right)(\varepsilon_f-\varepsilon_i-\omega_1^0-\omega_2^0)-T_e\kappa_j/2\right\}}{T_e(\varepsilon_j-\varepsilon_i-\omega_1^0)+\left(T_0-\frac{T_e}{2}\right)(\varepsilon_f-\varepsilon_i-\omega_1^0-\omega_2^0)-iT_e\kappa_j/2}\right\}$$

Where the transition matrix elements are $D_{kl}^{(j)} = \langle\psi_f|d_k|\psi_j\rangle\langle\psi_j|d_l|\psi_i\rangle$ and $T_0 = \frac{T_1+T_2}{2}$. The cross-section can then be defined in terms of Equation 1.19.

$$\sigma_e = \left|S_{fi}\right|^2 A_q^2/2 \qquad Equation\ 1.17$$

In order to simplify this expression, a few assumptions are made. The pump is assumed to be monochromatic $\Delta\omega_p \to 0$ and the phase-matching conditions are $\omega_p = \omega_1^0 + \omega_2^0$. The energy mis-match is written as $\Delta_k^j = \varepsilon_j - \varepsilon_i - \omega_k^0$.

Equation 1.17 can be simplified and rewritten as

$$\sigma_e = \frac{\pi}{4A_eT_e}\omega_1^0\omega_2^0\delta\left(\varepsilon_f - \varepsilon_i - \omega_1^0 - \omega_2^0\right) \times \left|\sum_j D_{21}^{(j)} \frac{1-\exp[-iT_e\Delta_1^{(j)} - T_e\kappa_j/2}{\Delta_1^{(j)} - i\kappa_j/2} + D_{12}^{(j)} \frac{1-\exp[-iT_e\Delta_2^{(j)} - T_e\kappa_j/2}{\Delta_2^{(j)} - i\kappa_j/2}\right|^2 \qquad Equation\ 1.18$$

1.4.1 Linear Intensity Dependence & Non-classical Fields

Javanainen and Gould discussed the linear intensity dependence of low intensity parametrically down converted light for potential uses in entangled two-photon absorption. Other types of fields that could be used are anti-bunched light, sub-poissonian light and squeezed light [30]. Spatiotemporal correlations lead to correlations in the detection of the twin photons created by spontaneous parametric down conversion. The model suggested by Javanainen et al estimates the two-photon transition rate a in three level atom excited with down-converted light with frequencies nearly resonant to the two-photon transition. There are two types of absorption rates described in this paper: the two-step process and the two-photon process. In the former process the field promotes the population to an intermediate state, and then in a second step the field promotes the population from that intermediate state to an excited state. On the other hand, the two-photon process occurs via a coherent superposition of the ground and excited state. These ideas are analogous to classical ideas of TPA for dipolar and virtual

state absorption mechanisms where the virtual state absorption occurs via a two-step process and dipolar absorption through the coherent superposition of the ground and excited state.

The entangled two-photon absorption rate is given by Equation 1.16. The d_{ij} terms are the matrix elements, h is Plank's constant, E^4 gives the classical two-photon quadratic term, gamma is the collision rate, gamma is the linewidth, delta is the detuning, E^2 is the non-classical intensity term.

$$R = \left|\frac{d_{01}d_{12}}{\hbar^2}\right|^2 \left(\frac{E^4\tau^2}{\Gamma} + \frac{\gamma/2}{\delta^2 + (\gamma/2)^2}\frac{E^2\hbar\omega\tau}{\epsilon_0 cA}\right) \qquad Equation\ 1.19$$

Independently, Gea-Banacloche et al also developed work on the linear intensity dependence at low input fluxes [31]. Using Mollow's derivation of the two-photon absorption rate:

$$w_2 = 2|g|^2 \int_{-\infty}^{\infty} dt\, e^{2i\omega_0 t - \Gamma|t|}\, G^{(2)}(-t, -t; t, t) \qquad Equation\ 1.20$$

Γ is the linewidth of the excited atomic level, ω_0 is the two-photon transition frequency, g is a coupling constant, and $G^{(2)}$ is the second order correlation function [31]. One should note that the ordering of the time-arguments is different than the general intensity correlation function [34]. For short-term lived atoms the rate becomes:

$$w_2 = 2|g|^2 G^{(2)}(0) \frac{\Gamma/2}{\left(\frac{\Gamma}{2}\right)^2 + (2\omega - \omega_0)^2} \qquad Equation\ 1.21$$

The correlation function of the field can also be rewritten in terms of its coherent (I_c) and squeezed-vacuum (I_{sv}) components:

$$G^{(2)}(0) = I_c^2 + I_c\left[4I_{sv} \pm (4I_{sv}^2 + 2\gamma I_{sv})^{\frac{1}{2}}\right] + 3I_{sv}^2 + \frac{1}{2}\gamma I_{sv} \qquad Equation\ 1.22$$

When I_c=0, the rate is linear at low input fluxes for purely squeezed fields [31].

1.4.1.1 Critical Flux

It is interesting to note that the linear intensity dependence is only valid for small input fluxes. As the flux increases, the nonclassical rate transitions to the classical quadratic rate. The flux at which this transition occurs is the critical flux. The critical flux can also be defined by the entangled two-photon absorption cross-section and the random two-photon absorption cross-section [20]:

$$\phi_c = \frac{\sigma_e}{\delta_r} \qquad Equation\ 1.23$$

Referring to Equation 1.19, this crossover intensity is given [30] as:

$$I_c = \frac{\hbar\omega}{\tau A} \qquad Equation\ 1.24$$

This is not the same I_c as given in Equation 1.22. This crossover intensity can be used to calculate the critical rate under the assumptions that the two-photon absorption event is completely on resonance and Γ=γ. This critical rate is given by:

$$R_c = \frac{1}{\gamma}\left(\frac{4\pi d_{01} d_{12}}{\hbar\lambda\epsilon_0 A}\right)^2 \qquad Equation\ 1.25$$

Schlawin et al also discussed this critical rate and also studied the critical rate's dependence on intermediate states [35]. This theoretical work explores two-photon

spectroscopy. The fields are generated by spontaneous parametric down conversion and a Hong-Ou-Mandel (HOM) interferometer balance beamsplitter mixes the fields. Using correlation functions and field statistics to derive the two-photon counting signal, gives a linear intensity dependence for weak fields while the second term in the equation displays a quadratic dependence on the field which dominates at higher intensities. Physically, the linear signal represents the signal and idler being indistinguishable such that both photons are reflected or transmitted. The quadratic term represent complete distinguishability such that each photon takes a different path [35].

Not only did Schlawin discuss the physical significance of the linear and quadratic terms, but this work also focuses on how transition from a linear to quadratic dependence depends on the intermediate state. When plotting the crossover intensity as a function, a signature HOM dip arises when the intermediate state is resonant with the signal and idler beams. Experimentally, this value is calculated after fitting the data to the function $Ax+Bx^2$. Once the linear and quadratic contributions are found they are plotted and the intercept is noted. For an APD dead time of 50ns this critical flux is ~1.4 x 10^7 cps. This does vary based on the choice of APD time with lower deadtimes producing lower crossover points.

1.4.2 Non-classical fields & Correlation Functions

To derive the entangled TPA rate, given earlier we use the treatment for field statistics given in *Frontiers of Nonequilibrium Statistical Physics* [34]. A state with a symmetrical minimum uncertainty is a coherent state. Unsymmetrical uncertainties give rise to squeezed states. This fourth order correlation function can be rewritten as $I^2 + I$. The classical intensity correlation function is written below as:

$$\boldsymbol{G_I^{(2)}(t'-t)} = \langle \boldsymbol{I(t')I(t)} \rangle \qquad \textit{Equation } 1.26$$
$$= \langle \boldsymbol{\varepsilon^*(t')\varepsilon(t')\varepsilon^*(t)\varepsilon(t)} \rangle$$

The fields can be arranged such that they are ordered as intensity terms. However, the fields cannot be arranged this way within the quantum description. This constraint arises due to the fact that operators do not commute. The ordering of the fields is determined by the experiment. The field can be written in terms of its positive and negative frequency parts. In the quantum description ε and ε^* are given by the raising and lowering operators.

$$E(r,t\,) = E^-(r,t) + E^+(r,t)$$

$$= \frac{1}{2}\left[\varepsilon(r,t\,)e^{-i\omega t} + \varepsilon^*(r,t)e^{i\omega t}\right]$$

$$G_I^{(2)}(\mathrm{t}_2 - t_1) = 4\langle I(t_1)I(t_2)\rangle \qquad \textit{Equation } 1.27$$
$$= \langle \varepsilon^*(t_1)\varepsilon(t_1)\varepsilon^*(t_2)\varepsilon(t_2)\rangle$$

The correlation function for a two-photon absorber can be written as

$$G_I^{(2)}(\mathrm{t}_2 - t_1) = 4\langle I(t_1)I(t_2)\rangle = \qquad \textit{Equation } 1.28$$

$$\langle \varepsilon^*(t_1)\varepsilon^*(t_1)\varepsilon(t_2)\varepsilon(t_2)\rangle,$$

which represents the simultaneous absorption of two photons.

The quantum treatment is much different. This intensity correlation function represents the detection of two-photons, one each at times t and t'. The quantum treatment involves the idea that measuring the field perturbs the system. The process is represented by the destruction of the two photons which is given by the matrix element $\langle \mathrm{f}|\hat{\mathrm{a}}(\mathrm{t}')\hat{\mathrm{a}}(\mathrm{t})|\mathrm{i}\rangle$. The quantized intensity correlation is given below:

$$\boldsymbol{G_I^{(2)}(t'-t)} \propto \qquad \textit{Equation } 1.29$$

$$\sum_{\boldsymbol{f}}\langle \boldsymbol{i}|\hat{\boldsymbol{a}}^{+}(\boldsymbol{t})\hat{\boldsymbol{a}}^{+}(\boldsymbol{t}')|\boldsymbol{f}\rangle\,\langle \boldsymbol{f}|\hat{\boldsymbol{a}}(\boldsymbol{t}')\hat{\boldsymbol{a}}(\boldsymbol{t})|\boldsymbol{i}\rangle,$$

Where we make use of the completeness theorem and rewrite Equation 1.29 as:

$$\boldsymbol{G}_{\boldsymbol{I}}^{(\boldsymbol{2})}(\boldsymbol{t}'-\boldsymbol{t}) = \langle \boldsymbol{i}|\hat{\boldsymbol{a}}^{+}(\boldsymbol{t})\hat{\boldsymbol{a}}^{+}(\boldsymbol{t}')\hat{\boldsymbol{a}}(\boldsymbol{t}')\hat{\boldsymbol{a}}(\boldsymbol{t})|\boldsymbol{i}\rangle \qquad Equation\ 1.30$$

The quantized two-photon correlation function can be written in the same manner, if the time ordering of the operators is handled correctly.

$$G_{TP}^{(2)}(t'-t) = \langle i|\hat{a}^{+}(t')\hat{a}^{+}(t')\hat{a}(t)\hat{a}(t)|i\rangle \qquad Equation\ 1.31$$

Again, it is important to note the difference between the intensity correlation function in Equation 1.30 and the two-photon correlation given in Equation 1.31.

In order to evaluate this and further illustrate where the linear intensity dependence arises, we utilize number states. For an initial number state, where (t=t'), the intensity correlation can be rewritten. Using the properties of number states, a proof is given below [34]:

$$\hat{\boldsymbol{a}}|\boldsymbol{n}\rangle = \sqrt{\boldsymbol{n}}|\boldsymbol{n}-\boldsymbol{1}\rangle \qquad Equation\ 1.32$$

$$\hat{a}^{+}|\mathrm{n}\rangle = \sqrt{\mathrm{n}+1}|\mathrm{n}+1\rangle$$

We assume that the initial states are pure number states and re-write the correlation function in terms of these number states.

$$\langle n|\hat{a}^{+}\hat{a}^{+}\hat{a}\hat{a}|n\rangle \qquad \text{Equation 1.33}$$

Evaluating the matrix element:

$$\langle n|\hat{a}^{+}\hat{a}^{+}\hat{a}\hat{a}|n\rangle = \sqrt{\mathrm{n}-1}\sqrt{\mathrm{n}-1}\sqrt{\mathrm{n}}\sqrt{\mathrm{n}} \qquad Equation\ 1.34$$

$$= n^2 - n \qquad Equation\ 1.35$$

As noted earlier, measuring the field perturbs the system. Detectors used for measurement absorb photons, thus we take the expectation value of the quantized two-photon correlation function. Using the properties of the raising and lowering operators we get an n^2 and n contribution which relates to the linear and quadratic contribution. Taking the limits of this expression, we see that the expectation value of the average number of photons increases, the quantized effect becomes less pronounced, and as it goes to infinity the correlation becomes classical in nature. It is also important to note that the quantized effect is pronounced at low intensities.

1.4.3 Necessary Rates for Experimental Realization of ETPA

Using commonly known experiment parameters, a range in which such a non-classical event could experimentally be observed was given. Entangled photons generated by spontaneous parametric down-conversion with collinear phase-matching were used. The light was focused to a Gaussian beam-waist. The transitions per unit time within the focal were calculated to be $48\pi\alpha c a_0 n$. The excitation rate of the sample is independent of the focal volume. This means that it is independent of the area and thus focusing.

Javanainen and Gould provide a starting place for determining the experimental observability of entangled-two photon interactions in molecules. The first requirement is a two-photon transition with a nearly resonant intermediate state detuning of less than 50 cm [30]. Secondly, since we are interested in non-classical effects we must look at intensities below the critical intensity. With this information we will follow Javanainen and Gould's method for calculating an experimental ETPA rate. For this calculation, we

start with the total transition rate, which is the sum of the two-step and two-photon contributions.

Assuming γ and Γ are equal and that the detuning is zero, the linear intensity rate becomes:

$$R_c = \frac{1}{\gamma}\left(\frac{4\pi d_{01} d_{12}}{\hbar \lambda \epsilon_0 A}\right)^2 \qquad Equation\ 1.36$$

The focal volume of the interaction can be calculated by assuming a Gaussian beam profile with a beam waist ω_0 and a coherence area ($A = \pi\omega_0^2$)

$$V = A\left(\frac{\pi {\omega_0}^2}{\lambda}\right) = 2\frac{A^2}{\lambda} \qquad Equation\ 1.37$$

Javanainen and Gould assume a gas of n atoms that are all two-photon resonant. The matrix elements are assumed to be ea_0. The decay rates are given as:

$$\gamma = \Gamma = \frac{d^2}{3\pi\epsilon_0\hbar}\left(\frac{2\pi}{\lambda}\right)^3 \qquad Equation\ 1.38$$

Combining Equation 1.36, Equation 1.37, and Equation 1.38, the total number of transitions per unit time within the focal volume in the linear regime can be written as:

$$R_c nV = 48\pi\alpha c {a_0}^2 n = 48\pi\frac{E_H}{\hbar}(a_0^3 n) \qquad Equation\ 1.39$$

where α denotes the fine-structure constant and E_H is the Hartree energy. Javanainen and Gould suggest a density of $n = 10^{12}$ cm^{-3} atoms, which would give a transition rate of 10^6 transitions/sec. When using light with a wavelength of 1 μm and a correlation time of

100 fs, experiments require approximately 2 x 10^{-6} μW in order to observe the rate calculated above.

1.4.4 Non-Classical Absorption in Atomic Cesium

Georgiades et al carried out the first experimental realization of linear intensity dependence in the atomic radiative process of two-photon atomic excitation. This departure from classical quadratic intensity dependence, was executed using squeezed light from non-degenerate parametric down-conversion to excite the two-photon transition in atomic cesium $6S_{1/2} \rightarrow 6P_{3/2} \rightarrow 6D_{5/2}$ [36]. A slope of 1.3 was recorded for the log-log plot.

The squeezed photons from an optical parametric oscillator were focused to 10μm in the magnetic optical trap (MOT) containing the cesium atoms. The trap's diameter was 200μm. Experimental runs with squeezed vacuum fields were compared with runs completed with coherent fields. The data from the former runs was fit with a linear plus quadratic function, whereas the data from the latter runs was fit with a purely quadratic function. The data points of five runs were used to calculate an average reduced χ^2, and calculate the significance levels of the trial functions. When fit with the quadratic plus linear function the squeezed light data had a significance level of C_{Q+L}=0.04, however, when the same data was fit with the purely quadratic function this resulted in a decrease in the significance level to $C_Q=5*10^{-10}$. The experiment provided evidence that new physics can be experimentally achieved and observed in spectroscopy with the use of non-classical fields.

1.4.5 Non-classical Effects in PPkTP

Dayan et al also utilized the non-classical nature of entangled photons to observe non-classical effects [37]. Using sum frequency generation (SFG) to generate entangled photons which exhibited a linear intensity dependence, they were able to obtain a rather large flux of 10^{12} entangled photon pairs/s which is approximately 0.3 μW of classical power [37]. Like the work of Georgiades the SFG rate also had a linear dependence. A single frequency Nd:YAG laser was used to pump a 12 mm PPkTP crystal. Entangled photons were generated and these photons had a broad bandwidth of 31 nm centered at 1064 nm. Prisms were used to filter out the pump. The dependence using log-log measurments showed a slope of 1.01 at lowest powers and 1.14 at highest powers[37].

1.4.6 Entangled Induced Transparency

Entangled two-photon induced transparency is another consequence of using entangled photons to carry out two-photon absorption. This experimental affect is analogous to electromagnetically induced transparency. Unlike the classical two-photon absorption cross-section which is constant, the ETPA cross-section is a non-monotonic function of the entanglement time. At certain entanglement times the entangled two-photon absorption cross-section drops three orders of magnitude. Therefore, entanglement induced transparency is based on the idea that at certain entanglement times the entangled two-photon signal becomes transparent. Inserting a quarter waveplates or any other field retarding devices into the beam path can experimentally vary the ETPA cross-sectional maxima, which vary as a function of the entanglement time. This dependence on entanglement can also in principle be utilized to induce other interesting

effects that cannot be realized with the use of classical fields, the ability to probe virtual excited states.

Both Saleh et al and Kojima et al theoretically calculated the virtual state energies of molecular hydrogen and OH, respectively [4, 5]. Both were able to use the time dependence that gave rise to the entanglement induced transparency to carry out the fourier transforms to calculate the intermediate/virtual state energies, since those states were summed over to calculate the ETPA cross-section. Virtual states are not eigenstates of the system, however, information regarding them could provide experimentalists more tools to use for characterizing and developing new materials. Such methods of experimentation are useful in characterizing and learning more about materials.

1.4.7 Entangled Two-Photon Absorption in Organic Molecules

While both Kimble and Dayan's work experimentally showed that non-classical fields when interacting with matter could experimentally demonstrate departures from classical theory, not much work has been done to realize these phenomena in larger molecular systems [1-3, 38]. To expand upon work done by Kimble and Dayan our group sought to observe entangled photon absorption in organic molecules, hoping that the use of organic molecules would make measurements easier to observe with the use of molecules with large two-photon absorption cross-sections and easier to conduct by studying molecules in solution phase.

Lee et al was the first to measure entangled two-photon absorption in an organic molecule [1]. This was demonstrated in an organic porphyrin. He also experimentally demonstrated the non-monotonic behavior [1]. Harpham et al demonstrated entangled two-photon absorption was the use of ten orders of magnitude less photons in

experiments conducted in both thin film and solutions [2]. He explored σ_e and δ_r as functions of thiophene dendrimer generation. These thiophenes were chosen because of their high classical two-photon absorption cross-section which varies from 6-1130 GM [39]. Guzman et al has also shown that it is possible to control the ETPA process by controlling the spatial orientation of the entangled photons [3]. This can be done by changing the phase matching conditions which controls the spatial orientations of the signal and idler photons. When varying the three phase matching conditions (non-collinear, collinear and spatially separated) it was shown that the non-collinear condition exhibited the largest response, followed by the collinear condition with the spatially separated field showing no response [3].

1.4.7.1 The Role of Decoherence in Open systems

Quantum entanglement is environment sensitive, and depending on the system or method of generation entangled photons can suffer from decoherence. As such, the very first experiments in this field were conducted in extremely clean environments. While observing these nonclassical effects in crystals or atoms located in a vacuum or magnetic optical trap are interesting and are certainly the first step in understanding these light matter interactions, they do not provide realistic conditions for expanding this work to more interesting systems and to application.

In contrast to these clean environments are the "messier" much more realistic systems. 'Open' systems provide much more realistic systems of interest; however, once environmental effects of 'open' systems are included the physics of treating the system become much more difficult to handle. In discussions of quantum dynamic theory it is necessary to clearly define what is meant by: system. It is important to note the

complexity of the system proposed in this study. Not only does this study focus on nonclassical fields, but materials that we hope to probe with these fields. Here we must deal with molecules interacting with solution, as well as, entangled photons interacting with the environment, and the interactions between the entangled photons and molecules/solution, as well.

Because of this, we can think of the system as three components. The fields are entangled. There is the issue of whether the material itself has entanglement, and whether coupling creates entanglement between the field and the material. At this point the main goal is to only focus on the entanglement in the field. While it may be interesting to study whether entangled photons can entangle the states of a molecule, at this point we are only interested in whether the use of entangled photons can produce nonclassical effects and whether we can use this information to tailor the design of new molecules. This topic of material entanglement and coupling has been explored quite extensively in quantum biology [40, 41]. The entangled fields do interact with the environment, which creates loss of entanglement. This is a particularly relevant issue for pulsed spontaneous parametric down conversion and interference experiments which as conducted with these fields [42] Relevant time scales to keep in when dealing with and conducting experiments on "open" systems are [43]:

- Natural frequency of the system
- Relaxation time scale
- Memory time

It's important to look at each particular piece of the system separately because each has complexities worth noting. For example, the dynamics of a molecule in solution

are not trivial. If system bath coupling is included things become quite complicated. The Hamiltonian of a generic system in solution would be [44]:

$$\widehat{H} = H_S + H_B + H_{BS} \qquad Equation\ 1.40$$

This modified Hamiltonian when utilized with the optical response function leads to dephasing terms. In much of the theoretical work on entangled two photon absorption, these terms are ignored [4, 20]. For example, in relaxation effects that arise from coupling to the phonon are not included [45]. However, they are included in calculations in Chap.3. These terms lead to Lorentzian line broadening. A similar treatment was used in Schlawin et al, where the states were broadened by 200 cm^{-1} [35].

In most cases studying open quantum systems, the density matrix notation is used. However, a density operator formulation has only been extended to entangled two-photon absorption in some of the later more applied papers using ETPA. Optical response functions can be used to describe the dynamics of open quantum systems [44, 46]. In several papers these interactions are treated using the superoperator Louiville space [47].

1.5 Overview of Subsequent Chapters

This dissertation combines work in classical and non-classical two-photon absorption in order to study novel materials and novel interactions between these materials and non-classical light. Theoretical work was also conducted. The combination of classical, non-classical and theoretical work is used to make statements towards future rational design of ETPA enhanced molecules.

1.5.1 Chapter Two: Classical Two-Photon Absorption

I began by looking at new and novel materials developed for TPA. Just a few of the novel materials studied in this dissertation are DCDHF chromophores and silver nanoclusters. Studying the TPA cross-section of the DCDHF chromophores and silver nanoclusters is one method of characterizing the usefulness of these materials for potential applications. Researchers want to create new organic self-assembled materials for use in single-molecule imaging that are brighter and more photostable.

As a part of this study to find novel two-photon molecules, I also looked at several novel organic fluorophores that have applications in single molecule imaging. The DCDHF fluorophores are composed of various amine donors and dicyanodihydrofuran acceptors linked by a conjugated unit [48]. I completed several comparative studies: a dimerization study, extended conjugation study and finally a donor acceptor study to study charge transfer characteristics in these molecules. Because of their decent two-photon properties, many of these novel chromophores were also used to study entangled two-photon interactions. In working with such materials the goal is to demonstrate ETPF and use those measurements and theoretical calculations to work with collaborators to develop ETPF sensitive chromophores for possible usage in entangled two-photon microscopy, and ultimately begin developing such a system within our group.

As nano-scale science progresses, many have realized that metal nanoclusters possess many unique and unusual properties that become more apparent as the size of these gold particles decreases. Much research has been devoted to studying the size and electronic structure of gold nanoparticles. Size properties and electronic structure properties play a key role in determining the chemical reactivity of such structures [49].

This work has been used to determine the chemical reactivity and other properties of these gold clusters as a function of their size [50, 51].

However, many of the optical effects, excited state dynamics and non-linear optical properties have yet to be rigorously explored and researched. Additional research in this area is essential in determining the non-linear optical properties of these structures [2]. Therefore, the first goal of this research project was to understand the non-linear optical properties of these silver structures and fully grasp the scientific principles that govern these small clusters. Our group has worked extensively on gold nanoclusters, however, little has been done with silver nanoclusters.

I also studied silver nanoclusters stablilized by single stranded DNA. This single stranded DNA with silver nanoclusters is then hybridized with a guanine rich single stranded DNA to create a fluorescent species [52, 53]. These clusters have a much higher quantum yield and seem to be much more stable than the monolayer protected clusters. However, there are questions that surround the exact composition of the sample, how the silver clusters are arranged in the DNA and whether the mechanism of fluorescence comes from silver clusters. I showed that the number of fluorescent counts had quadratic power dependence, which suggests a two-photon absorption process.

Data from steady state and TPA measurements will be presented for both sets of samples is presented in Chapter 2. The work on the silver nanoclusers was dervived from previous work in the group on gold nanoclusters. This work highlights DNA template nanoclusters which differ from conventional monolayer protected clusters.

1.5.2 Chapter Three: Entangled Two-Photon Absorption

After studying classical interactions, it was important to begin to characterize non-classical interactions between varieties of two-photon absorbing materials. In Chapter 3, we demonstrate that entangled photons are sensitive to the absorption mechanism of the molecule being probed. We present work with our collaborators that presents a model that describes the mechanism of absorption of entangled photons for various material systems.

To further classify these interactions it was necessary to take a step back and consider less complex molecules. While, large conjugated molecules are necessary for the viability of such non-classical techniques. Their complex dynamics make it difficult to fully characterize and understand the dynamics of these interactions.

1.5.3 Chapter Four: Virtual State Absorption

Continuing along this path of research, in order to better comprehend the exact dynamics of ETPA, we study diatomic molecules interactions with entangled photons in Chapter 4. This theoretical work is a comparison of homonuclear and heteronuclear diatomic molecules. In order to carry out this research, it was necessary to utilize quantum chemistry techniques to calculate the excited state to excited state transition dipole moments of these molecules. This work includes an in depth look at the selection rules for TPA, the polarization and field dependence, the molecular symmetry are covered because all these issues play an important role in multiphoton absorption. With the addition of non-classical fields, we explore the interferences and how the non-classical correlations affect the selection rules and explore how polarization dependence

and molecular symmetry also play a role. Fields can also be used for material characterization, as well as, for harvesting energy solar energy.

1.5.4 Chapter 5: Computational Methods

With the advent of more powerful and faster computers and computing systems, as well as, more sophisticated algorithms accessible through commercially available quantum chemistry programs the field of computational quantum chemistry has expanded beyond merely quantum chemists. There are in principle three general steps for solving quantum chemistry problems. The first step is to make the Born Oppenheimer Approximation. The second step is to choose a method for expanding the multi-electron wavefunction, and the last step is choosing a basis set.

We utilize quantum chemistry techniques in Chapter 5, to explore entangled two-photon absorption in diatomic molecules. This requires the use of specialize programs such as Molpro. While most optimization and ground state/excited state energy calculations are straightforward to run for small molecules, work does become more involved when dealing with excited state to excited state calculations. There are two-methods for calculating these excited state to excited state transition dipole moments that we explore in this dissertation, the Multireference Configuration Interaction method and the Equation of Motion method. Multireference calculations use more than one reference determinant from which all determinants are included in order to take into account the electron correlation in the system. The equation of motion method utilizes Green's function methods to calculate the transition moments without directly solving Schrodinger's equation for the ground and excited states. This dissertation is concluded

in Chapter 6. Chapter 6 is a summary of the work we have completed. It also contains conclusions and a summary of future work to be carried out in the field.

References:

[1] D.-I. Lee and T. Goodson, "Entangled Photon Absorption in an Organic Porphyrin Dendrimer," *The Journal of Physical Chemistry B,* vol. 110, pp. 25582-25585, 2006/12/01 2006.

[2] M. R. Harpham, O. z. n. Süzer, C.-Q. Ma, P. Bäuerle, and T. Goodson, "Thiophene Dendrimers as Entangled Photon Sensor Materials," *Journal of the American Chemical Society,* vol. 131, pp. 973-979, 2009/01/28 2009.

[3] A. R. Guzman, M. R. Harpham, O. z. n. Süzer, M. M. Haley, and T. G. Goodson, "Spatial Control of Entangled Two-Photon Absorption with Organic Chromophores," *Journal of the American Chemical Society,* vol. 132, pp. 7840-7841, 2010/06/16 2010.

[4] B. E. A. Saleh, B. M. Jost, H.-B. Fei, and M. C. Teich, "Entangled-Photon Virtual-State Spectroscopy," *Physical Review Letters,* vol. 80, pp. 3483-3486, 1998.

[5] J. Kojima and Q.-V. Nguyen, "Entangled biphoton virtual-state spectroscopy of the A2Σ+–X2Π system of OH," *Chemical Physics Letters,* vol. 396, pp. 323-328, 2004.

[6] M. Planck, "Ueber das Gesetz der Energieverteilung im Normalspectrum," *Annalen der Physik,* vol. 309, pp. 553-563, 1901.

[7] A. D. Aczel, *Entanglement: the greatest mystery in physics*. New York: Four Walls Eight Windows, 2002.

[8] A. Einstein, M. Born, and H. Born, *The Born-Einstein letters; correspondence between Albert Einstein and Max and Hedwig Born from 1916 to 1955*. New York: Walker, 1971.

[9] A. E. a. B. P. a. N. Rosen, "Can quantum-mechanical description of physical reality be considered complete?," vol. 41, ed. Physical Review, 1935.

[10] J. S. Bell, "On the Einstein Podolsky Rosen Paradox," vol. 195, 1964.

[11] J. F. C. a. M. A. H. a. A. S. a. R. A. Holt, "Proposed experiment to test local hidden-variable theories," vol. 23, ed. Phys. Rev. Lett., 1969, p. 880.

[12] D. A. Aspect, G. Roger, "Experimental test of Bell's inequalities using time-varying analyzers," vol. 49, 1982.

[13] R. P. Feynman, "SIMULATING PHYSICS WITH COMPUTERS," *International Journal of Theoretical Physics,* vol. 21, pp. 467-488, 1982.

[14] J. F. C. Holt, M. A. Horne, A. Shimony, and R. A., "Proposed experiment to test local hidden-variable theories," vol. 23, ed. Phys. Rev. Lett., 1969, p. 880.

[15] D. N. M. S. Olmschenk, P. Maunz, D. Hayes, L.-M. Duan, and C. Monroe, "**Quantum Teleportation Between Distant Matter Qubits**," *Science,* vol. **323**, pp. 486-489, 2009.

[16] E. Collini, C. Y. Wong, K. E. Wilk, P. M. G. Curmi, P. Brumer, and G. D. Scholes, "Coherently wired light-harvesting in photosynthetic marine algae at ambient temperature," *Nature,* vol. 463, pp. 644-647, 2010.

[17] N. K. Langford, S. Ramelow, R. Prevedel, W. J. Munro, G. J. Milburn, and A. Zeilinger, "Efficient quantum computing using coherent photon conversion," *Nature,* vol. 478, pp. 360-363, 2011.

[18] A. Bhaskar, R. Guda, M. M. Haley, and Goodson, "Building Symmetric Two-Dimensional Two-Photon Materials," *Journal of the American Chemical Society,* vol. 128, pp. 13972-13973, 2006/11/01 2006.

[19] A. Bhaskar, G. Ramakrishna, Z. Lu, R. Twieg, J. M. Hales, D. J. Hagan*, et al.*, "Investigation of Two-Photon Absorption Properties in Branched Alkene and Alkyne Chromophores," *Journal of the American Chemical Society,* vol. 128, pp. 11840-11849, 2006/09/01 2006.

[20] H.-B. Fei, B. M. Jost, S. Popescu, B. E. A. Saleh, and M. C. Teich, "Entanglement-Induced Two-Photon Transparency," *Physical Review Letters,* vol. 78, pp. 1679-1682, 1997.

[21] B. R. Mollow, "Two-Photon Absorption and Field Correlation Functions," *Physical Review,* vol. 175, pp. 1555-1563, 1968.

[22] M. Albota, "Design of Organic Molecules with Large Two-Photon Absorption Cross-Sections," *Science,* vol. 281, pp. 1653-1656, 1998.

[23] A. E. Rosen, B. Podolsky, and N., "Can quantum-mechanical description of physical reality be considered complete?," vol. 41, ed. Physical Review, 1935.

[24] M. A. Rowe, D. Kielpinski, V. Meyer, C. A. Sackett, W. M. Itano, C. Monroe*, et al.*, "Experimental violation of a Bell's inequality with efficient detection," *Nature,* vol. 409, pp. 791-794, Feb 2001.

[25] W. Tittel, J. Brendel, H. Zbinden, and N. Gisin, "Violation of bell inequalities by photons more than 10 km apart," *Physical Review Letters,* vol. 81, pp. 3563-3566, Oct 1998.

[26] M. Ansmann, H. Wang, R. C. Bialczak, M. Hofheinz, E. Lucero, M. Neeley*, et al.*, "Violation of Bell's inequality in Josephson phase qubits," *Nature,* vol. 461, pp. 504-506, Sep 2009.

[27] P. G. Kwiat, A. J. Berglund, J. B. Altepeter, and A. G. White, "Experimental verification of decoherence-free subspaces," *Science,* vol. 290, pp. 498-501, Oct 2000.

[28] P. G. Kwiat, K. Mattle, H. Weinfurter, A. Zeilinger, A. V. Sergienko, and Y. Shih, "New High-Intensity Source of Polarization-Entangled Photon Pairs," *Physical Review Letters,* vol. 75, pp. 4337-4341, 12/11/ 1995.

[29] Y. Shih, "Entangled biphoton source-property and preparation," *Reports on Progress in Physics,* vol. 66, pp. 1009-1044, Jun 2003.

[30] J. Javanainen and P. L. Gould, "Linear intensity dependence of a two-photon transition rate," *Physical Review A,* vol. 41, pp. 5088-5091, 1990.

[31] J. Gea-Banacloche, "Two-photon absorption of nonclassical light," *Physical Review Letters,* vol. 62, pp. 1603-1606, 1989.

[32] H. B. Bebb and A. Gold, "Multiphoton Ionization of Hydrogen and Rare-Gas Atoms," *Physical Review,* vol. 143, pp. 1-24, 03/04/ 1966.

[33] P. Lambropoulos, "Theory of multiphoton ionization: Near-resonance effects in two-photon ionization," *Physical Review A,* vol. 9, pp. 1992-2013, 05/01/ 1974.

[34] G. T. Moore, M. O. Scully, and O. North Atlantic Treaty, *Frontiers of nonequilibrium statistical physics*. New York: Plenum Press, 1986.

[35] S. Frank and M. Shaul, "Photon statistics of intense entangled photon pulses," *Journal of Physics B: Atomic, Molecular and Optical Physics,* vol. 46, p. 175502, 2013.

[36] N. P. Georgiades, E. S. Polzik, K. Edamatsu, H. J. Kimble, and A. S. Parkins, "Nonclassical Excitation for Atoms in a Squeezed Vacuum," *Physical Review Letters,* vol. 75, pp. 3426-3429, 11/06/ 1995.

[37] B. Dayan, A. Pe'er, A. A. Friesem, and Y. Silberberg, "Nonlinear Interactions with an Ultrahigh Flux of Broadband Entangled Photons," *Physical Review Letters,* vol. 94, p. 043602, 02/02/ 2005.

[38] L. Upton, M. Harpham, O. Suzer, M. Richter, S. Mukamel, and T. Goodson, III, "Optically Excited Entangled States in Organic Molecules Illuminate the Dark," *Journal of Physical Chemistry Letters,* vol. 4, pp. 2046-2052, Jun 20 2013.

[39] G. Ramakrishna, A. Bhaskar, P. Bauerle, and T. Goodson, "Oligothiophene Dendrimers as New Building Blocks for Optical Applications†," *The Journal of Physical Chemistry A,* vol. 112, pp. 2018-2026, 2008/03/01 2007.

[40] E. C. a. G. D. Scholes, "Coherent Intrachain Energy Migration in a Conjugated Polymer at Room Temperature," *Science,* vol. 323, pp. 369-373 2009.

[41] E. Collini, C. Y. Wong, K. E. Wilk, P. M. G. Curmi, P. Brumer, and G. D. Scholes, "Coherently wired light-harvesting in photosynthetic marine algae at ambient temperature," *Nature,* vol. 463, pp. 644-647, 2010.

[42] M. Atatüre, A. V. Sergienko, B. E. A. Saleh, and M. C. Teich, "Dispersion-Independent High-Visibility Quantum Interference in Ultrafast Parametric Down-Conversion," *Physical Review Letters,* vol. 84, pp. 618-621, 01/24/ 2000.

[43] S. Banerjee, "Open Quantum Systems," Presentation.

[44] E. Geva, "Title," unpublished|.

[45] F. Schlawin, K. E. Dorfman, B. P. Fingerhut, and S. Mukamel, "Manipulation of two-photon-induced fluorescence spectra of chromophore aggregates with entangled photons: A simulation study," *Physical Review A,* vol. 86, Aug 2012.

[46] S. Mukamel, *Principles of nonlinear optical spectroscopy*. New York: Oxford University Press, 1995.

[47] F. Schlawin and S. Mukamel, "Matter correlations induced by coupling to quantum light," *Physical Review A,* vol. 89, Jan 23 2014.

[48] S. J. Lord, Z. Lu, H. Wang, K. A. Willets, P. J. Schuck, H.-l. D. Lee*, et al.*, "Photophysical Properties of Acene DCDHF Fluorophores: Long-Wavelength Single-Molecule Emitters Designed for Cellular Imaging," *The Journal of Physical Chemistry A,* vol. 111, pp. 8934-8941, 2007/09/01 2007.

[49] S. H. Yau, O. Varnavski, and T. Goodson, "An Ultrafast Look at Au Nanoclusters," *Accounts of Chemical Research,* vol. 46, pp. 1506-1516, 2013/07/16 2013.

[50] G. Ramakrishna, O. Varnavski, J. Kim, D. Lee, and T. Goodson, "Quantum-Sized Gold Clusters as Efficient Two-Photon Absorbers," *Journal of the American Chemical Society,* vol. 130, pp. 5032-5033, 2008.

[51] O. Varnavski, G. Ramakrishna, J. Kim, D. Lee, and T. Goodson, "Critical Size for the Observation of Quantum Confinement in Optically Excited Gold Clusters," vol. 132, ed: American Chemical Society, 2010.

[52] J. Sharma, H.-C. Yeh, H. Yoo, J. H. Werner, and J. S. Martinez, "A complementary palette of fluorescent silver nanoclusters," *Chemical Communications,* vol. 46, pp. 3280-3282, 2010.

[53] H.-C. Yeh, J. Sharma, J. J. Han, J. S. Martinez, and J. H. Werner, "A DNA–Silver Nanocluster Probe That Fluoresces upon Hybridization," vol. 10, ed: American Chemical Society, 2010.

Chapter 2

Two-Photon Absorption

Abstract: We examine at the two-photon absorption efficiencies of dicyanodihydrofuran (DCDHF) and hybridized silver DNA-templated nanoclusters. Little is known in terms of two-photon absorption efficiencies of either of these molecules. Steady state and two-photon absorption measurements are conducted on both samples. The two-photon excited fluorescence curves, along with the log-log plots are presented. This data is used to quantify the charge transfer process is the DCDHF fluorophores, as well as, help elucidate the process of the fluorescence enhancement in the silver nanoclusters. Based on this steady state and two-photon analysis, we determine whether these molecules are good candidates to pursue entangled two-photon absorption studies.

The bulk of the DNA hybridized silver nanocluster work in this chapter was originally published in the following document:

S. H. Yau, N. Abeyasinghe, M. Orr, L. Upton, O. Varnavski, J. H. Werner*, et al.*, "Bright two-photon emission and ultra-fast relaxation dynamics in a DNA-templated nanocluster investigated by ultra-fast spectroscopy," *Nanoscale,* vol. 4, pp. 4247-4254, 2012 2012.

Modifications to the original document were made solely for adapting the content to this form, and to focus solely on the steady-state and two-photon absorption work.

2.1 Overview of Chapter

The goal of this chapter is to give an overview of the underlying theory and theoretical and experimental background that informs much of the work on two-photon interactions in later chapters. This chapter covers the experimental techniques that were utilized to obtain the experimental results in Sections 2.6 and 2.6.

Included in this chapter are the derivations and explanations of common terms that often arise in the literature. The goal of the following sections is to provide the reader with a suitable and coherent foundation to analyze and connect the findings presented in this and later chapters. To begin this synopsis, we will cover steady state absorption and emission and follow that with the derivation of the two-photon absorption cross-section.

The cross-section will be derived two ways: first using the induced polarization in terms of the macroscopic susceptibility and the second method using the interaction representation of the Hamiltonian and using perturbation theory in a quantum mechanical treatment. While the two-photon absorption cross-section is directly related to the parameters/statistics of the fields and the material properties of the matter being probed, the experimental method of calculating the TPA cross-section does not account for field statistics, since the use of a standard allows one to cancel the field terms. This method will be outlined in Section 2.5.3. The goal is to explore and explain how the statistics of the fields and the atomic and molecular structures relate to measurable two-photon parameters.

We will also explore the intensity factors that play a very large part in these measurements and how they are related to each other and to the materials that will be studied. This also includes a look at the selection rules for TPA. An explanation of the TPA experimental set-up and an explanation of how the TPA cross-section is calculated experimentally are also given.

2.2 Classical Two-Photon Absorption Introduction

As applications utilizing two-photon absorption spectroscopy have increased, the need for molecules with large two-photon absorption cross-sections has increased, as well. There are several classes of molecules with two-photon properties that have been studied such as charge transfer chromophores, polymers, linear oligomers and metal nanoclusters [1-4]. While, much work early work focused on linear systems and increasing conjugation linearly, the Goodson group has extensively studied large 2D macromolecules and systems with 2D extended conjugation and even some 3D molecules [1, 2, 5, 6]. These investigations focus on new and novel ways to increase TPA absorption cross-sections to meet the increasing demand.

As single molecule imaging technology advances and the need for higher resolution imaging increases, the need for stable and bright fluorophores increases, as well. Multi-photon imaging of biological samples requires fluorophores that exhibit high TPA cross-sections, high fluorescence quantum yields, stability against photobleaching, fluorescence tunability, and biocompatibility. The most common fluorophores considered for multi-photon imaging are organic dyes, quantum dots and metal nanoclusters. This work presents a spectroscopic analysis of DCDHF fluorophores and DNA-templated silver nanoclusters.

These nanoclusters have unique properties that distinguish them from many other metal nanoclusters. These clusters, which are embedded on single strands of DNA, become highly fluorescent once a second complementary strand of DNA is introduced. The use of DNA makes these clusters particularly useful for biological imaging. Much work has been dedicated to understanding the absorption properties of metal nanoclusters. However, much less work has been dedicated to studying these novel DNA-embedded silver nanoclusters compared to monolayer-protected nanoclusters.

2.3 One-Photon Absorption

There are two ways to treat spectroscopic phenomena, either macroscopically or microscopically. In the macroscopic case, we can begin by looking at the polarization, which is the dipole moment per unit volume, and it depends on the strength of the electric field. A simple picture of absorption can be described using a harmonic oscillator representation based on a damped oscillation by an external field. The differential equation governing this oscillator and field interaction is [7]:

$$m\frac{d^2y}{dt^2} + m\gamma\frac{dy}{dt} + m\omega_0^2 y = qE_0\exp(i\omega t) \qquad Equation\ 2.1$$

Where the mass of the oscillator is m, the charge is q, and the characteristic frequency of the oscillator is ω_0 and γ is the damping constant [7]. The solution to the complex amplitude is

$$y = \frac{qE_0}{m({\omega_0}^2 - \omega^2 + i\gamma\omega)}\exp(i\omega t) \qquad Equation\ 2.2$$

The induced dipole moment in the y direction is given by

$$\mu_y = qy = \frac{q^2 E_0}{m({\omega_0}^2 - \omega^2 + i\gamma\omega)} \exp(i\omega t) \qquad Equation\ 2.3$$

Since there are N oscillators in a particular sample per unit volume, the induced polarization is obtained with the equation

$$P_{ind} = \chi_e \varepsilon_0 E = N\mu \qquad Equation\ 2.4$$

where the susceptibility is

$$\chi_e = \frac{q^2 N}{m({\omega_0}^2 - \omega^2 + i\gamma\omega)} \qquad Equation\ 2.5$$

Generally the imaginary component is negligible, but this is not the case when the field frequency is near the resonant frequency [8]. The imaginary component of the complex index of refraction is given by

$$n'' = \frac{Nq^2}{8\varepsilon_0 m\omega_0} \frac{\gamma}{(\omega_0 - \omega)^2 + (\gamma/2)^2} \qquad Equation\ 2.6$$

If one decides to solve the wave equation for a lossy material, one would begin with the wave equation and assume plane wave solutions. The Lorentz model does account for some loss, but absorption of light in a medium is usually defined as the fraction of the power dissipated per unit length of the medium [8]. To relate Beer-Lambert Law to the harmonic oscillator model of absorption, we begin with the wave equation:

$$\nabla^2 \tilde{E} = \tilde{\epsilon}\mu_0 \frac{\partial^2 \tilde{E}}{\partial t^2} \qquad Equation\ 2.7$$

As stated earlier, the solutions to this differential equation are in the form of plane wave solutions:

$$\tilde{E}(z,t) = \tilde{E}_0 e^{i(\tilde{k}z-\omega t)} \qquad Equation\ 2.8$$

where the wave number is complex

$$\tilde{k} = k + i\kappa \qquad Equation\ 2.9$$

$$\kappa \equiv \sqrt{\tilde{\epsilon}\mu_0\omega}$$

If you insert the complex wave number into Equation 2.8, the wave equation becomes

$$\tilde{E}(z,t) = \tilde{E}_0 e^{-\kappa z} e^{i(kz-\omega t)} \qquad Equation\ 2.10$$

where κ is the damping term and accounts for the attenuation of the beam by absorption. Since the intensity goes as E^2, which gives damping terms that go as $e^{-2\kappa z}$, where $\alpha=2\kappa$. Going back to the harmonic oscillator description

$$\alpha = \frac{Nq^2}{8\varepsilon_0 m\omega_0}\frac{\gamma}{(\omega_0-\omega)^2+(\gamma/2)^2} \qquad Equation\ 2.11$$

The Beer-Lambert Law governs the steady state absorption, where α is the same variable defined above in Equation 2.11.

$$dI = \alpha\, dz \times I(z) = N\sigma(\omega)I(z) \qquad Equation\ 2.12$$

where N is the number of particles and σ is the cross-section as a function of the frequency. The solution to this differential equation is given below:

$$I(z) = I(0)e^{-\alpha z} = I(0)e^{-N\sigma l}. \qquad Equation\ 2.13$$

$$Transmission = \frac{I}{I_0} = e^{-\alpha z} = e^{-N\sigma l} \qquad Equation\ 2.14$$

From this we can derive an equation for absorption after taking the log of both sides we have

$$A = log\frac{I_0}{I} \qquad Equation\ 2.15$$

where I_0 is the input intensity and I is the transmitted intensity. The absorption is the ratio between the input and output flux. This can approximated to:

$$A = N\sigma l = \varepsilon cl, \qquad Equation\ 2.16$$

where not only can the absorption be given by the one-photon cross-section, σ, and N, the number of units per unit volume, but we can also relate it to the molar extinction coefficient (ε), concentration (c) and l is the length of the cuvette or sample holder. Experimentally, both the absorption and fluorescence measurements were completed with the use of steady state instrumentation for samples that were prepared in solution phase.

Absorption is measured directly on the UV-vis. All measurements were completed on an Agilent Model 8341 with deuterium and tungsten lamps.

2.4 Emission

We can also measure emission from various samples. Emission measurements are carried out on a Fluoromax-2 fluorimeter with a xenon arc lamp and two monochrometers. Emission and excitation scans can be completed.

The efficiency of emission can be determined by the quantum yield. It gives the ratio of absorbed photons to emitted photons. However, this is a very meticulous experiment to carry out. An accurate measurement and calculation of the quantum yield is critical for conducting two-photon excited fluorescence measurements which are easier to conduct than absolute measurement of TPA. The absolute measurement is difficult to calculate due to the temporal and spatial dependence of the fields. However, this method can be avoided with the use of standards and the comparison of the quantum yields of the standard and the sample. The method for calculating the quantum used in this dissertation is given by Horiba Jobin Yvon [9]. The equation for calculation the quantum yield is given below:

$$\Phi_{sample} = \Phi_{STD} \cdot \frac{J_{sample}(\nu)d\bar{\nu}}{J_{STD}(\nu)d\bar{\nu}} \cdot \frac{(J_{abs})_{STD}}{(J_{abs})_{sample}} \cdot \left(\frac{\eta_{sample}}{\eta_{STD}}\right)^2 \qquad Equation\ 2.17$$

where,

$\Phi_{STD} =$ Quantum yield of the standard

J_{sample} = Area under the fluorescence emission curve for the sample

$J_{STD} =$ Area under the fluorescence emission curve for the standard.

$(J_{abs})_{STD} =$ Absorbance of the standard

$(J_{abs})_{sample} =$ Absorbance of the sample

$\eta_{sample} =$ Refractive index of the solvent used for the sample.

η_{STD} = Refractive index of the solvent used for the standard.

A standard with a known quantum yield is used and compared to the sample with an unknown quantum yield. Both the sample and the standard are prepared with similar absorbances. The fluorescence is measured with the Fluoromax-2 fluorimeter for both the standard and the sample with the same slit settings and integration times. The areas under the fluorescence curves are measured and used in Equation 2.17. Low absorbances are used to prevent reabsorption of fluorescence and other spurious effects that may affect the quantum yield measurement.

2.4.1 General Formulas for One-Photon and Multi-Photon Transition Strengths

Before embarking further with this study it is essential to continue our overview with an in-depth summary of the transition probability of a molecule. This quantity is related to many of the intensity factors that are experimentally measured in the lab e.g. the absorption cross-section, the molar extinction coefficient and the radiative lifetime. The transition probability μ is measured in Debyes (1D=0.3935 a.u. = 1 x 10^{-18} esu cm = 3.336 x 10^{-30} Coulomb m). However, there is often confusion and discrepancy surrounding these intensity factors. The goal is to highlight some of the subtleties of these terms [10].

1.) Transition moment for electric dipole transitions

$$\mu_{i,v_i;j,v_j} = \langle i, v_i | \vec{\boldsymbol{\mu}} | j, v_j \rangle \qquad Equation\ 2.18$$

$$\vec{\boldsymbol{\mu}} \equiv e \sum_{k=1}^{n} \vec{\boldsymbol{r}}_k$$

$n\ is\ the\ number\ of\ electrons.$

$\vec{\boldsymbol{\mu}}$ is the one-electron vector operator and its matrix elements may simplified using the Wigner-Eckart Theorem and standard angular momentum techniques

2.) The radiative lifetime τ_i is the rate the population of level i decays

$$N_i(t) = N_i^0 \exp\left(-\frac{t}{\tau_i}\right) \qquad Equation\ 2.19$$

$$N_i^0 = the\ population\ of\ level\ i\ at\ t = 0.$$

3.) Transition probabilities (Einstein spontaneous emission coefficient A_{ij} in the absence of collisions, non-radiated decay processes and stimulated emission

Energy level i decays at a rate $\tau_i^{-1} = \sum_j A_{ij}$, where

$$A_{ij} = \left|\mu_{ij}\right|^2 v_{ij}^3 \left[\frac{8\pi^2}{3\hbar\varepsilon_0}\right] \qquad Equation\ 2.20$$

$$\left|\mu_{ij}\right|^2 = \sum_{M_j=M_i-1}^{M_i+1} \left|\langle iM_i|\,\vec{\boldsymbol{\mu}}\,|jM_j\rangle\right|^2$$

$$A_{ij} = 3.137 \times 10^{-7} \left|\mu_{ij}\right|^2 v_{ij}^3 \ s^{-1}$$

4.) Einstein stimulated emission/absorption, B_{ij}

$$B_{ij} = \left|\mu_{ij}\right|^2 / (6\hbar\varepsilon_0 c)$$

$B_{ij}\rho(v_{ij})$ $\quad i \to j$ transition rate for a molecule stimulated by a radiation field with energy density ρ (energy per unit volume per unit frequency, in cm^{-1} units

$$W_{ij} = N_i B_{ij}\, \rho(v_{ij})$$

W_{ij} is the rate, molecules/s or photons/s participating in the $i \to j$ stimulated process.

$$B_{ij} = \frac{g_j}{g_i} B_{ji}$$

$$B_{ij} = 6.283 \times 10^8 \left|\mu_{ij}\right|^2 J^{-1} m^3 cm^{-1} s^{-1}$$

2.5 Derivation of Two-Photon Processes

2.5.1 Theoretical Analysis

Two-photon absorption (TPA) involves the simultaneous absorption of two-photons. One photon absorption (OPA) is related to the first order polarizability and $\chi^{(1)}$. Therefore, the selection rules for OPA and TPA are different, since TPA is related to the third order polarizability $\chi^{(3)}$ and OPA is related to $\chi^{(1)}$.

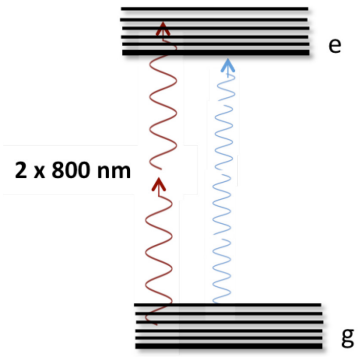

Figure 2.1. A schematic of the two-photon absorption process compared to OPA. The population is excited from the ground to the excited state either by a high energy photon or two photons at half the energy of the transition.

As stated earlier, for the macroscopic treatment the interaction is governed by the equation, $P(t) = \chi^{(1)} E(t)$, which can be expanded as a power series [11].

$$P(t) = \epsilon_0 \left[\chi^{(1)} E(t) + \chi^{(2)} E^2(t) + \chi^{(3)} E^3(t) + \cdots\right] \qquad Equation\ 2.21$$

The real part of the third order terms represents parametric processes, while the imaginary parts represent the non-parametric processes such as two-photon absorption. Kogej et al calculate the imaginary susceptibility using the sum over states method [12], which leads to

$$I\,\gamma(-\omega;\ \omega,-\omega,\omega) = \qquad Equation\ 2.22$$

$$Im\ P\left[\begin{array}{ll} \dfrac{M_{ge}^2\Delta\mu_{ge}^2}{(E_{ge}-\hbar\omega-i\Gamma_{ge})(E_{ge}-2\hbar\omega-i\Gamma_{ge})(E_{ge}-\hbar\omega-i\Gamma_{ge})} & D \\ +\sum_{e\prime}\dfrac{M_{ge}^2M_{ee\prime}^2}{(E_{ge}-\hbar\omega-i\Gamma_{ge})(E_{ge}-2\hbar\omega-i\Gamma_{ge\prime})(E_{ge}-\hbar\omega-i\Gamma_{ge})} & T \\ -\dfrac{M_{ge}^4}{(E_{ge}-\hbar\omega-i\Gamma_{ge})(E_{ge}-\hbar\omega-i\Gamma_{ge})(E_{ge}-\hbar\omega-i\Gamma_{ge})} & N \end{array}\right]$$

which is given in terms of γ and where D is the dipolar term. This term is present exclusively in noncentrosymmetric systems. T is a term that is dependent on the coupling between two excited states and there is a sum over the intermediate states e'. N is called the negative term and makes no contribution to TPA because it only involves one-photon resonances.

The two terms we are most interested in are the D and T terms, which we can relate to the molecular symmetry and dipolar and two-photon terms discussed earlier. TPA selection rules also depend on molecular symmetry properties. M is transition moment between the ground state and state e, and $\Delta\mu_{ge}$ is difference between the transition moments of the ground state and state e [12].

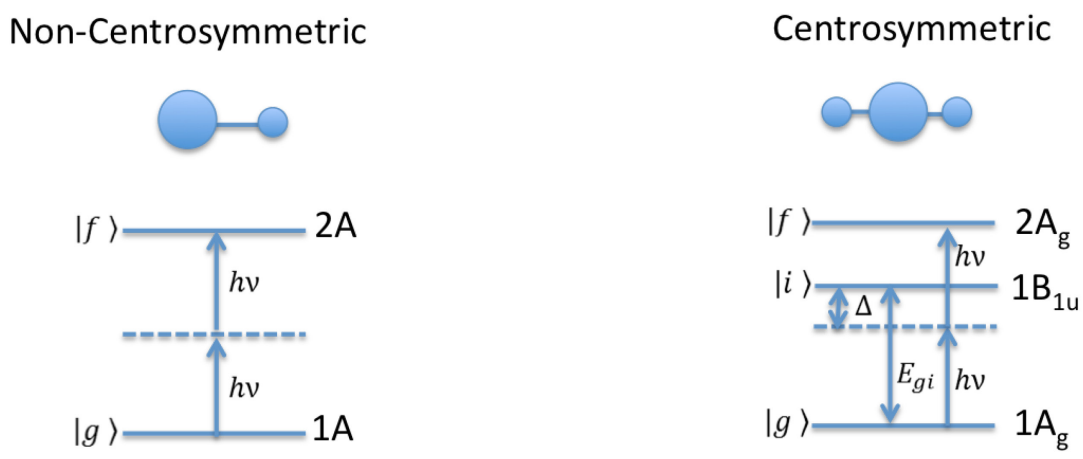

Figure 2.2. For the non-centrosymmetric case the g←→f transition is electric dipole allowed and the dipolar term of equation is nonzero. Both OPA and TPA transitions are allowed. For the centro-symmetric case, 1 and 2 photon allowed transitions are mutually exclusive, and the conservation of angular momentum becomes (+2, 0, -2), and the transition only occurs if the intermediate state is selection rule allowed.

2.5.2 Quantum Theory of Two-Photon Absorption

The following derivation follows Maria Goeppert-Mayer's original paper, which has been re-printed and uses the method outlined by Boyd [11, 13]. The two-photon cross-section can be derived using the interaction picture and starting with Schrodinger's equation. Second order perturbation theory is used. We will begin with the treatment of one-photon absorption in the interaction picture and follow it by deriving two-photon absorption, which follows naturally within this treatment.

To begin this derivation it is natural to start with one photon absorption, which will be derived first, and then proceed to the derivation of two-photon absorption. Second order perturbation theory is used to derive TPA. Using the time dependent Schrodinger's equation, we begin with the time dependent Hamiltonian in the interaction representation [11]:

$$i\hbar\frac{\partial\psi(\vec{r},t)}{\partial t}=\hat{H}\psi(\vec{r},t)$$

The Hamiltonian is given as:

$$\hat{H}=\hat{H}_0+\hat{V}(t)$$

The interaction energy and the electric dipole approximation are:

$$V(t)=-\hat{\mu}\tilde{E}(t),\quad where\quad \hat{\mu}=-e\hat{r}$$

The electric field is of the form:

$$\tilde{E}(t)=Ee^{-i\omega t}+c.c.$$

The wavefunctions are

$$\psi_n(\vec{r},t)=u_n(\vec{r})e^{-i\omega_n t},\quad where\quad \omega_n=E_n/\hbar$$

This wavefunction satisfies the eigenvalue equation and this wavefunction will safisfy the time dependent Schrodinger equation.

$$\hat{H}_0u_n(\vec{r})=E_nu_n(\vec{r})$$
$$i\hbar\frac{\partial\psi(\vec{r},t)}{\partial t}=\left(\hat{H}_0+\hat{V}(t)\right)\psi(\vec{r},t)$$

We can express the wavefunctions as linear combinations to get:

$$\psi(\vec{r},t)=\sum_l a_l(t)u_l(\vec{r})e^{-i\omega_l t}$$

By substituting the wave function into the time dependent Schrodinger equation, the time-dependent Schrodinger equation becomes:

$$i\hbar\left(\sum_l\frac{da_l(t)}{dt}u_l(\vec{r})e^{-i\omega_l t}+\sum_l(-i\omega_l)a_lu_l(\vec{r})e^{-i\omega_l t}\right)=\sum_l a_l(t)E_lu_l(\vec{r})e^{-i\omega_l t}+\sum a_l(t)\hat{V}u_l(\vec{r})e^{-i\omega_l t}$$

In order to simplify this equation, the orthonormality condition is used.

$$\int u_m^*(r)u_l(l)d^3r=\delta_{ml}$$

Equation 1 is simplified to become:

$$i\hbar \frac{da_m}{dt} = \sum_l a_l(t) V_{ml} e^{-\omega_{lm} t}, \quad where \quad \omega_{lm} = \omega_l - \omega_m$$

where,

$$V_{ml} = \int\int u_m^*(\vec{r}) \hat{V} u_l(\vec{r}) d^3 r$$

Now in order to solve this, we resort to using perturbation techniques, where λ is an expansion parameter and we expand $a_m(t)$ in powers of the interaction.

$$a_m(t) = a_m^{(0)}(t) + \lambda a_m^{(1)}(t) + \lambda^2 a_m^{(2)}(t) + ...$$

Eq. 1 now becomes

$$\frac{da_m^{(N)}}{dt} = (i\hbar)^{-1} \sum_l a_l^{(N-1)} V_{ml} e^{-i\omega_{lm} t}, \quad N = 1,2,3,...$$

2.5.2.1 One-Photon Absorption

In order to solve this, we begin with the case for one photon absorption by setting N=1. Below are our initial conditions before the laser is turned on. The entire population is in the ground state, and there is no population in the excited state.

$$a_g^{(0)}(t) = 1$$

$$a_l^{(0)}(t) = 0 \quad for \quad l \neq g$$

The interaction energy between the ground and the excited state is given by:

$$V_{mg} = -\mu_{mg} (E e^{-i\omega t} + E^* e^{i\omega t})$$

Eq. 1 is now

$$\frac{da_m^{(1)}}{dt} = (i\hbar)^{-1} \mu_{mg} \left[E e^{i(\omega_{mg} - \omega)t} + E^* e^{i(\omega_{mg} + \omega)t} \right]$$

which can now be integrated

$$a_m^{(1)}(t) = (i\hbar)^{-1}\mu_{mg}\int_0^t dt'\left[Ee^{i(\omega_{mg}-\omega)t} + E^* e^{i(\omega_{mg}+\omega)t}\right]$$

$$= \frac{\mu_{mg}E}{\hbar(\omega_{mg}-\omega)}\left[e^{i(\omega_{mg}-\omega)t}-1\right] + \frac{\mu_{mg}E^*}{\hbar(\omega_{mg}-\omega)}\left[e^{i(\omega_{mg}+\omega)t}-1\right].$$

Using the rotating wave approximation (RWA), the second term is dropped since we are deriving the equations for OPA. The probability that an atom is in excited state m is:

$$p_m^{(1)}(t) = \left|a_m^{(1)}(t)\right|^2 = \frac{\left|\mu_{mg}E\right|^2}{\hbar^2}\left|\frac{e^{i(\omega_{mg}-\omega)t}-1}{\omega_{mg}-\omega}\right|^2$$

$$= \frac{\left|\mu_{mg}E\right|^2}{\hbar^2}\frac{4\sin^2[(\omega_{mg}-\omega)t/2]}{(\omega_{mg}-\omega)^2} \equiv \frac{\left|\mu_{mg}E\right|^2}{\hbar^2}f(t)$$

where

$$f(t) = \frac{4\sin^2[(\omega_{mg}-\omega)t/2]}{(\omega_{mg}-\omega)^2}$$

2.5.2.2 Two-Photon Absorption

We now solve eq. 1 for N=2 and N=1. We can use $a^{(1)}(t)$ which we already calculated for OPA. Our interaction potential becomes:

$$V_{nm} = -\mu_{nm}\left(Ee^{-i\omega t} + E^* e^{i\omega t}\right)$$

$$\cong -\mu_{nm}Ee^{-i\omega t}$$

Plugging Eq.1, Eq.2 and Eq. 3 into Eq. 4 we get

$$\frac{d}{dt}a_n^{(2)} = (i\hbar)^{-1}\sum_m a_m^{(1)}(t)V_{nm}e^{-i\omega_{mn}t}$$

$$= -(i\hbar)^{-1}\sum_m \frac{\mu_{nm}\mu_{mg}E^2}{\hbar(\omega_{mg}-\omega)}\left[e^{i(\omega_{ng}-2\omega)t} - e^{i(\omega_{nm}-\omega)t}\right]$$

The second term is dropped because it represents the transient response of the system.

$$a_n^{(2)}(t) = \sum_m \frac{\mu_{nm}\mu_{mg}E^2}{\hbar(\omega_{mg}-\omega)}\left[\frac{e^{i(\omega_{ng}-2\omega)t}-1}{\omega_{ng}-2\omega}\right]$$

The probability of the atom being I excited state n is

$$p_n^{(2)}(t) = \left|a_n^{(2)}(t)\right|^2 = \left|\sum_m \frac{\mu_{nm}\mu_{mg}E^2}{\hbar(\omega_{mg}-\omega)}\right|^2 \left|\frac{e^{i(\omega_{ng}-2\omega)t}-1}{\omega_{ng}-2\omega}\right|^2$$

Assuming that level n is a smeared density of states, we are left with:

$$p_n^{(2)}(t) = \left|\sum_m \frac{\mu_{nm}\mu_{mg}E^2}{\hbar(\omega_{mg}-\omega)}\right|^2 2\pi\rho_f(\omega_{ng}=2\omega)$$

The transition rate for two-photon absorption is given by:

$$R_{ng}^{(2)} = \frac{p_n^{(2)}(t)}{t}$$

$$R_{ng}^{(2)} = \sigma_{ng}^{(2)}(\omega)I^2 \quad where \quad I = 2n\varepsilon_0 c\left|E\right|^2$$

$$\sigma_{ng}^{(2)}(\omega) = \frac{1}{4n^2\varepsilon_0^2c^2}\left|\sum_m \frac{\mu_{nm}\mu_{mg}}{\hbar(\omega_{mg}-\omega)}\right|^2 2\pi\rho_f(\omega_{ng}=2\omega)$$

The units for two-photon absorption are given in units of GM (1 GM is 10^{-50}cm^{4}s photon^{-1}). The units were name after Maria Goeppert-Mayer.

While, Goeppert-Mayer knew that two-photon absorption could be experimentally observable, she knew that intense fields would be necessary [13]. Indeed, Goeppert-Mayer was right. Kaiser and Garret didn't experimentally verify two-photon absorption until 30 years after Goeppert-Mayer's seminal work on two-photon absorption in 1961 after the introduction of the optical maser, which produced and collected the intense fields, needed to observed two-photon absorption [13]. They carried out two-photon excitation in CaF_2:Eu^{2+} with red light centered at 6943 Ang. Blue fluorescence was produced at 4250 Ang [14]. These two-photon processes were observed in a real

absorbing state of Eu^{2+}. A log-log plot with a slope of 2 was produced indicating a two-photon event. The efficiency of the process was on the order of 10^{-7}.

2.5.3 Two-Photon Excited Fluorescence

There are several ways in which one can measure the two-photon absorption cross-section (Z-scan, transmission measurements, and two-photon excited fluorescence) [5, 15-17]. Two-photon absorption experiments have evolved to include two-photon excited fluorescence measurements in which the fluorescence of molecules is measured as a function of the input power. The benefits of the two photon excited fluorescence method are better sensitivity than direct measurement of the absorption cross-section, the ability to eliminate the necessity of knowing explicit values for certain laser parameters since it is a comparative method, and the use of two-photon absorbing standards with known two-photon absorption cross-sections. One can plot a Log-log intensity plot and if the plot has a slope of two, it suggests two-photon absorption. One is then able to use known experimental parameters to calculate the absorption cross-section.

2.5.4 Two-Photon Absorption Experimental Set-Up

Figure 2.3 is a schematic of the Two-photon excited fluorescence experiment utilized in the Goodson lab. A diode laser with a center wavelength of 532nm pumps the Kapteyn Murnane Laboratories Ti:Sapphire laser. The Ti:Sapphire laser is tunable from 760nm-830nm. In order to tune the laser wavelength and monitor the quality of the mode-locked beam, we use an Ocean Optics Spectrometer connected to a fiber optic. A simple glass beam splitter directs a fraction of the beam to the fiber optic. While monitoring the beam profile on the computer from the spectrometer, the laser cavity can

be adjusted to change the wavelength by moving the positions of the prism within the laser cavity.

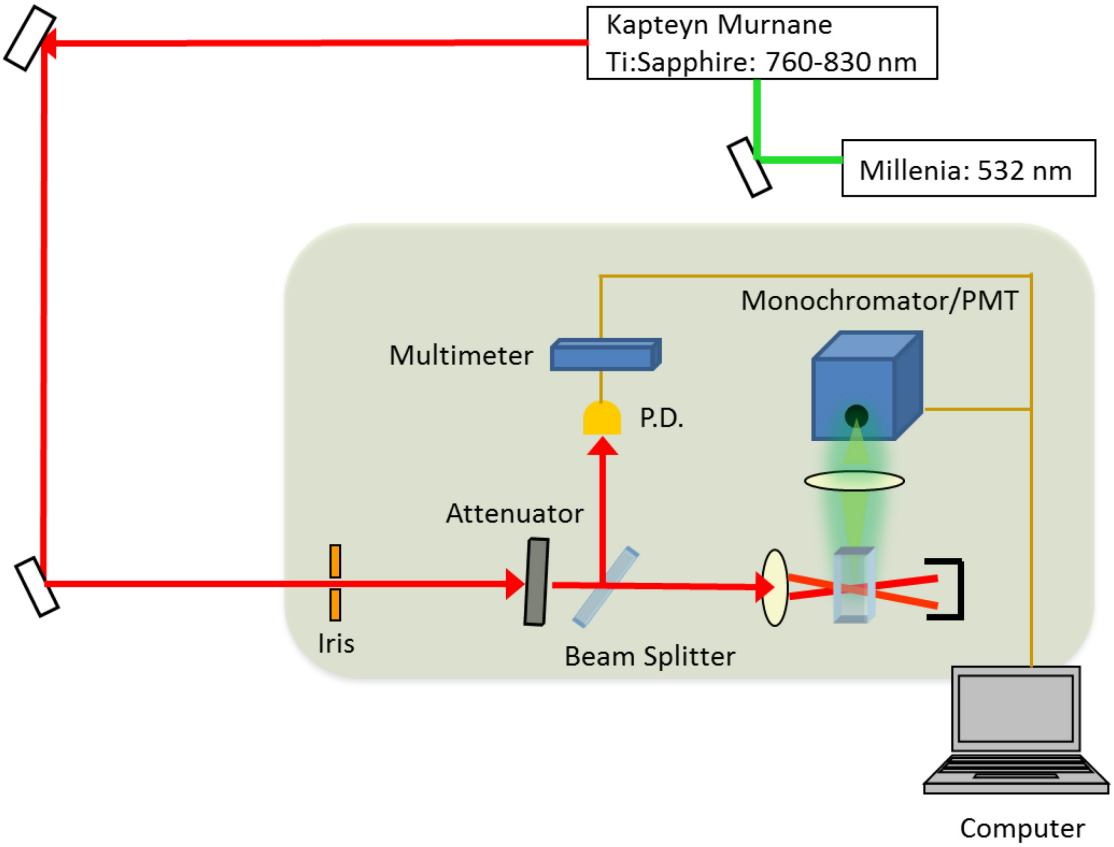

Figure 2.3. Two-photon Absorption experimental set-up.

After the laser cavity the beam travels to a periscope. The periscope changes the beam height and redirects the beam perpendicularly. Mirror 1 is placed at a 45 degree angle and directs the beam parallel to the original direction of the beam from the laser. The beam is directed through a neutral density filter, which is used to adjust the beam intensity. Another glass beam splitter is used after the ND filter to direct a fraction of the beam to the photodiode and the majority of the beam to the sample. The photodiode is connected to a multimeter, which is connected through a GPIB port to the computer. The

largest fraction of the beam is focused through a lens onto the sample. The beam that is not absorbed is directed to a beam dump behind the sample. Fluorescence from the sample is collected perpendicular to the beam path, and is focused through a lens into the monochromator. The monochromator has wavelength selectivity from 400nm-800nm. The intensity of the light is measured by the photomultiplier tube, which is attached to the monochromator. The photomultiplier tube is a Hamatsu, with a sensitivity range from 400nm-800nm.

As stated earlier, the Goodson lab utilizes the two-photon excited fluorescence method (TPEF). The cross-section of a sample is calculated by using a fluorescent standard with a known two-photon absorption (TPA) cross-section at the wavelength of interest. The mathematical relationship that relates the intensity dependent two-Photon excited fluorescence signal to the two-photon absorption cross-section is given in the equation [15]:

$$F(t) = \frac{1}{2}\eta\delta cn\frac{g_p}{\pi\lambda f\tau}\phi\langle P(t)\rangle^2 \qquad Equation\ 2.23$$

Where *F(t)* is the TPEF signal and η is the fluorescence quantum yield, δ is the TPA absorption cross-section, *c* is the concentration of the sample, *n* is the reactive index of the solvent and g_p is the shape factor of the pulse (0.664 for a Gaussian pulse), λ is the wavelength of the laser, f is the frequency of the laser pulses, τ is the pulse duration, ϕ is the collection efficiency of the experimental set-up, and $\langle P(t)\rangle$ is the average intensity of the excitation source. By taking the logarithm of each side of equation, we get:

$$\boldsymbol{Log(F(t))} = \boldsymbol{Log\left(\frac{1}{2}\eta\delta cn\frac{g_p}{\pi\lambda f\tau}\phi\langle P(t)\rangle^2\right)} \qquad Equation\ 2.24$$

We can then plot the log of the intensity versus the logarithm of the input power. This produces a linear plot with a slope of two and the y-intercept is given by comparing the result of the sample with the results of the standard, on can calculate the cross-section of the sample of interest. Using the properties of logarithmic functions, we get

$$Log\big(F(t)\big) = 2Log(\langle P(t)\rangle) + Log\left(\frac{1}{2}\eta\delta cn\frac{g_p}{\pi\lambda f\tau}\phi\right) \qquad Equation\ 2.25$$

2.5.4.1 Sample Two-Photon Absorption Cross-Section Calculation

Experimental Data

Rhodamine B: y = 2.0078x+2.4441

AgDNA: y = 2.0019x+2.9525

$$Log\big(F(t)\big) = 2Log(\langle P(t)\rangle) + Log\left(\frac{1}{2}\eta\delta cn\frac{g_p}{\pi\lambda f\tau}\phi\right) \qquad Equation\ 2.26$$

The calculation is carried out by using a standard with a known quantum yield (η) and a known cross-section at the experimental excitation wavelength (δ) to calculate the collection efficiency of the system (ϕ). We can then equate the experimental value of the y-intercept to the quantity, $Log\left(\frac{1}{2}\eta\delta cn\frac{g_p}{\pi\lambda f\tau}\phi\right)$.

$$2.4441 = Log\left(\frac{1}{2}\eta\delta cn\frac{g_p}{\pi\lambda f\tau}\phi\right) \qquad Equation\ 2.27$$

$$10^{2.441} = \frac{1}{2}\,\eta\delta cnLaser\phi,$$

$$where\ Laser = \frac{g_p}{\pi\lambda f\tau}$$

$$\boldsymbol{\phi = \frac{2 \cdot 10^{2.441}}{\eta\delta cnLaser}} \qquad Equation\ 2.28$$

Since the collection efficiency should be similar from run to run, we can plug ϕ into our equation for the sample. Proceeding as we did above, we equate our experimental y-intercept for the sample to $Log\left(\frac{1}{2}\eta\delta cn\frac{g_p}{\pi\lambda f\tau}\phi\right)$ and get:

$$2.9525 = Log\left(\frac{1}{2}\eta_s\delta_s c_s n_s\frac{g_p}{\pi\lambda f\tau}\phi\right) \qquad Equation\ 2.29$$

$$10^{2.9525} = \frac{1}{2}\,\eta\delta cnLaser\phi \qquad Equation\ 2.30$$

Plugging in ϕ

$$10^{2.9525} = \tfrac{1}{2}\,\eta\delta cnLaser\frac{2\cdot 10^{2.441}}{\eta\delta cnLaser}, \qquad Equation\ 2.31$$

where the laser parameters cancel out. We can now plug in the known quantities to solve for the cross-section. $\eta_s\delta_s = 210\ GM$

$\eta_s\delta_s$ = 210 GM
c_s = 1.01 x 10^{-6} M
n_s = 1.329
c =.87 x 10^{-6} M
n = 1.33

Now that the theory and experimental details have been described, we present the data for the two groups of novel materials that were studied (DCDHF fluorophores and DNA templated nanoclusters).

2.6 DCDHF Fluorophores

2.6.1 Introduction

The motivation for this next two-photon absorption study is also the need for bright/stable dyes for biological imaging, more specifically two-photon excited microscopy. An ideal dye has a large TPA cross-section and excellent single-molecule fluorescence properties (high quantum-yield and photostability). To gain a better understanding of these novel fluorophores we studied a group of molecules with an amine donor and a dicyanodihydrofuran (DCDHF) acceptor. These molecules tend to be dipolar, generally have large ground state dipole moments, and have some viscosity dependence and some hyperpolarizability [18, 19]. This work fits into the scope of the work completed in the Goodson group, in terms of exploring novel materials.

Figure 2.4 gives a schematic of the amine donor and DCDHF acceptor that are connected by a π-conjugated linker. The R1–R4 groups can be modified (usually without affecting the photophysics) in order to add reactive functionality or increased solubility [19]. The naming scheme used in this paper specifies the π system: "DCDHF-(π unit closest to acceptor)-...-(π unit closest to donor)" with the π units denoted P = phenylene, V = vinyl, T = thiophene, N = naphthalene, A = anthracene; the amine donor is not specified because it is present in all structures [20, 21].

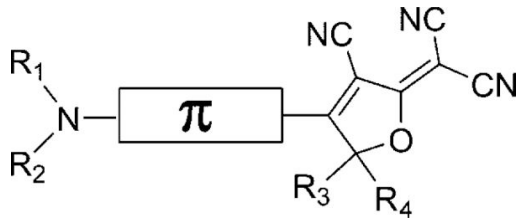

Figure 2.4. This is a schematic structure of the DCDHF fluorophores. A π-conjugated linker connects the amine donor and DCDHF acceptor [18].

There have been few TPA studies conducted on these types of molecules [22]. Similar dipolar molecules also exhibit large TPA cross-sections ~450 GM. Most of the studies conducted have been studies to test the single molecule properties. These tests were conducted in solution and in thin film. Basic steady state optical properties have also been covered, as well as, fluorescence lifetime measurements [19].

Below we present the steady, two-photon excited fluorescence curves and TPA cross-sections.

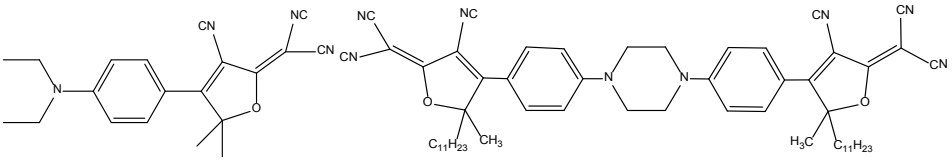

Figure 2.5. The monomer and dimer are given.

The particular DCDHF molecules that we focus on are given in Figure 2.5. The molecular structures of both LCA and LCC are given in Figure 2.5.

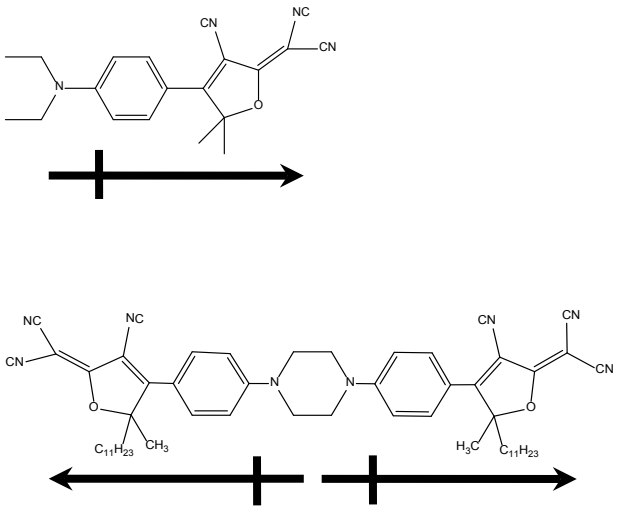

Figure 2.6. The dipole of the D-A motif for LCA and the dipoles of the A-D-A motif for LCC.

2.6.2 Results and Discussion

The first study that was conducted was a monomer and dimer study. It has been shown that designing molecules with symmetric (D-A-D and A-D-A) and non-symmetric (D-A) motifs enhance the transition dipole matrix elements [23]. Because these molecules are also dipolar, most measurements were conducted with pyridine as the solvent. The donor acceptor enhancement effect on the transition dipole moment seemed largest when using Pyridine to solvate LCA and LCC.

Steady state measurements were carried out using the methods and instrumentation given in Sections 2.3 and 2.4. The extinction coefficient of LCA is 64,377 $M^{-1}cm^{-1}$. The extinction coefficient of LCC is 84,800 $M^{-1}cm^{-1}$. The quantum yield was also calculated. The quantum yield for LCA is relatively low, at 0.00798. While the quantum yield for LCC is 0.00954. Below are the absorption and fluorescence curves for both LCA and LCC. LCA has an absorption peak centered at 514 nm. The fluorescence max is

centered at 556 nm. The absorption and fluorescence profiles of LCC are very similar to LCA. The absorption peak of LCC is located at 518 nm, while the fluorescence peak of LCC is centered at 545 nm.

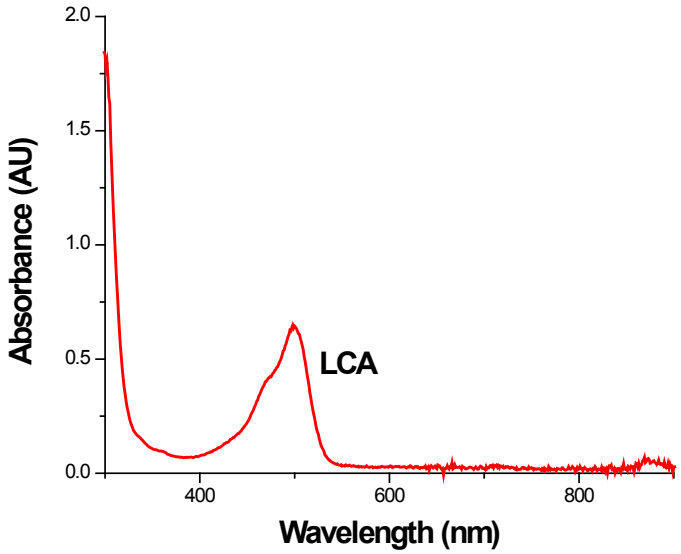

Figure 2.7. The Absorption maximum of LCA is λ_{max}=514 nm.

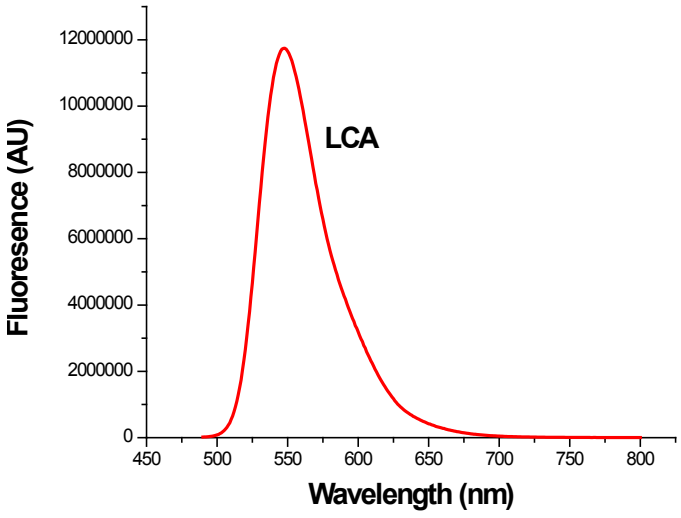

Figure 2.8. The fluorescence maximum of LCA is λ_{max}=556 nm.

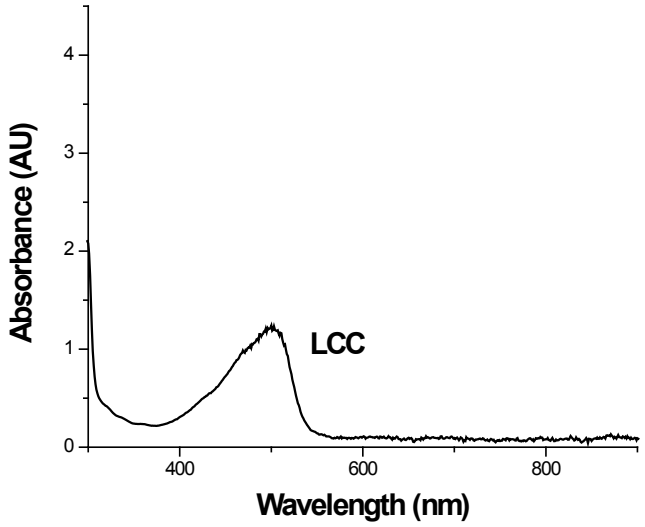

Figure 2.9. The absorption maximum of LCC is λ_{max}=518 nm.

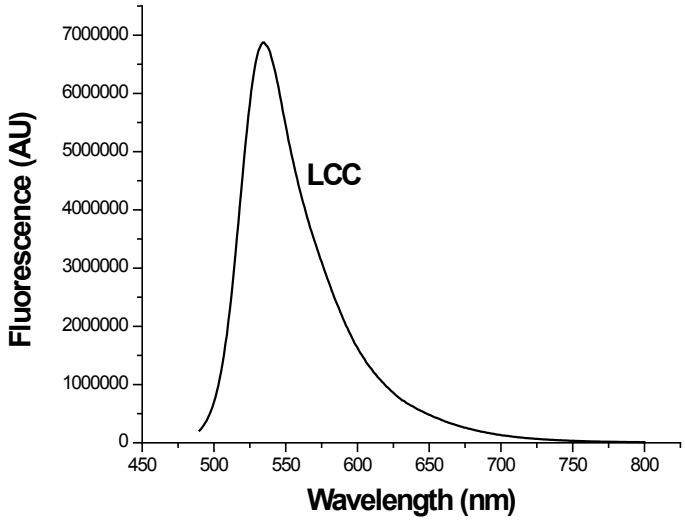

Figure 2.10. The fluorescence maximum of LCC is λ_{max}=545 nm.

2.6.2.1 Two-Photon Absorption

It is hypothesized that for these two molecules that the TPA cross-section of LCC should be larger than LCA. LCC is a centrosymmetric molecule and two-photon absorption should occur via intermediate states of the system. This enhances the T term in Equation 2.22 [23]. LCA, a dipolar molecule, lacks this intermediate state. This may explain why TPA cross-sections for centrosymmetric chromophores tend to be larger than cross-sections for non-centrosymmetric molecules. Again all the samples were measured in pyridine.

The two-photon excited fluorescence showed concentration dependence. At a concentration of 10 μM, the fluorescence peak was centered at 468 nm. This is given in Figure 2.11. At higher concentrations this peak was blue shifted and another peak also appeared. Below in Figure 2.12 the original peak shifts from 468 nm to 448 nm and a new peak arises at 546 nm.

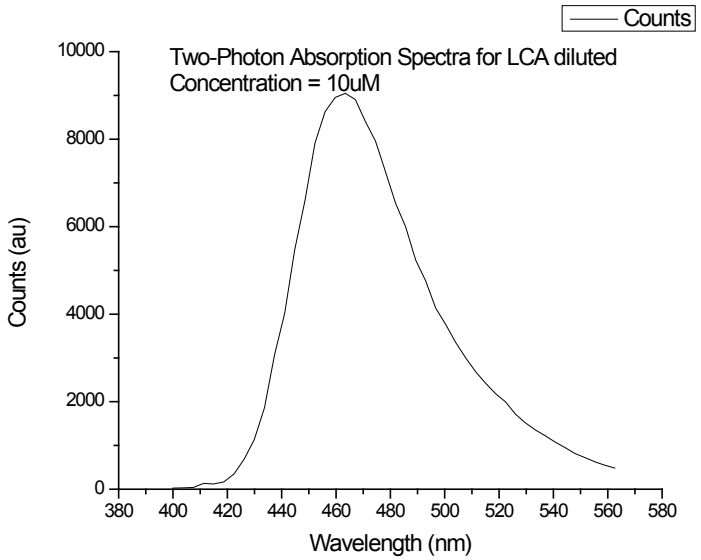

Figure 2.11. The two-photon excited fluorescence curve of LCA is given measured at a concentration of 10 μM.

2.6.2.2 Two-Photon Cross-Section Data

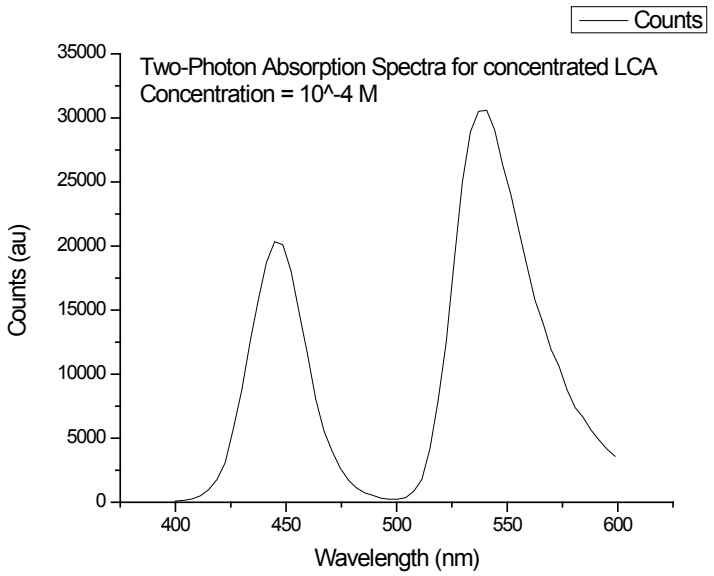

Figure 2.12. As concentration is increased another fluorescence peak is formed.

We measured the lower concentration samples. The cross-sections were calculated for 800 nm excitation. LCA had a cross-section of 45.6 GM and LCC had a cross-section of 105 GM. Figure 2.13 give the TPA cross-section of both LCA and LCC as a function of wavelength. Unfortunately due to the limitations of the experimental setup in Section 2.5.4, we were unable to probe the two-photon excited fluorescence at exactly twice the absorption peak of ~514 nm for both samples. While the cross-sections aren't extremely large, these samples may be interesting ETPA candidates. The dipolar properties of the molecules may present interesting properties worth exploring with non-classical fields.

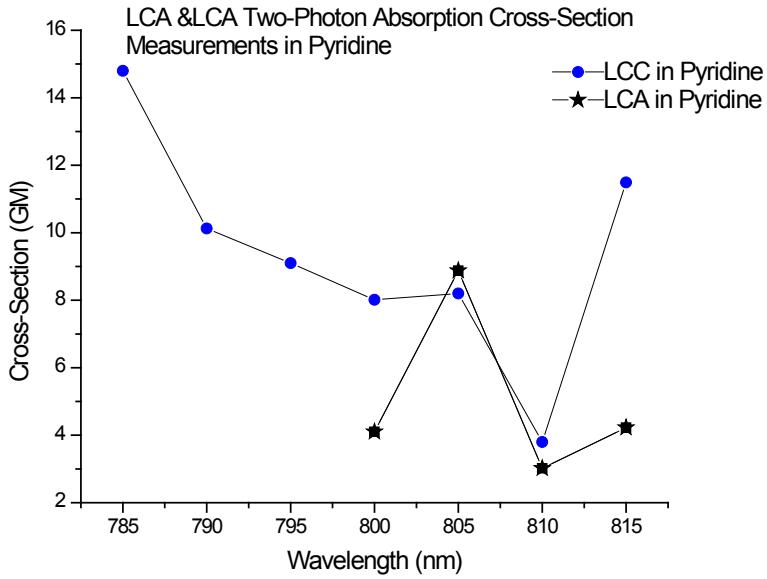

Figure 2.13. The fluorescence of LCA is given as a function of concentration. As concentration is increased another fluorescence peak is formed.

2.7 DNA-templated silver nanoclusters

2.7.1 Introduction

While organic dyes are currently the most prevalent fluorophores in the field, organic dyes suffer from both photobleaching and low photostability. While quantum dots are quite stable and have high fluorescent quantum yields, they are large (10-35nm) [24], which makes them impractical for use in biological samples because of their limited mobility in cellular environments [25]. Quantum dots also pose health and toxicity concerns because the heavy metals that are used to synthesize quantum dots may be toxic to biological systems [24, 26].

Metal nanoclusters are smaller than metal nanoparticles [27]. Generally clusters are considered to be less than 3 nm in diameter and as a result, surface plasmons are not created [28]. Of the metal nanoclusters, gold nanoclusters are the most extensively

studied. There is a crystal structure, they are relatively easy to synthesize, separate and characterize [29, 30]. Small metal nanoclusters have received much interest over the last two decades [29, 31-33]. Metal nanoclusters can be separated into two groups based on the method of synthesis. Monolayer-protected clusters (MPCs) are stabilized by ligands and by stable "Magic Number" configurations of the metal atoms in the core of the cluster [30].

While gold monolayer-protected nanoclusters do exhibit large TPA cross-sections, the clusters are plagued with low (on the order of 10^{-4}) fluorescent quantum yields [4]. Although much more efficient than the quantum yields of bulk gold (10^{-10}) [34], such low fluorescence is not ideal for biological imaging applications. The efficiency of gold as a two-photon absorber demonstratively depends upon the size of the clusters [35, 36]. TPA cross-sections were measured on the order of 10^6 GM, which are some of the largest cross-sections measured. This large TPA efficiency enables nonlinear optical applications such as multi-photon imaging, nanolithography, and optical power limiting. However, they have a very small quantum yield [4].

This fact led researchers to explore the possibility of developing silver nanoclusters. Silver is very similar to gold because of their similar electronic structures. Both atoms have one free electron per atom. While monolayer protected silver cluster have been synthesized, these particular samples were not stabilized with ligands. Templated nanoclusters are stabilized using dendrimers, biological material and other large molecules [37, 38]. Instead of using ligands as a stabilizing agent, DNA was used [39]. Originally developed as biological beacons, DNA-templated clusters seem to be a great candidate for two-photon biological imaging applications because of their highly

fluorescent nature [39]. Ultra-fast work has been conducted to develop a clearer picture of the absorption and fluorescence mechanism of these particles [40].

Silver monolayer-protected clusters lack stability and often aggregate and form into larger particles [41]. Unlike gold, less is known about silver clusters. While silver MPCs have been synthesized [41, 42], the resulting forms are not stable [41]. Although silver is predicted to behave much like gold, the ideal number configuration of the silver core atoms has not been calculated or proven experimentally yet. Silver MPCs have higher fluorescence quantum yields than gold, but the value is still much too low to consider the use of silver nanoclusters for practical imaging applications [43].

An alternative method to ligand protected nanoclusters, are oligonucleotides. Unlike monolayer-protected clusters, these DNA-templated silver nanoclusters exhibit high stability and large fluorescent quantum yields [43]. The clusters are formed on a 42-base nucleotide (a 12-base nucleotide contains the Ag nanoclusters and the 30-base nucleotide is the hybridization sequence). Gwinn and colleagues have demonstrated that the fluorescence of DNA-templated silver nanoclusters is a weak green fluorescence. This fluorescence can be tuned by changing the sequence of the DNA bases [43].

Hybridized DNA-templated silver samples self-assemble into enhance fluorescent clusters when other DNA-templated silver clusters; however, by adding the complementary ssDNA to the silver template enhances the fluorescence. Such samples that must be hybridized provide on and off switching for the fluorescence. The fluorescence intensity of these clusters depends on the sequence of the DNA [44] and is enhanced by guanine overhangs.

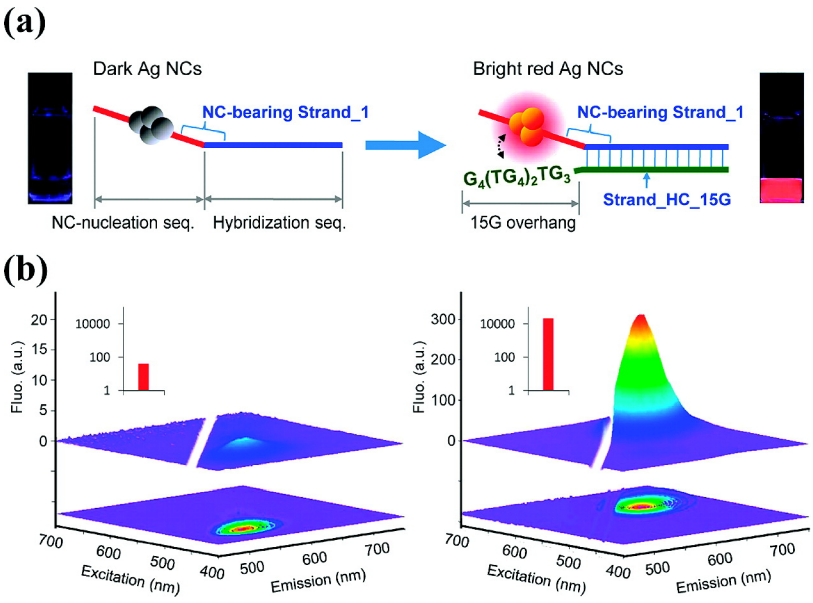

Figure 2.14. A schematic of the fluorescence enhancement induced by the 15G overhang. The red emission resulting from the activated clusters is also pictured along with the emission graph [44].

2.7.2 Results and Discussion

We now consider and study both the linear and the non-linear optical properties of these structures using both steady-state and ultrafast techniques. Probing the nonlinearities of such systems will help researchers fully understand and grasp the scientific principles that govern these small clusters. In particular, we examine at the steady state and the two-photon absorption efficiencies of the hybridized DNA-templated nanoclusters. High TPA efficiencies are useful for nonlinear optical applications such as multi-photon imaging, nanolithography, and optical power limiting.

This work presents the fluorescence enhancement that occurs with the addition of the G15 overhang. The two-photon excited fluorescence method is used to create a log(power) – log(counts) plot with a slope of 2, which suggests a two-photon absorption process. The TPA cross-section was then calculated for both the dialyzed and non-

dialyzed sample at several different wavelengths. Lastly, the stability was examined by observing the fluorescence spectra over the course of several days.

2.7.2.1 Steady State Results

Please refer to Sections 2.3 and 2.4 for detailed descriptions of the experimental techniques mentioned in this section. An Agilent 8432 UV-Vis absorption spectrometer, was used to measure the one-photon absorption spectra of the samples, and the fluorescence spectra was measured using a Fluoromax-2 Spectro-fluorophotometer. All measurements were carried out at room temperature. Samples were prepared and stored in a 1 cm quartz cell during the experiments. We received two samples a filtered and a filtered and dialyzed sample.

Figure 2.15 shows the optical absorption and steady-state emission spectra obtained for non-activated ssDNA with Ag and the activated dsDNA with Ag. The steady state absorption for the dialyzed sample is also given in Figure 2.16. Absorption spans the visible region with a shoulder at 450 nm for the non-activated sample. Once the sample is activated another shoulder appears at 580 nm.

Figure 2.15 also shows the emission spectra obtained after excitation at 430 nm. The non-activated samples emit weak green fluorescence. However, once the samples are activated this fluorescence is shifted to 630 nm and is enhanced. Figure 2.14 shows the ssDNA with silver, the G15 complement and the activated dsDNA with silver under UV light. The activated dsDNA with the G15 overhang is the only fluorescent sample with red/orange emission. The fluorescence quantum yield was 0.01, one hour after activation. The fluorescence quantum yield was measured using the gradient method described in Section 2.4.

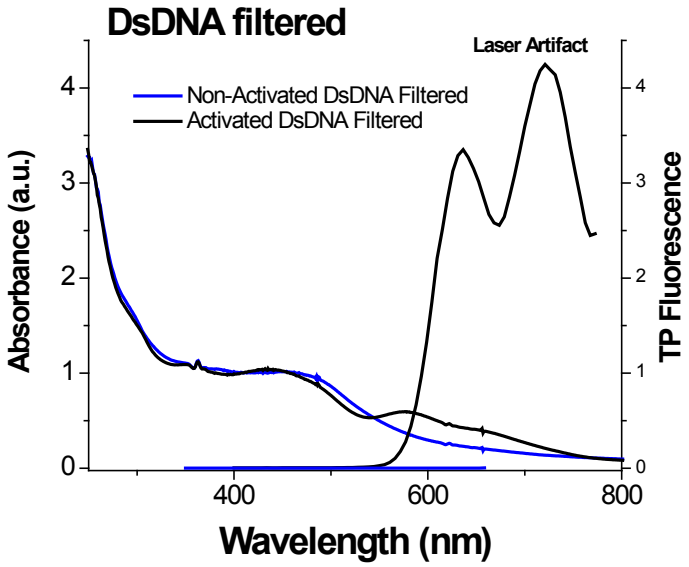

Figure 2.15. The absorption and emission of the non-activated and activated filtered DsDNA.

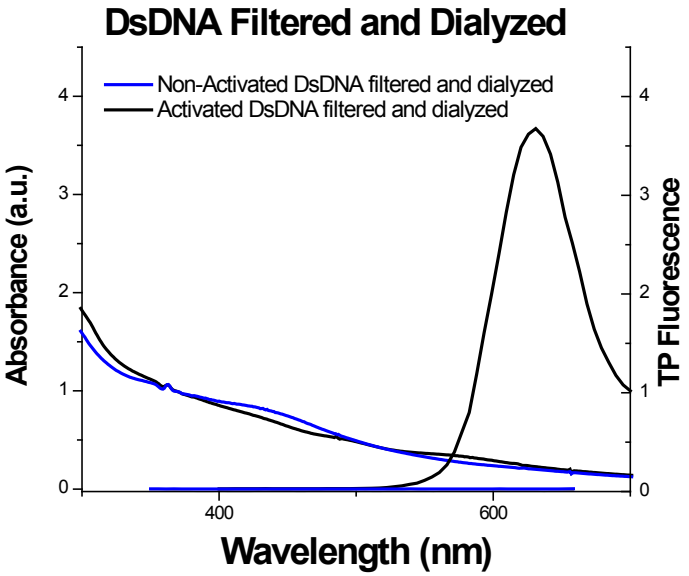

Figure 2.16. The absorption and emission of the non-activated and activated filtered DsDNA.

Little is known about the process of the fluorescence enhancement, although several theories have been proposed to describe it. These include: the formation of secondary structures that favor the formation of red-emitting nanoclusters, conformational changes in the DNA, and electron transfer from guanines to nanoclusters (cite Nanoletters). Figure 2.14 is a schematic of the theorized method of enhancement.

2.7.2.2 Two-Photon Absorption Results

The two-photon measurements were carried out on the experimental set-up described in detail in Section 2.5.4. Figure 2.15 and Figure 2.16 give the two-photon fluorescence spectra of the filtered and the filtered and dialyzed samples respectively. The two-photon absorption excited fluorescence peak is located at 630 nm for both samples. In Figure 2.18, some two-photon excited fluorescence is visible from the non-activated sample at 675nm. Figure 2.19 shows the pump power dependence of the fluorescence at 630nm for the filtered and dialyzed sample. The slope is ~2 suggesting two-photon excited emission. The method for calculating the TPA cross-section is the comparative two-photon excited fluorescence method with H2TPP in toluene as the standard.

Figure 2.19 shows the pump power dependence of the fluorescence at 630 nm is shown. The slope is ~2 suggesting two-photon excited emission. The method for calculating the TPA cross-section is the comparative two-photon excited fluorescence method with H2TPP in toluene as the standard. The TPA action cross-section at 800 nm for the activated dsDNA was determined to be 200 GM. This is a large TPA cross-section and suggests the Ag-templated DNA samples are viable fluorophores for multi-photon imaging.

The TPA action cross-section at 790 nm for the activated filtered dsDNA was determined to be 4658.13 GM. The cross-section for the filtered and dialyzed dsDNA is 1317.99 GM at the same wavelength. The TPA cross-sections are given from 790-820nm for both the filtered and filtered dialyzed samples are given in Figure 2.20. This is a large TPA cross-section and suggests the Ag-templated DNA samples are viable fluorophores for multi-photon imaging.

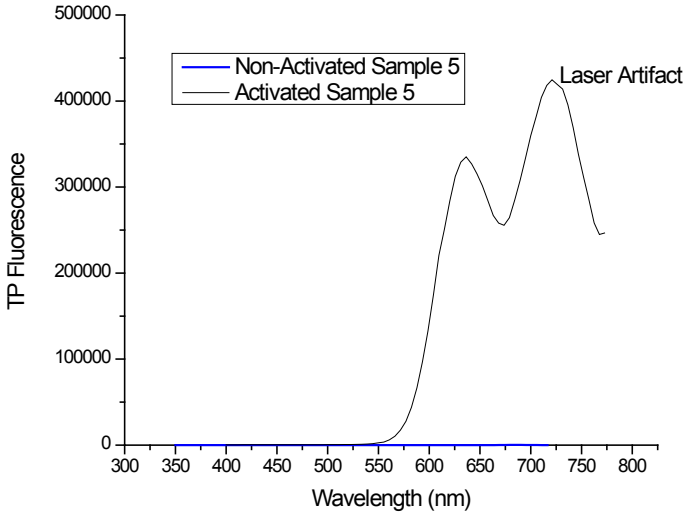

Figure 2.17. The two-photon excited fluorescence of the dsDNA filtered sample.

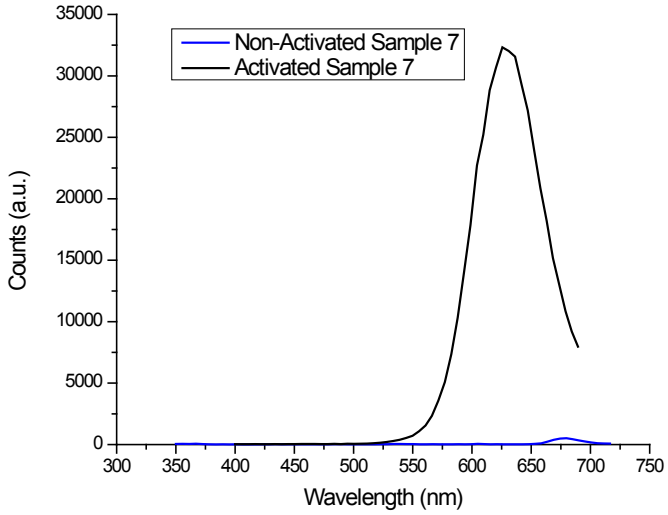

Figure 2.18. The two-photon excited fluorescence of the dsDNA filtered and dialyzed sample.

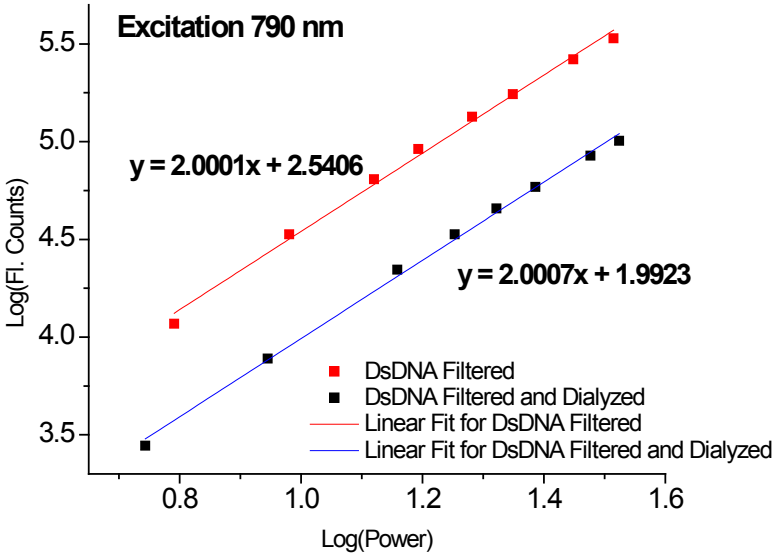

Figure 2.19. The log-log plot comparing the filtered DsDNA and the filtered dialyzed DsDNA.

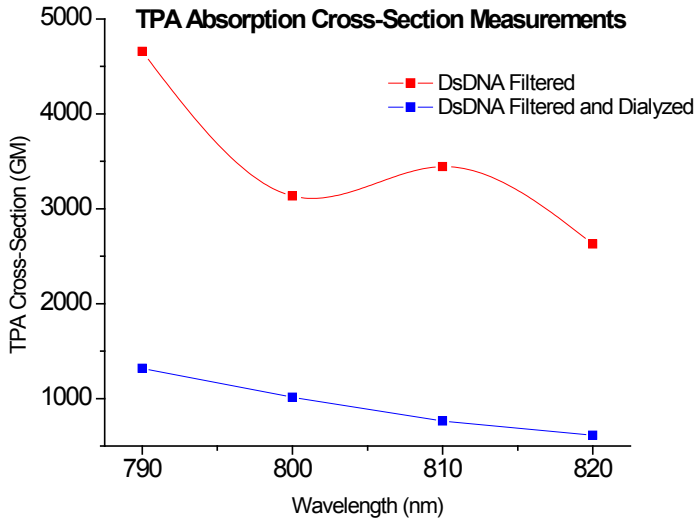

Figure 2.20. The two-photon absorption cross-sections of the DsDNA filtered and DsDNA filtered and dialyzed nanoclusters given in GM over the range of 40nm from 790 nm to 810 nm.

Two-Photon Absorption Cross-Section (GM)		
	DsDNA Filtered	DsDNA Filtered and Dialyzed
790 nm	4658.13	1317.99
800 nm	3135.09	1013.1
810 nm	3443.67	764.05
820 nm	2627.6	612.15

Table 2.1. The two-photon absorption cross-sections of the DsDNA filtered and DsDNA filtered and dialyzed nanoclusters given in GM over the range of 40nm from 790 nm to 810 nm.

2.7.2.3 Time Dependent Fluorescence Stability Study

While these clusters are highly fluorescent, there seemed to be issues with stability. In order to study the stability, we studied the activated cluster's fluorescence since a molecule's fluorescence is much more sensitive to measurements of stability than

absorption. The fluorescence measurements were made on the Fluoromax over the course of 4 days.

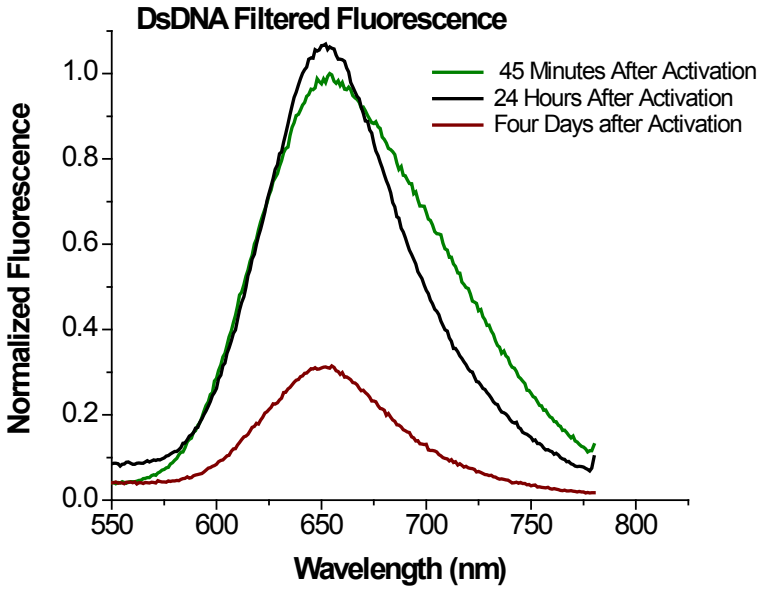

Figure 2.21. The filtered dsDNA fluorescence over a period of 96 hours. The peak is centered at 650 nm. After 24 hours, the intensity of the fluorescence decreases although the peak does not shift.

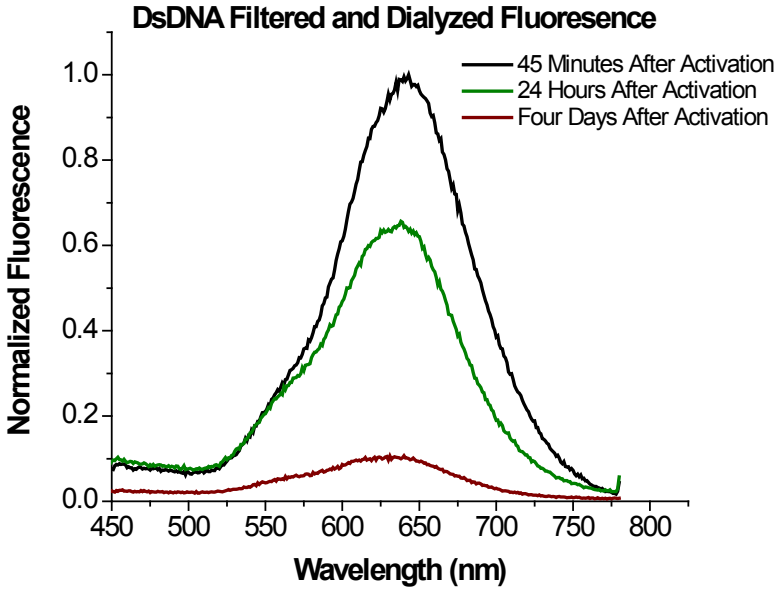

Figure 2.22. The dsDNA filtered and Dialyzed fluorescence over a period of 96 hours.

While the silver nanoclusters were bright, there are still too many unknowns about structure, stability and absorption mechanism to make it a good candidate for studying entangled two-photon absorption.

2.8 Conclusions

Both DCDHF flurophores and metal nanoclusters present new and novel TPA molecules. The DCDHF fluorophore were more promising. Their relatively large cross-sections and better characterization make them better candidates. As such, we will be studying their ETPA properties in Chapter 3. We explored their unique optical properties in hopes of finding new candidates for studying entangled two-photon absorption. Unfortunately, due to lack of proper characterization and lack of stability the silver DNA template nanoclusters would be unsuitable for further studies.

References:

[1] A. Bhaskar, R. Guda, M. M. Haley, and Goodson, "Building Symmetric Two-Dimensional Two-Photon Materials," *Journal of the American Chemical Society,* vol. 128, pp. 13972-13973, 2006/11/01 2006.

[2] A. Bhaskar, G. Ramakrishna, Z. Lu, R. Twieg, J. M. Hales, D. J. Hagan*, et al.*, "Investigation of Two-Photon Absorption Properties in Branched Alkene and Alkyne Chromophores," *Journal of the American Chemical Society,* vol. 128, pp. 11840-11849, 2006/09/01 2006.

[3] G. Ramakrishna, A. Bhaskar, P. Bauerle, and T. Goodson, "Oligothiophene Dendrimers as New Building Blocks for Optical Applications†," *The Journal of Physical Chemistry A,* vol. 112, pp. 2018-2026, 2008/03/01 2007.

[4] G. Ramakrishna, O. Varnavski, J. Kim, D. Lee, and T. Goodson, "Quantum-Sized Gold Clusters as Efficient Two-Photon Absorbers," *Journal of the American Chemical Society,* vol. 130, pp. 5032-5033, 2008.

[5] A. Bhaskar, "A Building Block Approach Towards Novel Nonlinear Optical Materials," Ph.D., Department of Chemistry, University of Michigan, 2007.

[6] J. C. Furgal, J. H. Jung, T. Goodson, and R. M. Laine, "Analyzing Structure-Photophysical Property Relationships for Isolated T-8, T-10, and T-12 Stilbenevinylsilsesquioxanes," *Journal of the American Chemical Society,* vol. 135, pp. 12259-12269, Aug 2013.

[7] J. Weiner, P.-T. Ho, and L. Wiley Online, *Light-matter interaction*. Hoboken, N.J.: Wiley, 2003.

[8] D. J. Griffiths, *Introduction to electrodynamics*. Upper Saddle River, N.J.: Prentice Hall, 1999.

[9] "Horiba Jobin Yvon, A Guide to Recording Fluorescence Quantum Yields."

[10] D. P. Craig and T. Thirunamachandran, *Molecular quantum electrodynamics: an introduction to radiation-molecule interactions*. London ; Orlando: Academic Press, 1984.

[11] R. W. Boyd, Knovel, and ScienceDirect, *Nonlinear optics*. Burlington, MA: Academic Press, 2008.

[12] T. Kogej, D. Beljonne, F. Meyers, J. W. Perry, S. R. Marder, and J. L. Brédas, "Mechanisms for enhancement of two-photon absorption in donor–acceptor conjugated chromophores," *Chemical Physics Letters,* vol. 298, pp. 1-6, 12/11/ 1998.

[13] B. R. Masters, P. T. C. So, and I. ebrary, *Handbook of biomedical nonlinear optical microscopy*. New York: Oxford University Press, 2008.

[14] W. Kaiser and C. G. B. Garrett, "Two-Photon Excitation in Ca${\mathrm{F}}_{2}$: ${\mathrm{Eu}}^{2+}$," *Physical Review Letters,* vol. 7, pp. 229-231, 09/15/ 1961.

[15] C. Xu and W. W. Webb, "Measurement of two-photon excitation cross sections of molecular fluorophores with data from 690 to 1050 nm," *J. Opt. Soc. Am. B,* vol. 13, pp. 481-491.

[16] C. Xu, W. Zipfel, J. B. Shear, R. M. Williams, and W. W. Webb, "Multiphoton fluorescence excitation: new spectral windows for biological nonlinear microscopy," *Proceedings of the National Academy of Sciences,* vol. 93, pp. 10763-10768, 1996.

[17] N. S. Makarov, M. Drobizhev, and A. Rebane, "Two-photon absorption standards in the 550-1600 nmexcitation wavelength range," *Optics Express,* vol. 16, pp. 4029-4047, 2008/03/17 2008.

[18] S. J. Lord, N. R. Conley, H.-l. D. Lee, S. Y. Nishimura, A. K. Pomerantz, K. A. Willets*, et al.*, "DCDHF Fluorophores for Single-Molecule Imaging in Cells," *ChemPhysChem,* vol. 10, pp. 55-65, 2009.

[19] S. J. Lord, Z. Lu, H. Wang, K. A. Willets, P. J. Schuck, H.-l. D. Lee*, et al.*, "Photophysical Properties of Acene DCDHF Fluorophores: Long-Wavelength Single-Molecule Emitters Designed for Cellular Imaging," *The Journal of Physical Chemistry A,* vol. 111, pp. 8934-8941, 2007/09/01 2007.

[20] U. Gubler, M. He, D. Wright, Y. Roh, R. Twieg, and W. E. Moerner, "Monolithic Photorefractive Organic Glasses with Large Coupling Gain and Strong Beam Fanning," *Advanced Materials,* vol. 14, pp. 313-317, 2002.

[21] K. A. Willets, O. Ostroverkhova, M. He, R. J. Twieg, and W. E. Moerner, "Novel Fluorophores for Single-Molecule Imaging," *Journal of the American Chemical Society,* vol. 125, pp. 1174-1175, 2003/02/01 2003.

[22] O. A. Kucherak, L. Richert, Y. Mely, and A. S. Klymchenko, "Dipolar 3-methoxychromones as bright and highly solvatochromic fluorescent dyes," *Physical Chemistry Chemical Physics,* vol. 14, pp. 2292-2300, 2012.

[23] M. Pawlicki, H. A. Collins, R. G. Denning, and H. L. Anderson, "Two-Photon Absorption and the Design of Two-Photon Dyes," *Angewandte Chemie International Edition,* vol. 48, pp. 3244-3266, 2009.

[24] S. Courty, C. Luccardini, Y. Bellaiche, G. Cappello, and M. Dahan, "Tracking Individual Kinesin Motors in Living Cells Using Single Quantum-Dot Imaging," *Nano Letters,* vol. 6, pp. 1491-1495, 2006/07/01 2006.

[25] E. A. Jares-Erijman and T. M. Jovin, "FRET imaging," *Nat Biotech,* vol. 21, pp. 1387-1395, 11//print 2003.

[26] U. Resch-Genger, M. Grabolle, S. Cavaliere-Jaricot, R. Nitschke, and T. Nann, "Quantum dots versus organic dyes as fluorescent labels," *Nat Meth,* vol. 5, pp. 763-775, 09//print 2008.

[27] S. H. Yau, O. Varnavski, and T. Goodson, "An Ultrafast Look at Au Nanoclusters," *Accounts of Chemical Research,* vol. 46, pp. 1506-1516, 2013/07/16 2013.

[28] L. Shang, S. Dong, and G. U. Nienhaus, "Ultra-small fluorescent metal nanoclusters: Synthesis and biological applications," *Nano Today,* vol. 6, pp. 401-418, 8// 2011.

[29] R. Jin, "Quantum sized, thiolate-protected gold nanoclusters," *Nanoscale,* vol. 2, pp. 343-362, 2010.

[30] Y. Negishi, N. K. Chaki, Y. Shichibu, R. L. Whetten, and T. Tsukuda, "Origin of Magic Stability of Thiolated Gold Clusters: A Case Study on Au25(SC6H13)18," *Journal of the American Chemical Society,* vol. 129, pp. 11322-11323, 2007/09/01 2007.

[31] S. Chen, R. S. Ingram, M. J. Hostetler, J. J. Pietron, R. W. Murray, T. G. Schaaff*, et al.*, "Gold Nanoelectrodes of Varied Size: Transition to Molecule-Like Charging," *Science,* vol. 280, pp. 2098-2101, June 26, 1998 1998.

[32] R. S. Ingram, M. J. Hostetler, R. W. Murray, T. G. Schaaff, J. T. Khoury, R. L. Whetten*, et al.*, "28 kDa Alkanethiolate-Protected Au Clusters Give Analogous Solution Electrochemistry and STM Coulomb Staircases," *Journal of the American Chemical Society,* vol. 119, pp. 9279-9280, 1997/10/01 1997.

[33] T. G. Schaaff, M. N. Shafigullin, J. T. Khoury, I. Vezmar, R. L. Whetten, W. G. Cullen*, et al.*, "Isolation of Smaller Nanocrystal Au Molecules: Robust Quantum Effects in Optical Spectra," *The Journal of Physical Chemistry B,* vol. 101, pp. 7885-7891, 1997/10/01 1997.

[34] A. Mooradian, "Photoluminescence of Metals," *Physical Review Letters,* vol. 22, p. 185, 1969.

[35] G. Ramakrishna, O. Varnavski, J. Kim, D. Lee, and T. Goodson, "Quantum-Sized Gold Clusters as Efficient Two-Photon Absorbers," vol. 130, ed: American Chemical Society, 2008.

[36] O. Varnavski, G. Ramakrishna, J. Kim, D. Lee, and T. Goodson, "Critical Size for the Observation of Quantum Confinement in Optically Excited Gold Clusters," vol. 132, ed: American Chemical Society, 2010.

[37] O. Varnavski, R. G. Ispasoiu, L. Balogh, D. Tomalia, and T. Goodson, "Ultrafast time-resolved photoluminescence from novel metal–dendrimer nanocomposites," *The Journal of Chemical Physics,* vol. 114, pp. 1962-1965, 2001.

[38] J. D. Gilbertson, G. Vijayaraghavan, K. J. Stevenson, and B. D. Chandler, "Air and Water Free Solid-Phase Synthesis of Thiol Stabilized Au Nanoparticles with Anchored, Recyclable Dendrimer Templates," *Langmuir,* vol. 23, pp. 11239-11245, 2007/10/01 2007.

[39] J. Sharma, H.-C. Yeh, H. Yoo, J. H. Werner, and J. S. Martinez, "A complementary palette of fluorescent silver nanoclusters," *Chemical Communications,* vol. 46, pp. 3280-3282, 2010.

[40] S. H. Yau, N. Abeyasinghe, M. Orr, L. Upton, O. Varnavski, J. H. Werner*, et al.*, "Bright two-photon emission and ultra-fast relaxation dynamics in a DNA-templated nanocluster investigated by ultra-fast spectroscopy," *Nanoscale,* vol. 4, pp. 4247-4254, 2012 2012.

[41] S. Kumar, M. D. Bolan, and T. P. Bigioni, "Glutathione-Stabilized Magic-Number Silver Cluster Compounds," *Journal of the American Chemical Society,* vol. 132, pp. 13141-13143, 2010/09/29 2010.

[42] Z. Wu, E. Lanni, W. Chen, M. E. Bier, D. Ly, and R. Jin, "High Yield, Large Scale Synthesis of Thiolate-Protected Ag7 Clusters," *Journal of the American Chemical Society,* vol. 131, pp. 16672-16674, 11/03 2009.

[43] H.-C. Yeh, J. Sharma, J. J. Han, J. S. Martinez, and J. H. Werner, "A DNA–Silver Nanocluster Probe That Fluoresces upon Hybridization," vol. 10, ed: American Chemical Society, 2010.

[44] E. G. Gwinn, P. O'Neill, A. J. Guerrero, D. Bouwmeester, and D. K. Fygenson, "Sequence-Dependent Fluorescence of DNA-Hosted Silver Nanoclusters," vol. 20, ed: WILEY-VCH Verlag, 2008.

Chapter 3

Entangled Two-Photon Absorption

Abstract: We utilize entangled photons to carry out nonlinear optical spectroscopy in organic molecules with an extremely low number of photons. Selectivity of the entangled photon absorption process is also observed and a theoretical model of this process is provided. Through these experiments and theoretical modeling it is found that while some molecules may not have strong classical nonlinear optical properties, due to their excitation pathways, these same excitation pathways may enhance the entangled photon processes. It is found that the opposite is also true. Some materials with weak classical nonlinear optical effects may exhibit strong entangled photon nonlinear optical effects. These results provide the first steps in realizing and demonstrating the criteria for molecular control and rational design of enhanced entangled two-photon absorption.

The bulk of this chapter was originally published as the following document:

"Optically Excited Entangled States in Organic Molecules Illuminate the Dark"

L. Upton, M. Harpham, O. Suzer, M. Richter, S. Mukamel, and T. Goodson, III

The Journal of Physical Chemistry Letters 2013 4 (12), 2046-2052

Modifications to the original document were made solely for adapting the content to this form. References between the original manuscript and supporting information have been unified into a single numbering system.

3.1 Introduction

As stated earlier in Chapter 1, quantum entanglement [1] has surprisingly proven to have implications in numerous physical applications. For example, it is a critical ingredient for the fast transfer of information, as well as the encryption of data.[2] Optically, it is responsible for elusive quantum communication protocols and non-locality representation schemes [3, 4]. Quantum entanglement has also been discussed in such diverse fields as biology to computer system's logic [5-8]. It is found that sometimes the details of quantum mechanics give rise to phenomena which are counterintuitive to our classically driven sense of reason. A number of studies have analyzed the effects of decoherence within quantum systems [9] and the feasibility of generating entanglement schemes for long distance quantum communication [10].

In this chapter, we present results of absorption as a result of quantum entangled two-photon excitation in an organic material. These measurements take advantage of the nearly ten orders of magnitude enhancement observed when entangled (versus classical) two-photon measurements are carried out [11-13]. We demonstrate that when using entangled photons it is possible to carry out two-photon absorption with a small input flux 10^{10} photons/cm^{2}s compared to 10^{18} photons/cm^{2}s due the correlations of the entangled fields. Yet, the effects of these correlations between the entangled photon states on material electronic states have not yet been fully characterized. Not only is the cross-section modified, but also the two-photon processes are no longer quadratic in intensity dependence.

This approach may be implemented in a number of quantum optical sensors and detectors. The measurable enhancement despite lower input flux is useful when one

considers the potential damage biological samples may incur when probed with the high flux fields needed for multi-photon microscopy [14]. We also discuss the entangled two-photon absorption and the electronic state mechanisms that govern the interactions between the entangled photon states and electronic material states. With such mechanisms, it will be possible to predict entanglement sensitive molecules, thus allowing us to design molecules optimized for particular quantum processes and applications. This report offers what could be the first step toward real applications of two-photon molecular control using quantum-entangled fields in in organic materials.

Classical two-photon absorption (TPA) is a third-order nonlinear optical process [15]. As discussed in Chapter 2, TPA is an extremely inefficient process [16], requiring a very high input flux of photons to overcome the small cross-sections. To increase the two-photon probability, high peak intensity pulsed lasers are generally utilized. One can get a sense of the inefficiency of this process by comparing the two-photon absorption cross-section to the one-photon absorption cross-section. While the units of the two processes are different, it is important to note the difference in the order of magnitude between the two processes. Cross-sections for two-photon absorption in most organic chromophores are typically on the order of $1 \times 10^{-48} cm^4 s/photon$. On the other hand, the one-photon cross-section is, in general, on the order of $1 \times 10^{-16}\ cm^2$.

3.2 Entangled Two-Photon Absorption Revisited

In order to describe these nonlinear interactions between light and matter, it is useful to invoke higher order optical coherence theory. As shown in classical TPA can be described with second order correlation functions [17]. It then follows that the rate for classical two-photon processes is quadratic in nature. Unlike single photon absorption

there is a (ϕ^2) dependence on the fields. Using second-order perturbation theory, the classical two-photon absorption cross-section (TPACS) δ_R is given [16] by:

$$\delta_r = \frac{\pi}{2}\omega_1^0\omega_2^0\delta\left(\varepsilon_f - \varepsilon_i - \omega_1^0 - \omega_2^0\right)\times\left|\sum_j\left[\frac{D_j}{\Delta_j^{(1)} - i\kappa_j/2} + \frac{D_j}{\Delta_j^{(2)} - i\kappa_j/2}\right]\right|^2 \quad \textit{Equation } 3.1$$

where ω_1^0 and ω_2^0 are the frequencies of the of the two photons, $\delta\left(\mathcal{E}_f - \mathcal{E}_i - \omega_1^0 - \omega_2^0\right)$ enforces conservation of energy, ε_f and ε_i are the energy eigenvalues of the ground and excited state, respectively, $\mathrm{D_j} = \left\langle \psi_\mathrm{i} \middle| \mathrm{e}\cdot\mu \middle| \psi_\mathrm{j} \right\rangle \left\langle \psi_\mathrm{j} \middle| \mathrm{e}\cdot\mu \middle| \psi_\mathrm{f} \right\rangle$ give the transition dipole matrix elements between the ground and excited states, κ_j are the state linewidths, and $\Delta_j^{(k)} = \varepsilon_j - \varepsilon_i - \omega_k^0$ is the energy mismatch and k=1 or 2 refers to each of the photons involved in the interaction. In organic systems, the size of this cross-section can be manipulated by increasing the conjugation length in the molecule and by utilizing different donor acceptor configurations [18, 19]. It should be noted that two-photon absorption can occur in molecules via a permanent dipole transition or via a virtual state transition [20].

Moving beyond the classical regime of nonlinear optics to study the effects of quantum correlated photons in nonlinear spectroscopy; we see that the quantum effects caused by entangling the excitation source vary the interaction mechanism between the fields and the material system and provide a method of probing the quantum pathways of

these material systems [21]. Entangling the source also provides more flexibility and control of bandwidth and temporal resolution than classical sources [22].

In order to fully describe the interactions between entangled photon pairs and matter it is again useful to consider higher order optical coherence theory. Entangled photons generated by the process of spontaneous parametric down conversion have a high level of spatial and temporal correlation described by fourth order correlation functions [23]. As stated in Chapter 1, because the photons are correlated, the absorption rate has linear intensity dependence instead of the normal quadratic dependence for two-photon absorption, despite it also being a two-photon process. The entangled two-photon cross-section σ_E is given as [24]:

$$\sigma_e = \frac{2\pi}{(\hbar\varepsilon_0 c)^2 A_e T_e}\omega_i \omega_s \delta\left(\varepsilon_f - \varepsilon_i - \omega_i - \omega_s\right) \times \left|\sum_j \left\{ D_{is}^{(j)} \frac{1-\exp[-iT_e\Delta_j^{(i)}]}{\Delta_j^i} + D_{si}^{(j)} \frac{1-\exp[-iT_e\Delta_j^{(s)}]}{\Delta_j^s} \right\}\right|^2 \qquad \textit{Equation } 3.2$$

where $\hbar$ is Plank's constant, ε_0 is vacuum permittivity, c is the speed of light, A_e and T_e are entanglement area and entanglement time, respectively, ω_i and ω_s are the frequencies of the idler and signal photons, $\delta\left(\varepsilon_f - \varepsilon_i - \omega_i - \omega_s\right)$ enforces energy conservation, ε_f and ε_i are the energy eigenvalues of the ground and excited state, respectively, $D_{is}^{(j)} = \left\langle \psi_i \middle| e_i \cdot \mu \middle| \psi_j \right\rangle \left\langle \psi_j \middle| e_s \cdot \mu \middle| \psi_f \right\rangle$ give the transition dipole matrix elements and $\Delta_j^{(k)} = \varepsilon_j - \varepsilon_i - \omega_k$ is the detuning energy where k=i or s refers to the signal and idler photons. The fourth order correlation functions pertaining to the fields are contained

within the spatial and temporal contributions of A_e and T_e. It is also important to note that unlike the classical two-photon absorption cross-section, the entangled cross-section is inversely proportional to A_e and T_e.

Theory states that the ETPA rate is not an exclusive process consisting only of $\sigma_E\phi$, but is accompanied by a non-entangled or random TPA effect [25] involving two noncorrelated photons The entangled two-photon absorption rate, R_e, is derived [26] in the same manner as Equation 3.1 and Equation 3.2 using time-dependent second-order perturbation theory to determine the cross-sections and using correlation functions to determine the flux dependence [17]. The overall ETPA rate with contributions from both entangled and classical two-photon absorption R_e is thus expressed [11, 13, 27] as the sum of the linear ETPA rate and the quadratic, random TPA rate

$$R_E = \sigma_E\phi + \delta_R\phi^2, \qquad Equation\ 3.3$$

where σ_e is the ETPA cross-section Equation 3.2, δ_R is the random TPA cross-section Equation 3.1 and ϕ is the input photon flux density of photon pairs. For small input fluxes, the entangled contribution dominates. However, as the flux increases the random TPA rate takes over.

Using an entangled photon experimental protocol provided in Section 3.3.1, we excited several classes of molecules at 800nm, which is far from their single photon resonance energies. We provide tests to show that the measured absorption rate was not due to excitation from the classical fundamental or the classical SHG. We demonstrate that entangled photons are sensitive to the absorption mechanism of the molecule being probed. Lastly, we present a model that describes the mechanism of absorption of

entangled photons for various material systems. To further test this model, simpler and better studied molecules are chosen and their ETPA cross-sections are compared.

3.3 Experimental Methods

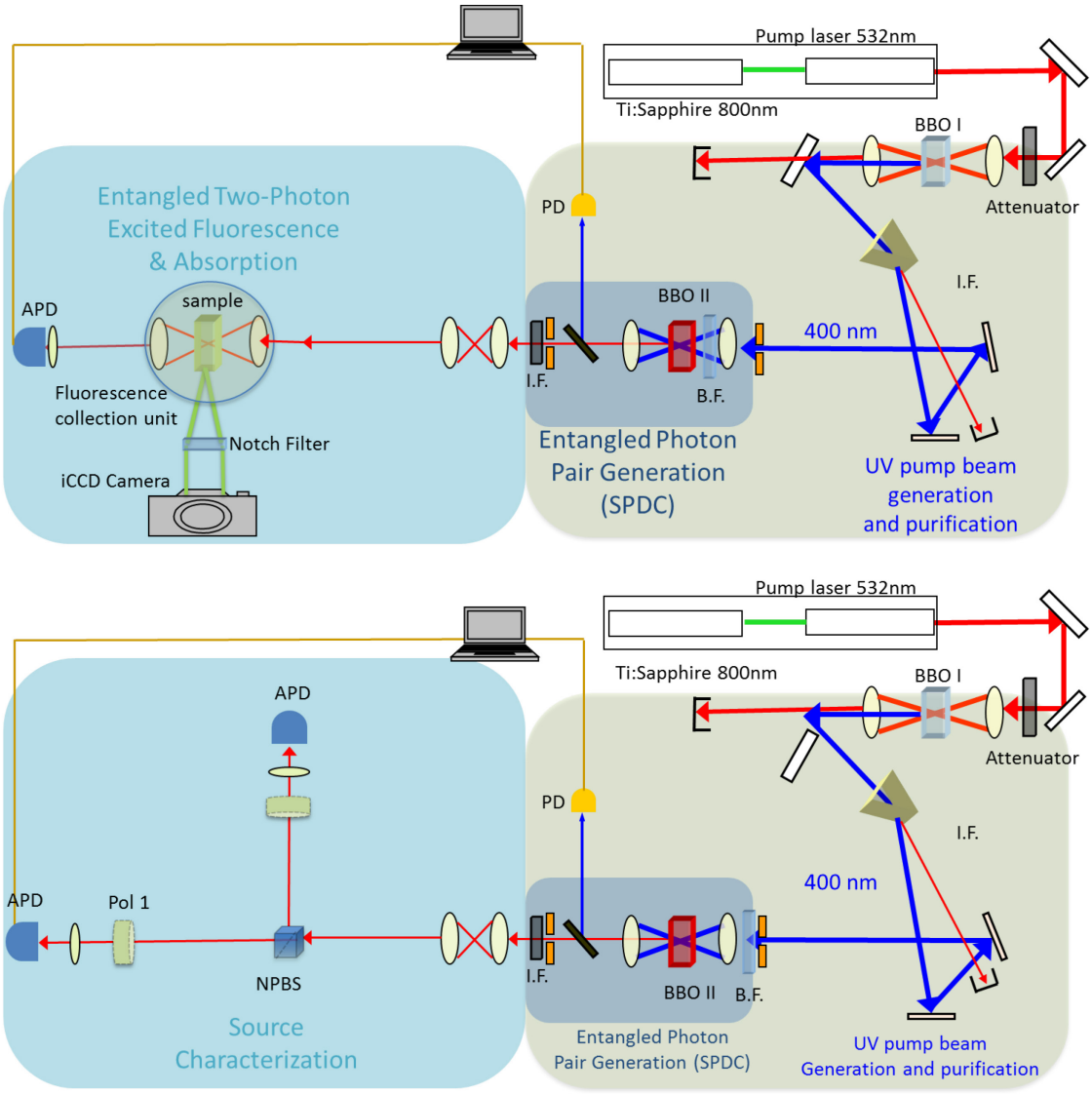

Figure 3.1. The original experimental set-up. Complete re-alignment was needed to carry out visibility and ETPA absorption measurements, as well as, imaging the SPDC profile.

3.3.1 Entangled Two-Photon Absorption Experimental Set-Up

To generate the entangled photons, we use a mode-locked Ti:Sapphire laser with a pulse width of 100fs, 80MHz repetition rate and 12nm bandwidth. The fundamental passes through a neutral density filter, which is used to attenuate the fields for the intensity dependent measurements. The fundamental is focused on a 1 mm thick barium borate (BBOI) crystal of type I configuration to generate second-harmonic light. After passing through the second lens of the telescope, the collimated beam which is a mixture of the fundamental the second harmonic is directed to a dichroic mirror that reflects the second harmonic and transmits the fundamental. Since the dichroic mirror transmits the fundamental, the fundamental is then passed to a beam dump. The dichroic mirror directs the second harmonic and any residual not transmitted to the beam dump to a prism for further purification. After the prism, a beam dump collects the residual fundamental.

The second harmonic is then focused on a 0.5 mm thick barium borate II (BBOII) crystal cut for type-II spontaneous parametric down conversion (SPDC). Adjusting the angle of the BBOII can change the phase-matching conditions of the nearly degenerate signal and idler photons. Another dichroic mirror is used to purify the entangled photon field. It reflects the second harmonic light to a New Focus Inc. Large Area Visible Photoreceiver Model 2031 which is used as a reference photodiode for these experiments. The detector is set at low gain. Three high optical density (OD) filters are placed in front of the reference photodiode to prevent damage to the photoreceiver since the saturation power at low gain is 4 mW. The manufacturer's specifications are included in Appendix A of this dissertation.

The entangled photons centered at 800nm are transmitted. Any residual second harmonic is blocked with a high OD interference filter. After the filter is a telescope used to adjust the SPDC ring size, if necessary. The entangled photons are then focused onto the sample. The sample is held in a custom fluorescence cube. The fluorescence cube was constructed to conducted fluorescence measurements. A Princeton Instruments intensified charge coupled device (ICCD) camera is positioned perpendicular to the fluorescence cube. There is a cutout in the fluorescence cube that allows the fluorescence to be measured by the ICCD camera. The entangled photons are transmitted through the cube and a second lens outside of the cube collimates the beam. The transmitted beam intensity is then measured on a Perkin Elmer SPCM-AQR-13 silicon avalanche photodiode single photon counting module (SPCM). The manufacturer specifications are also included in the appendix at the end of this dissertation. The absorption set-up including the fluorescence cube and the ICCD camera can be removed in order to add a non-polarizing beam splitter, two polarizers and another SPCM to carry out visibility measurements used to characterize entanglement. After the interference filter and the telescope, the entangled photons are transmitted through the non-polarizing beam splitter. The transmitted photons are directed to a Glan-Thompson polarizer and a focusing lens which focus the photons unto the SPCM. This is the same for the reflected photons.

While this set-up was sufficient for the first experimental tests of these interactions, it was necessary to make adjustments to ensure greater functionality, more reproducibility and better characterization of the fields. Although the set-up was useful for absorption measurements, the optical table had to be re-aligned after the last interference filter in order to image the SPDC profile or do visibility measurements. The

set-up was re-configured to be able to do all measurements with less extensive re-alignment procedures. After the telescope an optical flip mount mirror was inserted to direct the entangled photons to the CCD camera, which was placed on a horizontal 1-D track that allows for positioning for SPDC profile imaging and movement for entangled two-photon excited fluorescence experiments, as well. A second optical flip mount mirror was inserted just before the absorption unit to direct the beam to a non-polarizing beam splitter. After the beam splitter, both the reflected and the transmitted beam are directed to polarizers and lens focusing each beam onto the two SPCMs. To carry out absorption measurements the second flip mount mirror is flipped out of the beam path so that the beam is focused onto the sample.

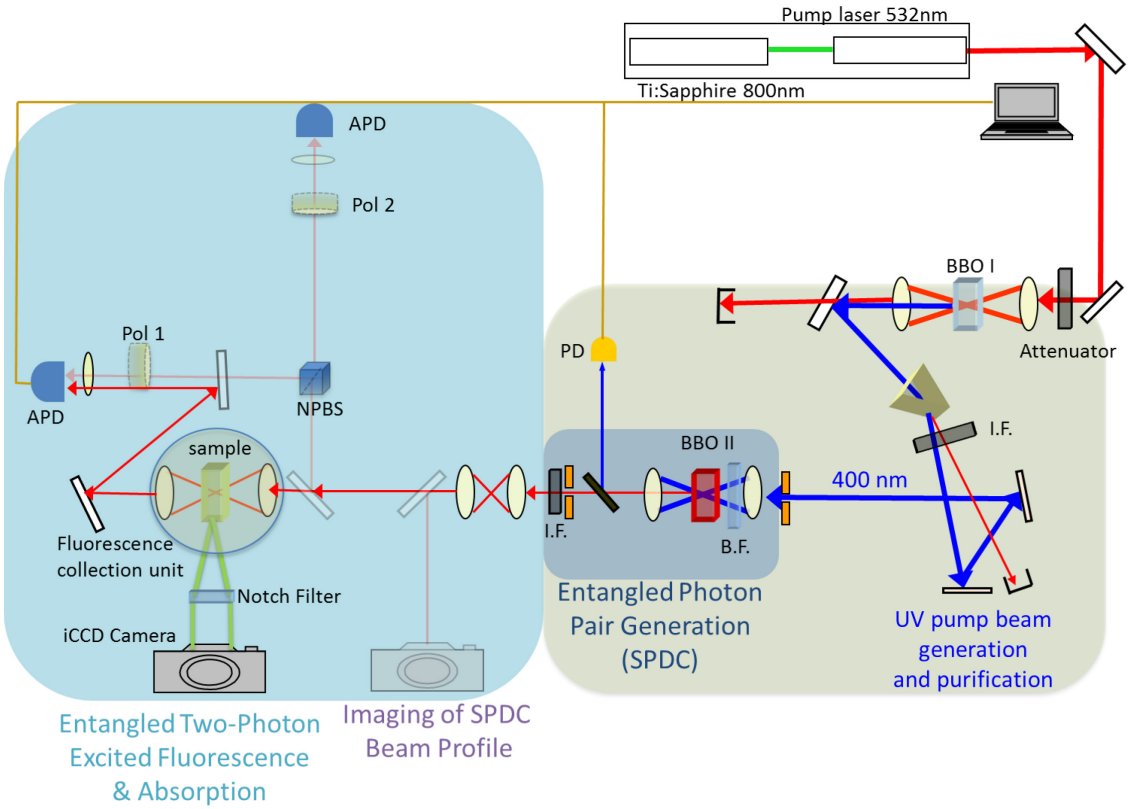

Figure 3.2. Entangled Two-photon Absorption experimental set-up is composed of several nonlinear optical components.

A mirror is added after the sample cell. Another flip mount mirror is added to direct the beam to the SPCM. This mirror is flipped out of the beam path for visibility measurements.

The phase-matching conditions are determined and adjusted by imaging the signal and idler beams with the ICCD camera. The collinear signal and idler beams are then focused onto the sample. The entangled photon flux is measured via a silicon avalanche photodiode single-photon counting modules (Perkin-Elmer SPCM-AQR-13). We conduct two-photon experiments with the use of just 10^7 entangled photons per second, which is virtually impossible with classical photons since the efficiency of two-photon absorption is so low. The classical two-photon laser source generates approximately 10^{24} photons per second. Experiments were carried out both in thin film and solution.

3.3.1.1 Background Measurements

After re-configuring the set-up, it was necessary to do some preliminary tests and checks for background noise in order to decrease background and the possibility of fundamental leaks. Shielding was added around the first BBO to block scatter from the fundamental. After the prism, we inserted a 390 nm center wavelength 40nm bandwidth OD 6 fluorescence filter from Edmund optics to ensure blockage of any of the fundamental into the second harmonic beam path. We also replaced the interference filter after the second BBO for entangled photon generation with a Semrock 800/12 nm BrightLine® single-band bandpass filter with approximately OD 6 blocking at 400nm to prevent SHG leaks.

As stated earlier, the entangled photon flux is measured via a silicon avalanche photodiode single-photon counting modules (Perkin-Elmer SPCM-AQR-13). The focal

spot size of the signal and idler fields onto the detector is ~30um. The photon detection efficiency at 800nm is 60% and 7% at 400nm. The factory estimated dark counts for the SPCM are 250 counts/sec. The experimentally measured dark counts were approximately 300 counts/sec. The results of the spurious background was measured and noted. The laser was blocked with an anodized beam block. Counts generated from this scatter are on the order of 10^4 counts/sec. After the beam block was removed there was still measured scattered. At first this was thought to be thermal lensing. Since high intensities were attenuated ~800mW, tests were completed to ensure that thermal lensing does not occur at any filters in the system, as can be seen in Figure 3.3 and Figure 3.4.

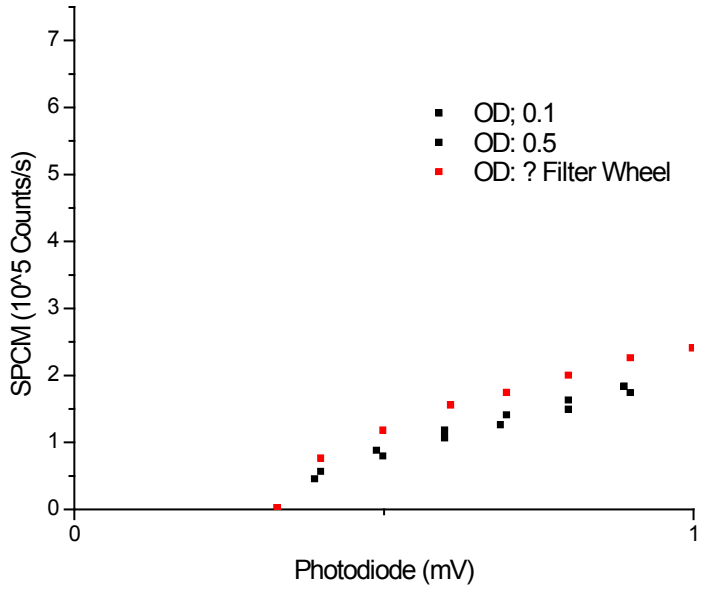

Figure 3.3. The system was tested for thermal lensing. OD 0.1 and 0.5 filters were used. The filter wheel was also used and adjusted to its most opaque setting.

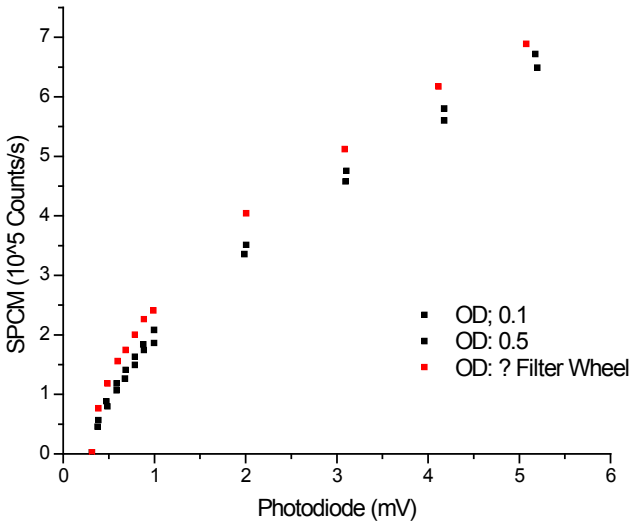

Figure 3.4. The system was tested for thermal lensing. OD 0.1 and 0.5 filters were used. The filter wheel was also used and adjusted to its most opaque setting.

However, thermal lensing did not seem be the case. Scatter showed no SPDC angle dependence, which suggested that it was from the fundamental. The SHG was also detuned such that there was not enough SHG power to pump the SPDC crystal to generate entangled photons. This was done over low voltages in Figure 3.5.

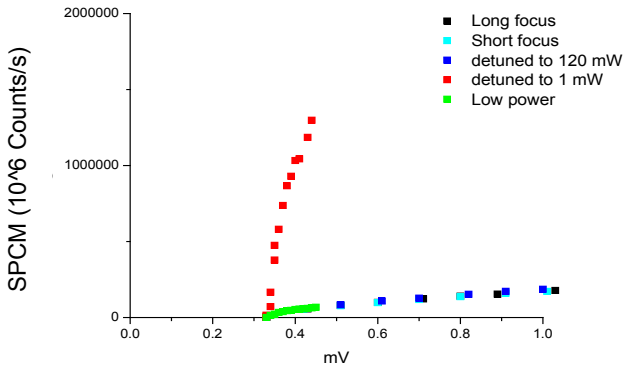

Figure 3.5. The first BBO that generates the SHG was detuned from a max power of 120 mW to 1 mW blue light to determine the amount of 800 nm fundamental light leakage.

When the crystal is detuned to 1 mW there is not enough power to generate entangled photon via the process of spontaneous parametric down conversion. Therefore the majority of the counts on the SPCM are from the fundamental. There was relatively no difference between the results for the short and long focus comparisons or the low power investigation.

Figure 3.6 gives the detuned SHG such that there was not enough SHG power to pump the SPDC crystal to generate entangled photons over the experimental reference photodiode voltage range. This also suggested a leak of the fundamental.

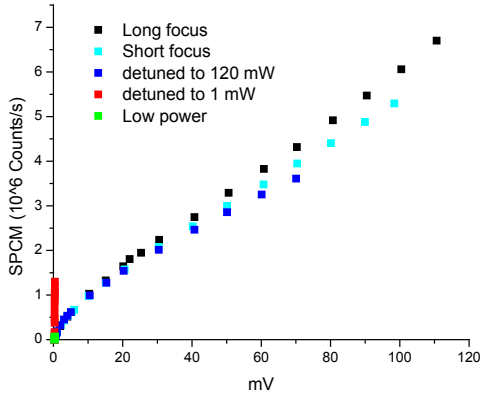

Figure 3.6. The first BBO that generates the SHG was detuned from a max power of 120 mW to 1 mW blue light to determine the amount of 800 nm fundamental light leakage. These measurements were extended out to longer wavelengths. The results for 1 mW do not seem to have a dependence on voltage because there is not enough blue power to focus onto the reference photodiode.

400 nm and 800 nm filters were used to determine the source of the scatter. When an 800nm filter is placed in front of the interference filter the counts are cut almost in half. When the filter is placed directly in front of the detector, the scatter is cut down to 5 x 10^3 counts/sec. The SHG crystal was enclosed with a cardboard shield. That cut the scatter counts in half from 2.2 x 10^4 to 10^4 counts/sec. The SHG generation portion of

the experimental set-up was then enclosed. With this enclosure, and the counts dropped to 2 $x10^3$ counts/sec. With additional shielding the counts were cut to 8.9 $x10^2$ counts/sec. With the addition of the filter the counts were cut further on order with the experimental dark counts with the laser shutter closed. After these adjustments the absorption rate at 1 x 10^7 photons/s for ZnTPP was reduced to 4.24 x 10^5 photons/s versus 1.0 x 10^6 photons/s before the adjustments.

Other tests were run to ensure the linearity of the detectors at low input fluxes. In quantum optics the idea of measurement plays key role in experiments. As such, the devices that carry out these measurements are quite important. Since the crux of the experiment rests on the detection of linear intensity dependence at low powers it is crucial that the detectors are linear in this region. The key instruments in this experiment are the reference photodiode and the single photon count module. The spec sheets for both instruments are included in the Appendix. Efficiencies and linearity of the detectors are important.

3.3.1.2 Instrument Correction Factors

To determine the input flux rate for the absorption measurements a correction factor is applied to the collected data from the single photon counting module. The correction takes into account the APD dead time and is calculated using the method outlined in the Perkin Elmer datasheet. The total collected counts are then plotted as a function of the input flux measured by the single photon counting module. The Single Photon Counting Module has an active area of 180 μm. The linear correction factor for the SPCM is given in the spec sheet and given by:

$$Correction\ Factor = \frac{1}{1 - (t_d \times C_R)} \qquad Equation\ 3.4$$

Where t_d is the deadtime and C_R is the countrate. The deadtime was chosen to be 55 nanoseconds. The deadtime can be adjusted over a range of 20 ns from 40 to 60 ns. The results of the deadtime dependence on ETPA absorption graphs are given in Figure 3.7, Figure 3.8 and Figure 3.9. Further information regarding the SPCM can be found in the Appendices.

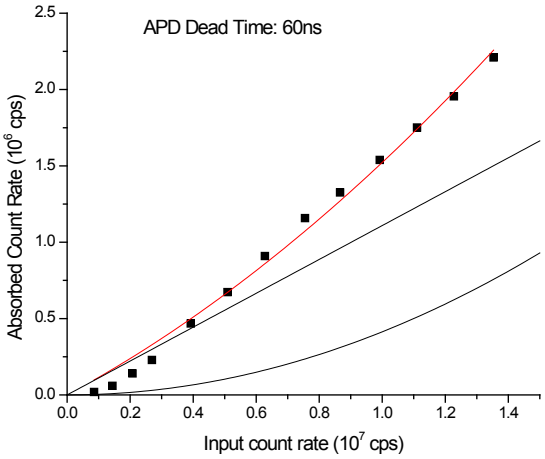

Figure 3.7 The entangled two-photon absorption cross-section plotted with an APD dead time of 60ns. This was calculated with the dead time equation given on the Perkin Elmer SPCM-AQRH.

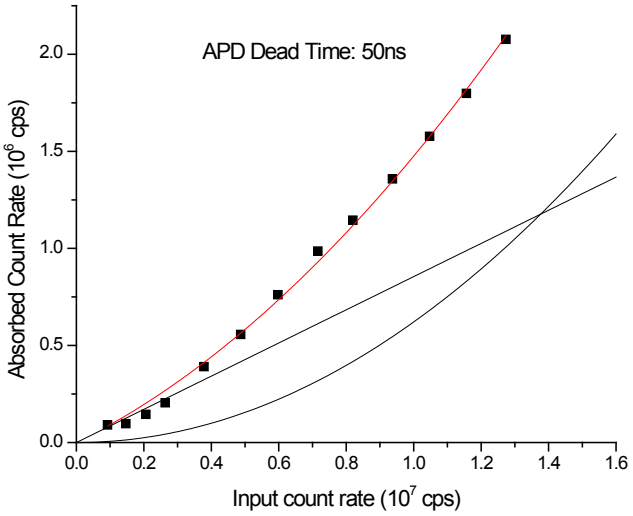

Figure 3.8 The entangled two-photon absorption cross-section plotted with an APD dead time of 50ns.

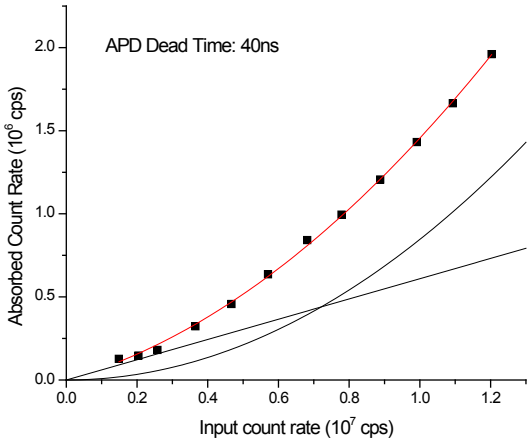

Figure 3.9 The entangled two-photon absorption cross-section plotted with an APD dead time of 40ns.

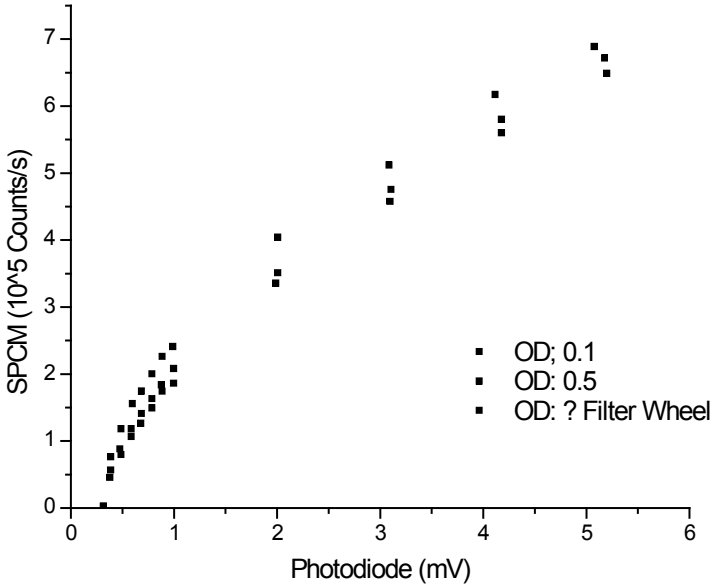

Figure 3.10. The linearity of the single photon counting module is tested at low powers.

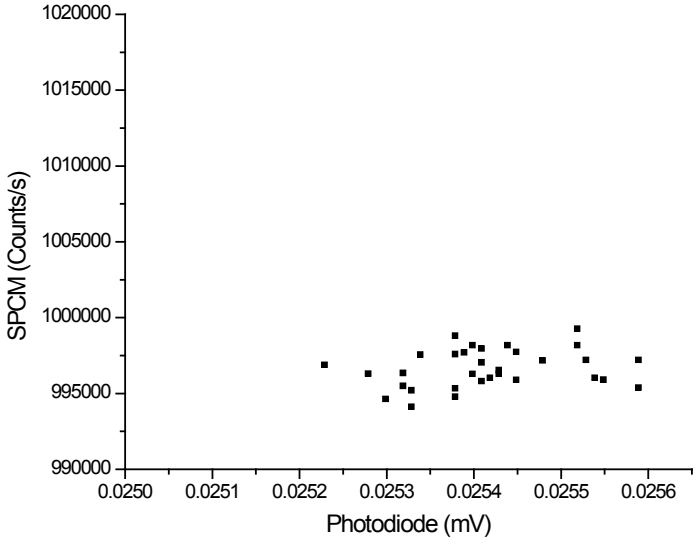

Figure 3.11. The drift of the single photon counting module is measured as a function of time. There seems to be no charge building up on the detector.

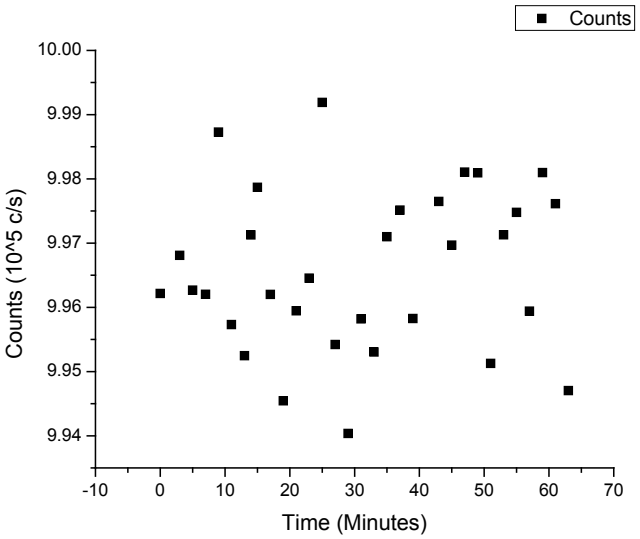

Figure 3.12. The drift of the single photon counting module is measured as a function of time at low input fluxes. There seems to be no charge building up on the detector

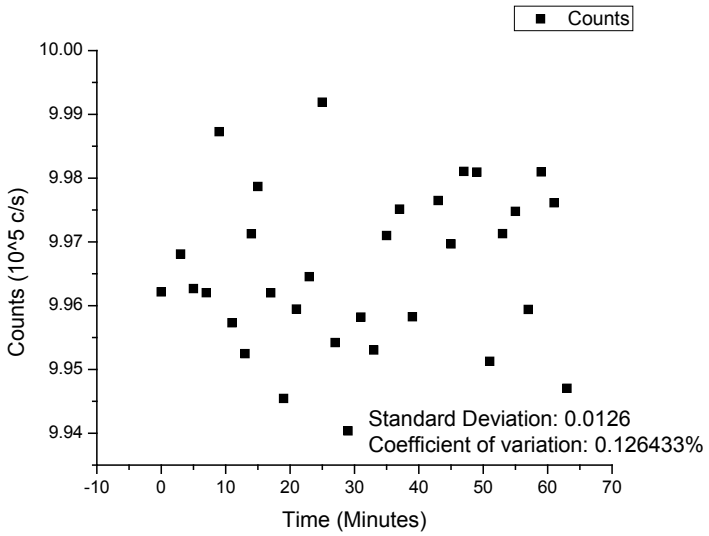

Figure 3.13. The standard deviation of the single photon counting module was measured to be 0.0126.

The reference photodiode diode used to measure the SHG power is a New Focus Large-Area visible Photoreceiver Model 2031. The detector has an 8mm diameter. The gain is set to low. The detector was tested for linearity, thermal lensing and also checked to ensure that there is no charge build up on the photodiode. The reference photodiode was tested for linearity in the range from 0 to 1 mW. This is plotted in Figure 3.14.

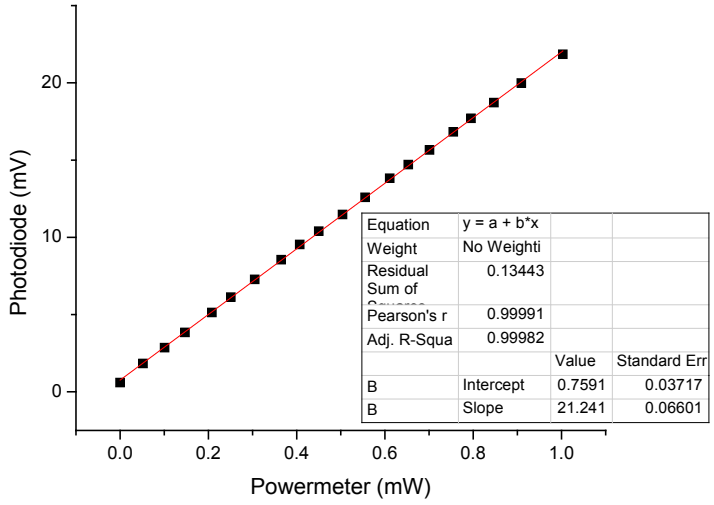

Figure 3.14. The linearity of the photodiode is tested at low powers.

Tests were carried out to test whether there was charge built up on the photodiode. The measurement was carried out over an hour which is typically longer than ETPA experiments. The data is given in Figure 3.16. The standard deviation of the fluctuations of the photodiode was measured and shown in Figure 3.16. The standard deviation is 0.08943 and the coefficient of variation is 0.352%.

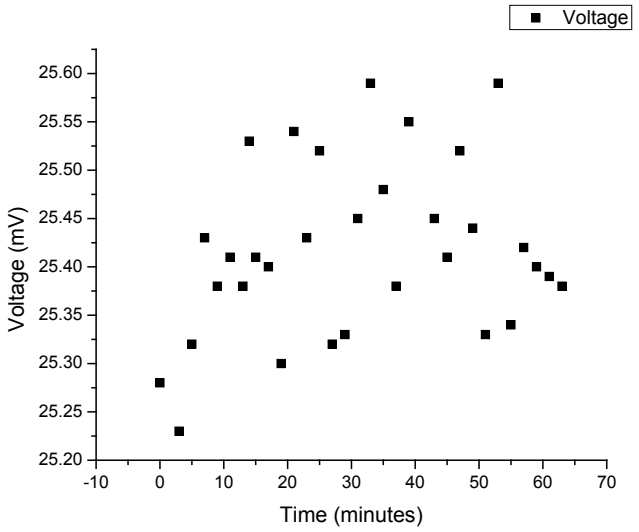

Figure 3.15. The drift of the reference photodiode is measured as a function of time at low input fluxes. There seems to be no charge building up on the detector.

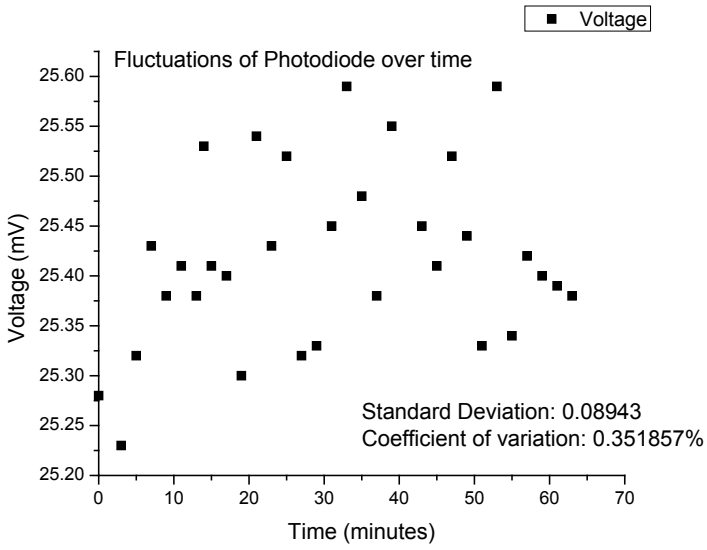

Figure 3.16. The standard deviation of the reference photodiode module was measured to be 0.08943.

3.3.1.3 Spontaneous Parametric Down Conversion

There are several methods to generate entangled photons. However, pulsed spontaneous parametric down conversion is a process by which we generate the entangled photons for these experiments. The SPDC process has a low conversion efficiency, usually on the order of 10^{-12} mm^{-1} (7×10^{-8} mm^{-1} sr^{-1}) of crystal length [28], which is comparable to experimental efficiencies 3×10^{-8} mm^{-1} sr^{-1} [29]. The focus of this section will be on pulsed type-II optical parametric conversion since the entangled photons generated for these experiments are generated via this method. The photon pairs created via type-II SPDC are orthogonally polarized. Whereas, photons from pairs created via type-I SPDC have the same polarization [30]. It is generally easier to experimentally prepare Bell states using type-II SPDC than it is for type-I SPDC [31]. However, pulsed type-II SPDC does provide its own challenges since distinguishability between the two-photon wave functions arises in the space-time contribution of the wave function.

This section will cover energy-time entanglement and the polarization entanglement which will prove important in future experiments and theoretical analysis [32]. The polarization entangled SPDC wavefunction is given by [30]:

$$|\psi\rangle = \left(|H_1, V_2\rangle + e^{i\alpha}|V_1, H_2\rangle\right)/\sqrt{2} \qquad Equation\ 3.5$$

While the time delay between the signal and idler are given by:

$$\delta T = L(1/u_o - 1/u_e) \qquad Equation\ 3.6$$

which is a result of the velocity differences that arise from the nonlinearity of the crystal, the importance of which will be discussed later. This term suggests that the signal and

the idler are created within some entanglement time. This time delay denotes a fourth order coherence function [32-34]. Using this we can calculate the entanglement time, which is just:

$$T_e = T_1 - T_2 = \frac{l}{2}\left(\frac{1}{u_1} - \frac{1}{u_2}\right), \qquad Equation\ 3.7$$

where T_1 and T_2 are the mean transit times of each of the photons. Using birefringence and the 0.5mm thickness of the BBO, the max temporal difference is approximated to be 200fs [32].

There are several methods to measure these time delays and the interference that arises from these delays. The simplest two-photon correlation experiment involves the orthogonally polarized signal and idler directed through a polarizing beam splitter to two separate detectors [35, 36]. A delay in either the signal or the idler can be created by implementing birefringent material before the beam splitter [35]. The coincidences can then be measured as a function of this delay.

However, one can utilize interferometers to carry out these experiments, as well. Interferometers provide one method of controlling the time delay between the signal and the idler. A collinear interferometer nonpolarizing beam splitter directs the signal/idler photons to two detectors each with an analyzer placed in front of it. Experiments measuring coincidence counts as a function of the time delay between the signal and idler have been carried out with Michelson and Mach Zehnder interferometers [35, 37]. Unfortunately, a spatially separated Mach Zehnder interferometer is often difficult to manipulate [31]. Because of this issue, Sergienko et al developed a double unbalanced polarization interferometer. This setup includes a polarization insensitive 50/50

beamsplitter and the first beam path that leads to a variable polarization delay line, an analyzer and the first detector [31]. The second beam path includes an analyzer and a second detector. Sagnac interferometers have been used, as well, to measure pulsed entangled photon interferences. However the type-II SPDC entangled photons studied using this Sagnac interferometer setup were generated in the interferometer after being created by type-I SPDC [38].

As stated earlier, the manipulation of the time delay can also be achieved with the use of a birefrigent material before a set of coincidence detectors. Experimentally, a third generation porphyrin acted as coincidence detector and measurements were carried out by varying the entanglement time with quartz plates [13]. With the use of plates the entanglement time was varied over 200fs. Each 1mm thick plate creates a 30fs optical delay. The time between the signal and the idler was varied 1fs, 150fs and 200fs. Over this range of entanglement times the entangled two-photon absorption cross-section varied an order of magnitude approximately [13].

More experiments should be carried out to not only measure the two-photon interference, but to also more clearly map out entanglement induced transparency in molecules due to the cross-sectional dependence on entanglement time. It should also be noted that one should be careful in using pumped type-II SPDC fields due to the spectral properties of the fields that lead to distinguishability [34, 36, 39]

3.3.1.4 Derivation of Type II SPDC Process

Now that issues with background have been dealt with and are sufficiently low for this experiment, we begin discussion of the actual entangled two-photon fields. For this entangled two-photon absorption experiment, Type-II spontaneous parametric down

conversion was chosen because of the relatively high conversion efficiency compared to other entangled photon pair sources [39]. To better understand how the fields will interact with the molecules studied it is imperative to have some understanding of SPDC. Following the method prescribed by [32], begins with the Hamiltonian for an optical parametric process in a Type-II crystal:

$$H_1 = \varepsilon_0 \int_V d^3r\, \chi E_p^{(+)} E_0^{(-)} E_e^{(-)} + H.c. \qquad Equation\ 3.8$$

where V is the volume of illuminated crystal by E_p, the pump field, . The output fields are given by:

$$E_j^{(+)} = \sum_k E_{j\boldsymbol{k}} a_{j\boldsymbol{k}} e^{i(\boldsymbol{k}\cdot\boldsymbol{r}-\omega_{j\boldsymbol{k}}t)} \qquad Equation\ 3.9$$

the amplitude E_{jk} is

$$E_{j\boldsymbol{k}} = i\left(\frac{\hbar\omega_{j\boldsymbol{k}}}{2\mathcal{E}_0 n_{j\boldsymbol{k}}^2 V_Q}\right)^2 \qquad Equation\ 3.10$$

The commutation relation relates the raising and lowering operator

$$\left[a_{j\boldsymbol{k}}, {a_{m\boldsymbol{q}}}^{\dagger}\right] = \delta_{j\boldsymbol{m}}\delta_{k\boldsymbol{q}} \qquad Equation\ 3.11$$

The pump field is given by

$$E_p^{(+)} = E_0 e^{i(k_p z-\omega_p t)} \qquad Equation\ 3.12$$

$$|\Psi\rangle = |0\rangle + \sum_{kk'} F_{kk'} a_{xk}^{\dagger} a_{yk}^{\dagger} |0\rangle \qquad Equation\ 3.13$$

The average coincidence-counting rate is given by:

$$R_c = \lim_{T\to\infty} \frac{1}{T} \int_0^T dT_1 \int_0^T dT_2 \left\langle \Psi \middle| E_1^{(-)} E_2^{(-)} E_2^{(+)} E_1^{(+)} \middle| \Psi \right\rangle \qquad Equation\ 3.14$$

$$\times S(T_1 - T_2)$$

$$\left\langle \Psi \middle| E_1^{(-)} E_2^{(-)} E_2^{(+)} E_1^{(+)} \middle| \Psi \right\rangle$$

$$= \left| \left\langle 0 \middle| E_2^{(+)} E_1^{(+)} \middle| \Psi \right\rangle \right|^2$$

$$= \left| A(t_1, t_2) \right|^2$$

where $A(t_1, t_2)$ is the two-photon amplitude.

$$A(t_1, t_2) = v(t_1 + t_2) u(t_1 - t_2) \qquad Equation\ 3.15$$

$$u(t) = e^{-i\omega_d \left(\frac{t}{2}\right)} \Pi(t) \qquad Equation\ 3.16$$

$$v(t) = v_0 e^{-i\omega_p \left(\frac{t}{2}\right)} \qquad Equation\ 3.17$$

where $\Pi(t)$ is a rectangular function related to the photon travel time in the crystal. It is this time-energy entanglement that gives rise to the non-monotonic behavior of the ETPA cross-section and the ability to do virtual state spectroscopy. It is an important parameter to study in the future to see how its effects affect ETPA and if ETPA can be controlled. Next, we discuss characterization methods of these fields.

3.3.2 Characterization of the Fields

3.3.2.1 Number of photons per pulse

Entangled photons generated by continuous wave and pulsed sources differ significantly. With the use of pulsed sources, linear dispersion arises due to the various frequencies and the different group velocities [40]. This reduces visibilities. One of the more widely used techniques to remedy this situation is spectral filters. However, these filters do reduce the flux of entangled photons per pulse.

As stated earlier, the experiments were carried out with a Ti:Sapphire laser with a pulse width of 100fs, 80MHz repetition rate and 12nm bandwidth. The pulse energy is given by Equation 3.18.

$$pulse\ energy = \frac{P_{avg}}{Hz} \qquad Equation\ 3.18$$

The average power of the system is 50 mW. Although, ETPA experiments the power is varied from zero mW with the beam blocked to ~105 mW. Using the average power of the pump SHG beam and the repetition rate, the pulse energy is calculated.

$$pulse\ energy = \frac{50\ mW}{80\ Hz} \qquad Equation\ 3.19$$

$$= 6.25 \times 10^{-10} J$$

Once the pulse energy is calculated, we used the fact that the pump beam for SPDC is 400 nm. This is used to calculate the number of photons per pulse.

$$\frac{6.25 \times 10^{-10} J/pulse}{5 \times 10^{-19} J/photon} = 1.26 \times 10^{9}\ photons/pulse \qquad Equation\ 3.20$$

The efficiency based on pulsed sources, which is 0.86×10^{-9} [41] is used. Using this efficiency, we approximate that there is approximately one entangled photon pair per pulse. Experimentally, our singles count rate is 1 x 10^7 photons/s while the coincidence count rate is on the order of 1 x 10^5 photons/s.

3.3.2.2 Visibility Measurements

One method of measuring the quality of an entangled state is to conduct visibility measurements. If coincidence measurements are carried out when certain quantities are entangled, interference patterns should arise. Visibility measurements are the measurement of these visible interference patterns. The greater the indistinguishability of entangled quantities (photons in this particular case), the higher the visibility percentage is. The quality of the entangled state is determined by the contrast between the max coincidence counts and minimum counts. The equation for visibility is given in Equation 3.21. This can be carried out with two detectors and two polarizers. The entangled source is directed to a non-polarizing beam splitter. Each beam after the polarizer is directed to a polarizer in front of a detector where the coincidence counts are measured as a function of polarization angle. For Type-II SPDC, the max visibility should occur when the polarizers are orthogonally polarized. Visibility measurements can be carried out for different phase-matching conditions of the system and are given in Figure 3.17 and Figure 3.18.

$$V = \frac{N_{\max} - N_{\min}}{N_{\max} + N_{\min}} \qquad Equation\ 3.21$$

The noncollinear phase-matching condition has a visibility of 82.64%. The collinear caser has a measured visibility of 77%. While these polarization visibility

measurements do tell us something about the quality of the polarization entanglement, an interesting and relevant measure would be the visibility measurements as a function of the entanglement time [34, 39]. With the use of wave retarders one can measure the coincidence as the entanglement time is increased and decreased.

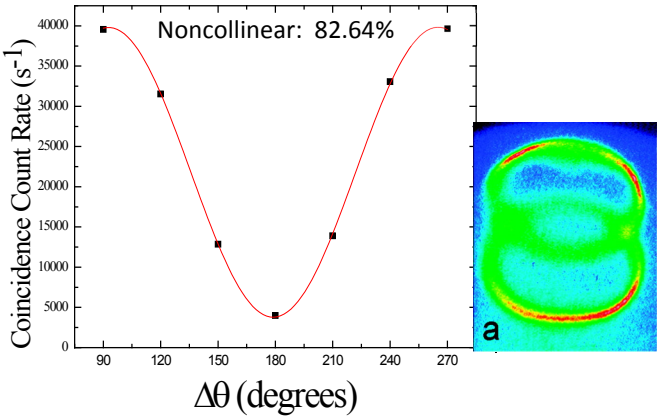

Figure 3.17. The visibility measurements as a function of Δθ for non-collinear phase matching.

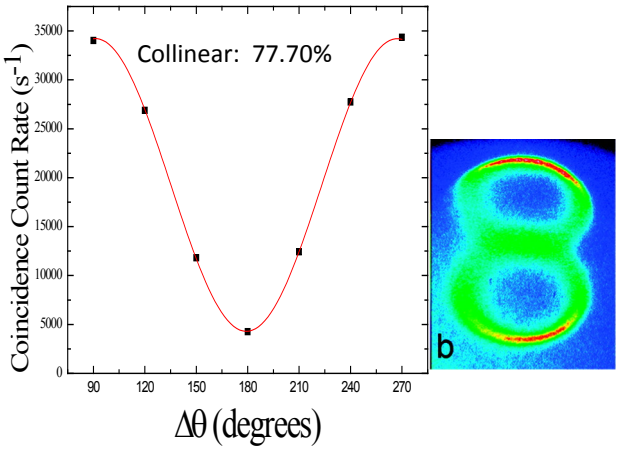

Figure 3.18. The visibility measurements as a function of Δθ for collinear phase matching.

3.4 Materials

All of the materials were chosen for this study was chosen because of their classical two-photon properties and relatively large classical two-photon cross-sections. Compounds **A** is a nitrogen centered tolane dendrimer [42]. Compound **B** is a commercially available Zinc Tetraphenyl Porphin [18]. Compounds **C** and **D** are both thiophene dendrimers [43]. The steady state specs are given [44], for compounds **E** and **F** which are branched donor acceptor chromophores. Compound **G** is commercially available. Molecules **A-D** (Figure 3.19) were used in our absorption and fluorescence studies because of their ability to absorb entangled photons [11] and their relatively high fluorescent quantum yields. Steady state data is provided.

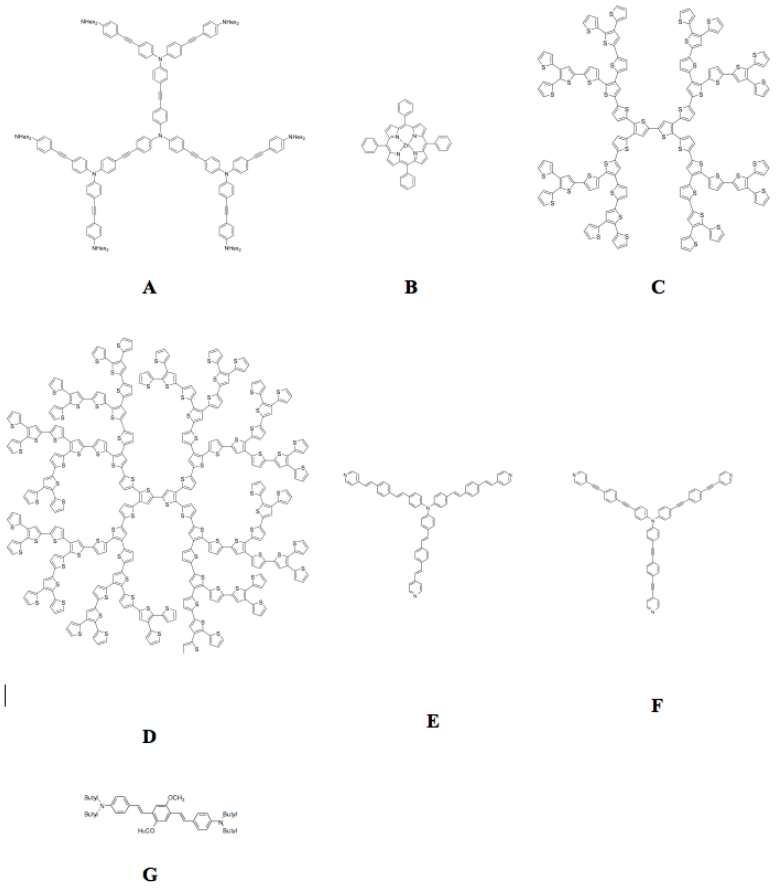

Figure 3.19. Structures and labeling scheme for compounds studied in this chapter.

3.5 Results

From our entangled photon absorption measurements an enhanced cross-section were obtained for several molecules and this result is shown in Figure 3.20. The data for the absorbed photon rate was found to follow closely to that of predicted by Equation 3.3. Also, experiments of entangled photon absorption were carried out for molecular systems depicted in Figure 1 **A-D**. The entangled photon absorption process found in these systems also suggests that a non-classical enhancement effect is operative.

Interestingly, it is found that entangled photon absorption cross-section does not scale with material in the same manner as the classical TPA cross section.

3.5.1 Calculating the ETPA Cross-section

The ETPA rate is measured using transmission measurements. Unlike classical TPA, the entangled two-photon absorption rate associated with the linear intensity does not depend on the area of the pump [25]. Much like classical linear absorption it only depends on the path length of the sample holder. As such, the linear absorption rate is given by:

$$\frac{N_{out} - N_{in}}{N_{in}} = 1 - e^{-\sigma lc} \qquad Equation\ 3.22$$

Where N_{out} is the photon count rate through solvent containing sample, N_{in} is the photon count rate through solvent alone, σ is the entangled two-photon absorption cross-section, l is the path length and c is the concentration of the sample solution. This can be approximated to:

$$\frac{N_{out} - N_{in}}{N_{in}} \approx \sigma lc \qquad Equation\ 3.23$$

Where $\frac{N_{out}-N_{in}}{N_{in}}$ is given by the slope of the linear contribution in ETPA. The slope is calculated by fitting the data to $A\phi + B\phi^2$.

$$0.17 \approx \sigma lc \approx \sigma \cdot 1\ cm \cdot \frac{6 \cdot 10^{-6} M}{L} \qquad Equation\ 3.24$$

The cross-section is then given by: $\sigma \approx \frac{0.17}{6 \cdot 10^{-6}} \approx 4.7 \times 10^{-17} cm^2/molecule$

3.5.2 ETPA Absorption Mechanism

As one can see in Table 1, for example molecule **B**, which has a much smaller classical two-photon absorption cross-section than molecules **A** or **C**, has a entangled two-photon absorption cross-section which is very similar to both **A** and **C**. In general, as depicted by theory described above, the electronic levels responsible for the classical two-photon process are well understood. However, this finding suggests a possible differing absorption mechanism for the entangled photon two-photon process in organic materials.

Another striking contrast to this effect was that for molecules **E-G**, no entangled photon absorption was obtained in our experiments. This result is obtained despite their large classical TPA cross-sections. These materials undergo TPA through a direct transition, based on the large change in permanent dipole moment between ground and excited states. This mechanism does not require that intermediate states be close to resonance with the photons. Experiments with molecules **E-G** were carried out in solution at low concentration, very high concentrations and even in thin films. In each case, no entangled photon absorption could be found in these systems. This result turned out to be very intriguing and completely unexpected.

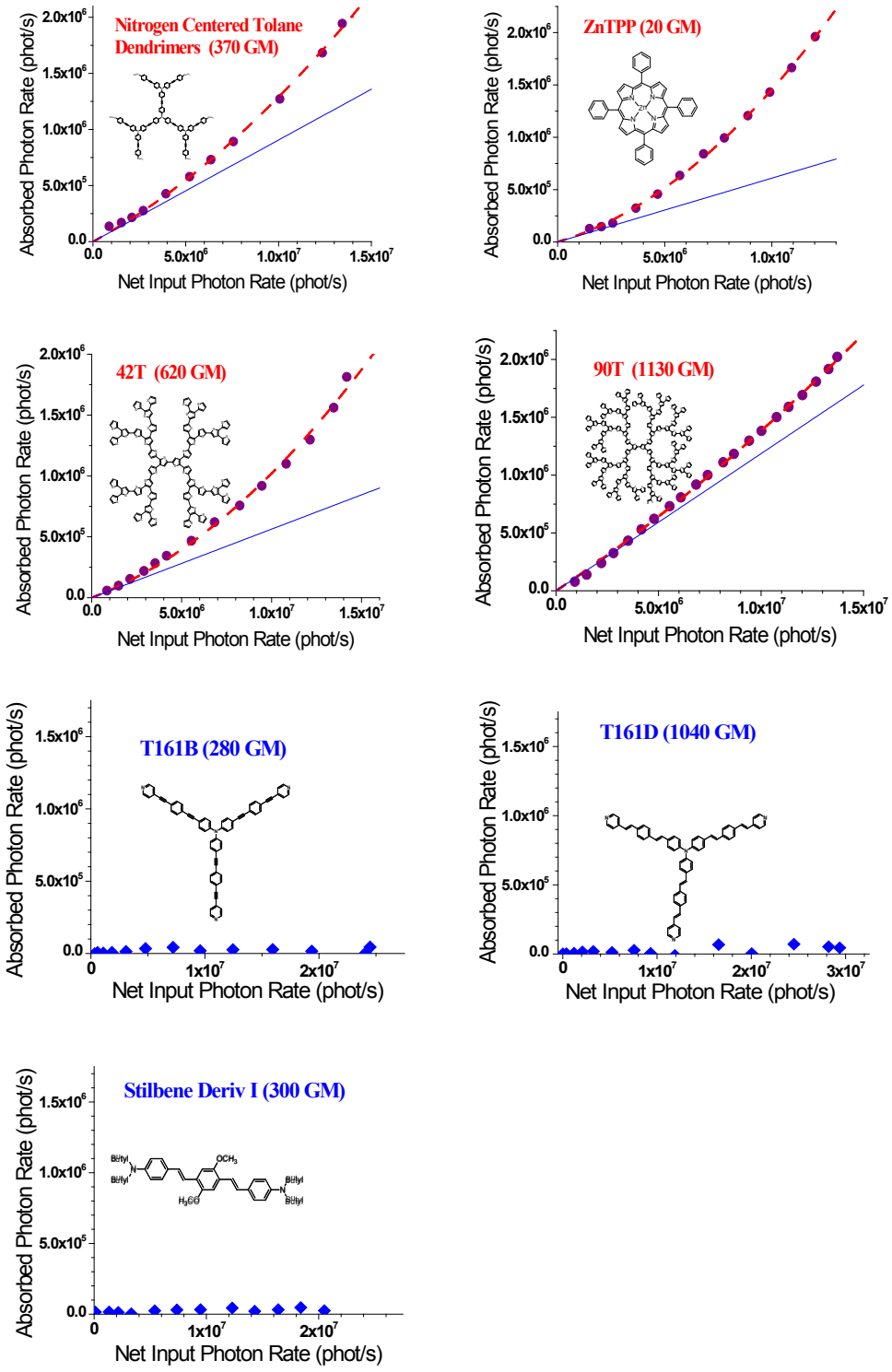

Figure 3.20. The entangled two-photon absorption (ETPA) rate for solutions of a) Nitrogen-Centered Tolane Dendrimer, b) Zinc Tetraphenyl Porphyrin, c) 42-unit thiophene macrocycle, d) 90-unit thiophene macrocycle, e) T161B, g) T161D plotted against input photon rate. For the materials showing ETPA, the linear fit of the initial points of absorbed photon rate is shown with a solid blue line to demonstrate a non-zero

derivative at zero i.e. the presence of linear component, while the best fit to the ETPA absorption rate, $R_E = \sigma_E \phi + \delta_R \phi^2$, is shown with a dashed red line. Numbers in parentheses correspond to classical TPA cross-sections using an 800 nm excitation.

Material	TPA cross-section[a] δ_R (GM)	ETPA cross-section σ_E (10^{-17} cm^2)
A.) 1st Generation dendrimer	370	2.33
B.) Tetraphenylporphine, Zinc	20	2.37
C.) **42T** thiophene dendrimer	620	1.27
D.) **90T** thiophene dendrimer	1130	2.08
E.) T161B	280	No ETPA
F.) T161D	1040	No ETPA
G.) Stilbene derivative I	300	No ETPA

[a]TPA cross-section reported for an 800 nm excitation from a classical source, 1 GM = 10^{-50} cm^2 photon^{-1} s^{-1} molecule^{-1}

Table 3.1. Two-photon absorption cross-sections and Entangled two-photon cross-sections.

A number of reproducible experiments were performed on these materials to check the validity that in some cases, a material could have a large classical nonlinear response and the same material show no entangled nonlinear response. And later we found the opposite to be true in some cases as well. That depending on the electronic states accessible, an organic material with a relatively small classical two-photon cross-section may have a large entangled photon cross-section. For example, ZnTPP (molecule **B**), is a molecule with a smaller classical TPA cross-section, yet it exhibits a strong ETPA cross-section. These results offer an opportunity for scientists and engineers to

tune the quantum entangled nonlinear process. But in order to do so, one must provide an understanding of the entangled ETPA process.

To interpret why some materials with a large classical two-photon absorption cross-section (TPACS) do not appear to absorb entangled photons, the origin of the TPACS is explored. For a non-centro-symmetric molecule, one can consider a three-level system involving ground state *g*, intermediate state *j* and final state *f*. As stated earlier, the TPACS δ_R is given [16] by Equation 3.1. TPA typically occurs via [20, 45] one of two pathways, a virtual state pathway or a permanent dipole pathway, depending on the material, with the TPA rate increasing quadratically with photon flux [16] regardless of the mechanism. However, one cannot directly infer which pathway is utilized from first glance when using Equation 3.2. In order to directly compare absorption mechanisms for both TPA and ETPA, we now modify Equation 3.1 and Equation 3.2 in order to include and distinguish both pathways.

The classical two-photon absorption cross-section δ_R can be rewritten [20] as:

$$\delta_R = \frac{B}{\hbar^2 \varepsilon_0^2}\omega_0^2 \delta(\varepsilon_f - \varepsilon_g - 2\omega_0)\left|\frac{1}{(\omega_0 + \varepsilon_g - \varepsilon_e) - i\kappa_e/2}\mu_{fe}\cdot e\mu_{eg}\cdot e + \frac{1}{\omega_0 - i\kappa_g/2}\mu_{fg}\cdot e\mu_{gg}\cdot e + \frac{1}{-\omega_0 - i\kappa_f/2}\mu_{ff}\cdot e\mu_{fg}\cdot e\right|^2 \quad \textit{Equation } 3.25$$

assuming only photons of the same polarization in classical case. The first term in Equation 3.25 describes TPA through an intermediate level (A), whereas the second and third term describes a process involving permanent dipoles (B). In the classical case these two terms can be simplified to one contribution proportional to permanent dipole difference $\Delta\mu_{fg} = \mu_{ff} - \mu_{gg}$, which gives Equation 3.1.

Two potential pathways for TPA are observed in the two terms of Equation 3.25 and illustrated in Fig. 3. The transition dipole pathway (A), given by the first term involves an intermediate state (close to resonance with the photon). The transition dipole moments μ_{fe} and μ_{eg}, as well as the detuning between the laser frequency and the intermediate state, are known to play an important role in this TPA mechanism. Materials with moderate donor acceptor character, and without charge-transfer character, are described [46] as absorbing through pathway (A). In the permanent dipole pathways (B), given by the second and third term in Eq. 4, the intermediate state is off resonance and does not play a role. The ground and excited states are connected directly, and resonance between intermediate states and the laser is not required for TPA. In the case of charge transfer materials, the contribution to the TPACS from the intermediate state terms is overshadowed by the contribution from the difference of permanent dipole moments of the ground and the excited states. In this case, the second and third terms of Equation 3.25dominate, and the TPACS is explained [20, 45, 47] by pathway (B). This is known to occur when the intermediate states of the material are very far from resonance with the photons.

3.5.2.1 Virtual State Mechanism

Materials **A-D** in which we have observed ETPA were previously described [11, 44, 48] as having a classical two-photon excitation through pathway (A), in which an intermediate state is involved in the transition. Theoretical investigations have indicated [24, 27, 49-51] an enhancement of the ETPA cross-section under conditions of near-resonance between entangled photons and an intermediate state. We have shown previously that a G3 porphyrin dendrimer was capable of strongly absorbing entangled

photons, with ETPA cross-sections measured nearly on the order of the one-photon absorption cross-section at half the wavelength. By varying the entanglement time, T_E, the intermediate state energy was estimated to be 9.85×10^3 cm^{-1}. This intermediate state energy is found to be approximately 4000 cm^{-1} below the ^1B_u Q_x state within the Q-band [48]. This supports the theory advanced by Fei et al. [52] and Kojima and Nguyen [24] that ETPA involves intermediate states.

3.5.2.2 Dipolar Mechanism

Whereas, literature has suggested [18, 42] that molecules **E-G** undergo a two-photon transition by the permanent dipole mechanism, in which the substantial change in permanent dipole moment between ground and excited states allows a direct transition. It is a direct coupling of the intermediate states to the ground and final states. This is in part due to the large detuning energy between the photon and the intermediate state, which reduces its amplitude compared to the dipole pathway. The molecule **G** was shown [18] to have a $1B_u$ band at 20,600 cm^{-1}, which is approximately 8,000 cm^{-1} higher in energy than the entangled photons used in our experiment. From Eq.(2), the combination of a large detuning energy between the entangled photon and the $1B_u$ band of molecule **G** and a weak coupling to the intermediate state is expected to have a negative impact on the ETPA cross-section of this material, which leads to no measurable ETPA with our current source of entangled photons.

While molecules **E** and **F** look symmetric, studies have found that the branches of these molecules interact [53, 54]. This interaction causes a fast depolarization, which leads to an enhanced transition dipole due to localized charge on a single branch [54]. Because of this change in the permanent dipole moment between the ground and excited

state, the dipolar term is non-zero, which may explain why there is no ETPA response in these molecules.

As stated before, the ETPA cross-section is reported to have dependence on the detuning energy between the entangled photon and the intermediate state, as well as, on the intermediate state linewidth, and the transition matrix elements. To account for this dependence in the ETPA cross-section, Equation 3.2 is rewritten in the same manner as Equation 3.25. For a system with ground, intermediate, and excited state wavefunctions $|g\rangle$, $|e\rangle$, and $|f\rangle$, and under a simplified case of a monochromatic pump between signal and idler beam, we derived for σ_E (analog to Fei et al [52]):

$$\sigma_e = \frac{A}{\hbar^2 \varepsilon_0^2 A_e T_e} \omega_0^2 \delta(\varepsilon_f - \varepsilon_g - 2\omega_0) \left| \frac{1 - e^{-i(\omega_0 + \varepsilon_g - \varepsilon_e)T_e - \kappa_e T_e/2}}{(\omega_0 + \varepsilon_g - \varepsilon_e) - i\kappa_e/2} \mu_{fe} \cdot e_i \mu_{eg} \cdot e_s \right. \quad \textit{Equation } 3.26$$
$$\left. + \frac{1 - e^{-i\omega_0 T_e - \kappa_g T_e/2}}{\omega_0 - i\kappa_g/2} \mu_{fg} \cdot e_i \mu_{gg} \cdot e_s + \frac{1 - e^{i\omega_0 T_e - \kappa_f T_e/2}}{-\omega_0 - i\kappa_f/2} \mu_{ff} \cdot e_i \mu_{fg} \cdot e_s \right|^2$$

where A_E and T_E are entanglement area and entanglement time, respectively, ω_0 is the frequency of the signal and idler photons, e_i, e_s are the polarization of signal and idler, ε_g, ε_e and ε_f are the frequency of the ground, intermediate and excited state, respectively, μ_{ij} are the transition dipole matrix elements and κ_j are the state linewidths. A level scheme as depicted in Figure 3.21 was assumed, three pathways contribute to this scheme: ETPA through an intermediate level $|e\rangle$ and ETPA utilizing permanent dipoles for states $|g\rangle$ and $|f\rangle$. The first term in Equation 3.26 describes ETPA through an intermediate level (A), whereas the second and third term describes a process involving permanent dipoles (B). In the entangled case we cannot simplify the two terms to one contribution

proportional to the permanent dipole difference due to the oscillatory terms in this scenario. Our results suggest that molecules **A-D** absorb photons via mechanism (A) as described by the first term in Equation 3.25, whereas **E-G** utilize mechanism (B) or a combination of both mechanisms (A) and (B).

We have shown that molecules **A-D** are capable of strongly absorbing entangled photons, with ETPA cross-sections measured nearly on the order of the one-photon absorption cross-section, using longer excitation wavelengths. It is clear from the data and the cross-sections that are reported in Table 1 that there seems to be a non-classical fluorescence enhancement.

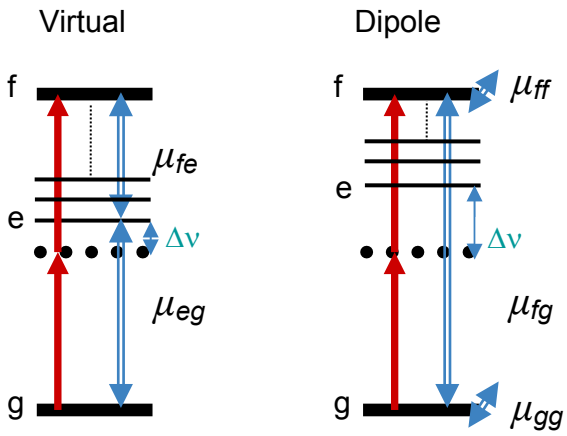

Figure 3.21. Schematic depiction of two-photon absorption pathways. The intermediate state (left) and dipole (right) pathways of classical two-photon absorption are illustrated. Final, intermediate, and ground states are denoted by f, e, and g, respectively. μ is the transition dipole moment is represented as. Photon energies and transition dipole moments are represented by filled and hollow arrows, respectively.

This enhancement is perhaps most clearly demonstrated by the fact that we were able to observe a relatively high fluorescent count rate for such a relatively small input flux. To explain the enhancement of ETPEF and the ETPA cross-sections over TPEF and

the TPA cross-sections, Eq. 4 and 5 are now compared. The material enhancement of ETPA over TPA is visible in the equation with a factor proportional to $\frac{1}{T_e A_e}$.

However, this factor does not explain the material dependent response to entangled photons. The important terms in Eq. 5 are the oscillating terms of the form $1-e^{i\Delta\omega\cdot T_e}$ for each of the contributions. We plot $T_e\sigma_e/\delta_R$ over entanglement time T_e in Fig. 4 for a model system undergoing ETPA via an intermediate level pathway and for a model system with dominant permanent dipole pathway to illustrate this contribution. For case (A) we see an oscillation over entanglement time T_e with a period in the range of several hundred femtoseconds.

Periodic destructive interference and thus entanglement induced transparency, is also seen, as pointed out earlier by Fei et al. [52]. The oscillation frequency is thereby dependent on the detuning between intermediate level and the photons. However, if pathway (B) dominates, the picture is similar except the oscillation pattern is a more complex beating pattern controlled by the two permanent dipoles and the period is much shorter. The oscillation period and the distance between the entanglement induced transparencies is in the range of a few femtoseconds. Therefore, for the permanent dipole case the TPA signal is more likely to be in an area of entanglement induced transparency. In this case, the oscillation frequency is controlled by and equal to the photon energy. The entanglement time of $T_E \approx 100\text{fs}$ used in our experiments may often match values of entanglement induced transparency inside the inhomogeneous distribution of molecules transition frequencies for all materials dominated by pathway (B) because the values of entangled induced transparency are very dense.

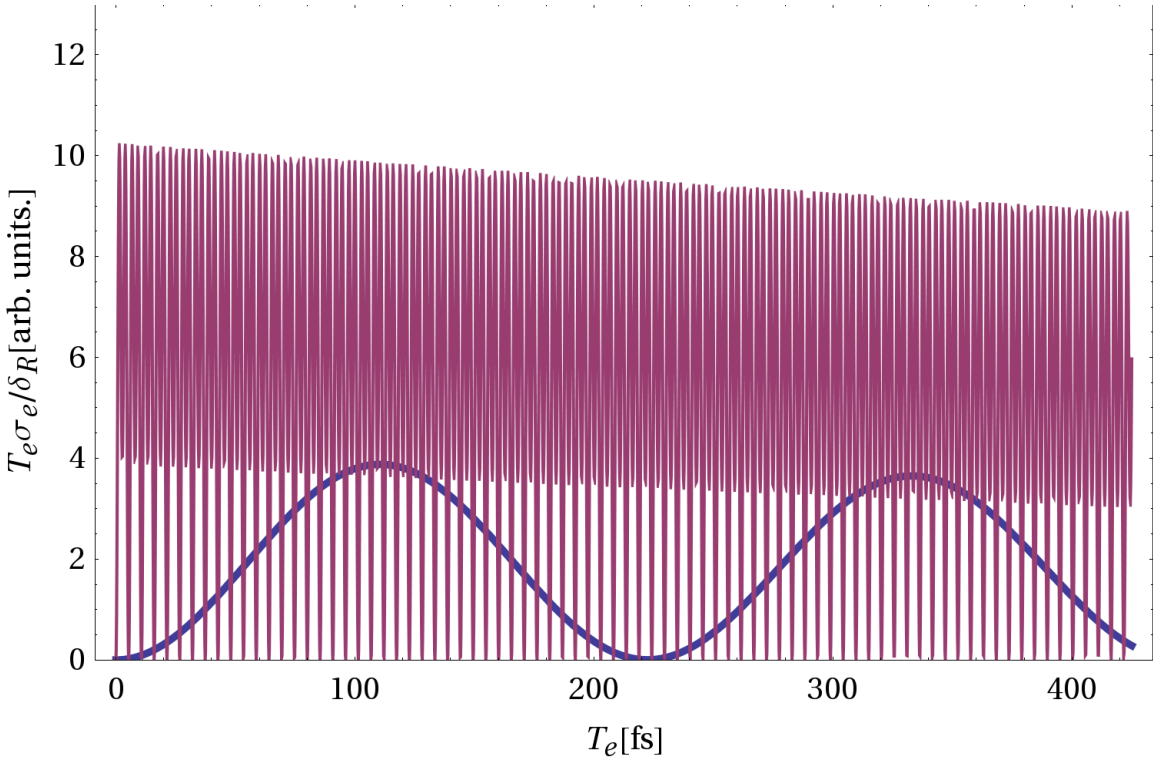

Figure 3.22. Variation of TPA signal with entanglement time for the two theoretical models depicted in Fig. 3 through intermediate levels (blue) and for a model with dominant permanent dipole mechanism (red). Where the y-axis is T_e (the entanglement time) multiplied by σ_e (the entanglement cross-section) is divided by the classical/random two-photon absorption cross-section (δ_R). The x-axis is entanglement time varied over several hundred femtoseconds. $T_e\sigma_e / \delta_R$ is plotted over entanglement time T_e to illustrate the contribution of the material dependent response due to the use of entangled photons.

3.6 ETPA Studies in Commercial Molecules

Using non-classical fields may provide new and novel ways to control molecular excitation. However, the molecular structures of the molecules used to study the effects of non-classical absorption are quite complex. This makes it difficult to tease out relevant information pertaining to the absorption the differing responses to differing absorption pathways. In order to study this further, molecules that are simpler and better studied were chosen. Most of the molecules that are studied and presented below are

molecules that are commercially available. The only novel chromophore studied in the absorption mechanism exploration of ETPA is the DCDHF fluorophore, LCA, studied in Chapter 2.

Jagatap et al derived the probability of excitation as a sum of both absorption contributions. When treated separately, both the dipolar and the virtual state mechanisms have orientationally average final state populations within the same order of magnitude. However, the presence of both competing pathways corresponds to a 0.006% drop in the final state population. This competition occurs in only heteronuclear diatomics and not homonuclear diatomics. We assume that in larger molecules this competition may be even more complex. To further test this hypothesis, we tested ZnTPP, 4-Dimethylamino-4'-nitrostilbene, Coumarin 30 and the DCDHF fluorophore.

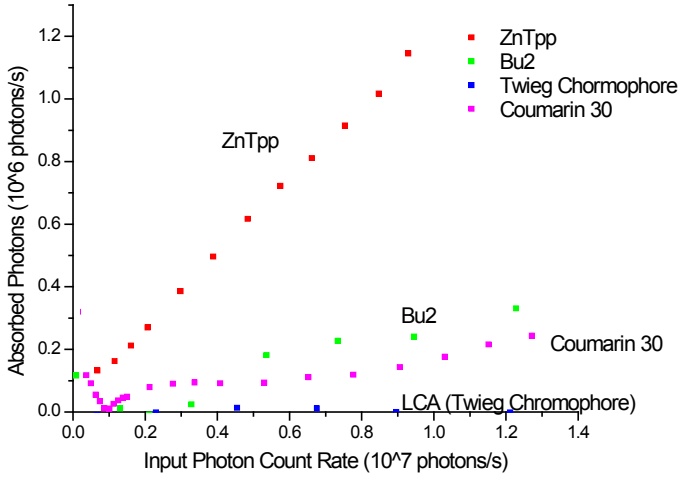

Figure 3.23. The entangled two-photon absorption rates of ZnTPP, Bu2, Coumarin 30 and LCA.

In Figure 3.23, the entangled two-photon absorption rates are plotted as functions of the input count rate. ZnTPP seems to exhibit the largest ETPA response. While, the DCDHF fluorophore (Twieg chromophore) does not seem to exhibit any ETPA. Both the 4-Dimethylamino-4'-nitrostilbene (Bu2) and Coumarin 30 exhibit moderate responses.

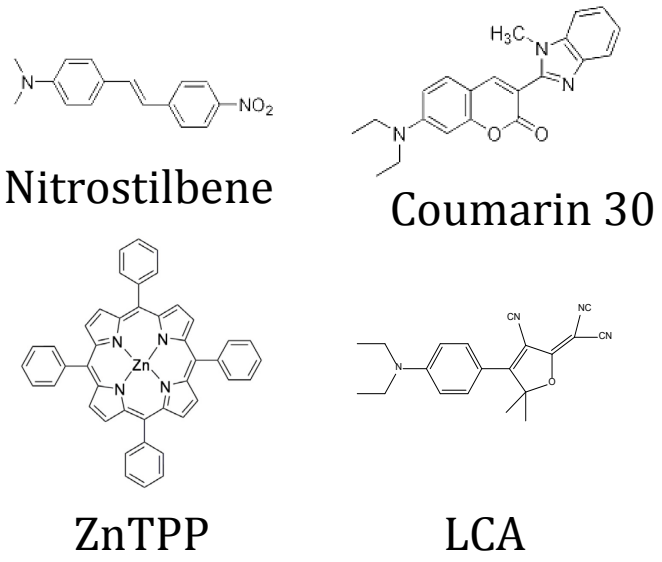

Figure 3.24. The structures of the molecules for this comparison for further ETPA absorption mechanism studies.

We'd also like to conduct future studies on Napthalene, Coronene, H2TPP and Perylene since these molecules do not have a permanent dipoles for further comparison.

3.7 Conclusions

In summary, we have now demonstrated entangled two-photon excited fluorescence on a set of nonlinear organic optical materials. With our method, we utilize the ten orders of magnitude enhancement previously seen in ETPA experiments to detect

measurable emission. This highly efficient nonlinear fluorescence and absorption is expected to have a large impact in quantum imaging, lithography, microscopy, and remote sensing. We have also demonstrated entangled two-photon absorption (ETPA) experiments on a set of nonlinear organic optical materials. Theoretical investigations have predicted [24, 27] that intermediate states far from resonance are not expected to contribute to the entangled two-photon absorption cross-section of a material. Our study has also provided both experimental and theoretical proof that intermediate states may be used to tune the ETPA process. This provides the possibility to observe fluorescence in some materials which actually have very small classical two-photon cross-sections. It was also found that the entanglement times used in our experiments may match values of entanglement induced transparency for all materials dominated by a particular pathway involving intermediate states. These results and theoretical predictions provide a new construct as to how certain materials may now be illuminated by undetectable photons and may be selectively illuminated by classical or non-classical light.

References:

[1] R. P. Feynman, "SIMULATING PHYSICS WITH COMPUTERS," *International Journal of Theoretical Physics,* vol. 21, pp. 467-488, 1982.

[2] D. S. Naik, C. G. Peterson, A. G. White, A. J. Berglund, and P. G. Kwiat, "Entangled State Quantum Cryptography: Eavesdropping on the Ekert Protocol," *Physical Review Letters,* vol. 84, pp. 4733-4736, 2000.

[3] K. S. Choi, A. Goban, S. B. Papp, S. J. van Enk, and H. J. Kimble, "Entanglement of spin waves among four quantum memories," *Nature,* vol. 468, pp. 412-416, 2010.

[4] N. K. Langford, S. Ramelow, R. Prevedel, W. J. Munro, G. J. Milburn, and A. Zeilinger, "Efficient quantum computing using coherent photon conversion," *Nature,* vol. 478, pp. 360-363, 2011.

[5] E. C. a. G. D. Scholes, "Coherent Intrachain Energy Migration in a Conjugated Polymer at Room Temperature," *Science,* vol. 323, pp. 369-373 2009.

[6] E. Collini, C. Y. Wong, K. E. Wilk, P. M. G. Curmi, P. Brumer, and G. D. Scholes, "Coherently wired light-harvesting in photosynthetic marine algae at ambient temperature," *Nature,* vol. 463, pp. 644-647, 2010.

[7] G. Panitchayangkoon, D. Hayes, K. A. Fransted, J. R. Caram, E. Harel, J. Wen*, et al.*, "Long-lived quantum coherence in photosynthetic complexes at physiological

temperature," *Proceedings of the National Academy of Sciences,* vol. 107, pp. 12766-12770, 2010.

[8] M. D. Reed, L. DiCarlo, S. E. Nigg, L. Sun, L. Frunzio, S. M. Girvin*, et al.*, "Realization of three-qubit quantum error correction with superconducting circuits," *Nature,* vol. advance online publication, 2012.

[9] J. B. Altepeter, P. G. Hadley, S. M. Wendelken, A. J. Berglund, and P. G. Kwiat, "Experimental Investigation of a Two-Qubit Decoherence-Free Subspace," *Physical Review Letters,* vol. 92, p. 147901, 2004.

[10] D. N. M. S. Olmschenk, P. Maunz, D. Hayes, L.-M. Duan, and C. Monroe, "**Quantum Teleportation Between Distant Matter Qubits**," *Science,* vol. **323**, pp. 486-489, 2009.

[11] M. R. Harpham, O. z. n. Süzer, C.-Q. Ma, P. Bäuerle, and T. Goodson, "Thiophene Dendrimers as Entangled Photon Sensor Materials," *Journal of the American Chemical Society,* vol. 131, pp. 973-979, 2009/01/28 2009.

[12] A. R. Guzman, M. R. Harpham, O. z. n. Süzer, M. M. Haley, and T. G. Goodson, "Spatial Control of Entangled Two-Photon Absorption with Organic Chromophores," *Journal of the American Chemical Society,* vol. 132, pp. 7840-7841, 2010/06/16 2010.

[13] D.-I. Lee and T. Goodson, "Entangled Photon Absorption in an Organic Porphyrin Dendrimer," *The Journal of Physical Chemistry B,* vol. 110, pp. 25582-25585, 2006/12/01 2006.

[14] C. Xu, W. Zipfel, J. B. Shear, R. M. Williams, and W. W. Webb, "Multiphoton fluorescence excitation: new spectral windows for biological nonlinear microscopy," *Proceedings of the National Academy of Sciences,* vol. 93, pp. 10763-10768, 1996.

[15] J. H. Bechtel and W. L. Smith, "Two-photon absorption in semiconductors with picosecond laser pulses," *Physical Review B,* vol. 13, pp. 3515-3522, 1976.

[16] W. M. H. McCain, R.A., *Two-Photon Molecular Spectroscopy in Liquids and Gases in Excited States*. New York: Academic, 1977.

[17] B. R. Mollow, "Two-Photon Absorption and Field Correlation Functions," *Physical Review,* vol. 175, pp. 1555-1563, 1968.

[18] M. Albota, "Design of Organic Molecules with Large Two-Photon Absorption Cross-Sections," *Science,* vol. 281, pp. 1653-1656, 1998.

[19] G. Ramakrishna and T. Goodson, "Excited-State Deactivation of Branched Two-Photon Absorbing Chromophores: A Femtosecond Transient Absorption Investigation," *J. Phys. Chem. A,* vol. 111, pp. 993-1000, 01/24 2007.

[20] B. N. Jagatap and W. J. Meath, "On the competition between permanent dipole and virtual state two-photon excitation mechanisms, and two-photon optical excitation pathways, in molecular excitation," *Chemical Physics Letters,* vol. 258, pp. 293-300, 1996.

[21] C. A. Marx and S. Mukamel, "Nonlinear spectroscopy with entangled photons: Manipulating quantum pathways of matter," vol. 79, p. 033832.

[22] S. Mukamel, "Ultrafast double-quantum-coherence spectroscopy of excitons with entangled photons," vol. 82, p. 013820.

[23] A. Joobeur, B. E. A. Saleh, T. S. Larchuk, and M. C. Teich, "Coherence properties of entangled light beams generated by parametric down-conversion: Theory and experiment," *Physical Review A,* vol. 53, pp. 4360-4371, 1996.

[24] J. Kojima and Q.-V. Nguyen, "Entangled biphoton virtual-state spectroscopy of the A2Σ+–X2Π system of OH," *Chemical Physics Letters,* vol. 396, pp. 323-328, 2004.

[25] J. Javanainen and P. L. Gould, "Linear intensity dependence of a two-photon transition rate," *Physical Review A,* vol. 41, pp. 5088-5091, 1990.

[26] J. Gea-Banacloche, "Two-photon absorption of nonclassical light," *Physical Review Letters,* vol. 62, pp. 1603-1606, 1989.
[27] F. Lissandrin, B. E. A. Saleh, A. V. Sergienko, and M. C. Teich, "Quantum theory of entangled-photon photoemission," *Physical Review B,* vol. 69, p. 165317, 2004.
[28] A. Ling, A. Lamas-Linares, and C. Kurtsiefer, "Absolute emission rates of spontaneous parametric down-conversion into single transverse Gaussian modes," *Physical Review A,* vol. 77, p. 043834, 04/28/ 2008.
[29] D. N. Klyshko, *Photons Nonlinear Optics*: CRC Press, 1988.
[30] P. G. Kwiat, K. Mattle, H. Weinfurter, A. Zeilinger, A. V. Sergienko, and Y. Shih, "New High-Intensity Source of Polarization-Entangled Photon Pairs," *Physical Review Letters,* vol. 75, pp. 4337-4341, 12/11/ 1995.
[31] A. V. Sergienko, M. Atatüre, Z. Walton, G. Jaeger, B. E. A. Saleh, and M. C. Teich, "Quantum cryptography using femtosecond-pulsed parametric down-conversion," *Physical Review A,* vol. 60, pp. R2622-R2625, 10/01/ 1999.
[32] M. H. Rubin, D. N. Klyshko, Y. H. Shih, and A. V. Sergienko, "Theory of two-photon entanglement in type-II optical parametric down-conversion," *Physical Review A,* vol. 50, pp. 5122-5133, 12/01/ 1994.
[33] A. Joobeur, B. E. A. Saleh, T. S. Larchuk, and M. C. Teich, "Coherence properties of entangled light beams generated by parametric down-conversion: Theory and experiment," *Physical Review A,* vol. 53, pp. 4360-4371, 1996.
[34] A. V. Sergienko, Y. H. Shih, and M. H. Rubin, "Experimental evaluation of a two-photon wave packet in type-II parametric downconversion," *Journal of the Optical Society of America B,* vol. 12, pp. 859-862, 1995/05/01 1995.
[35] Y.-H. Kim, M. V. Chekhova, S. P. Kulik, M. H. Rubin, and Y. Shih, "Interferometric Bell-state preparation using femtosecond-pulse-pumped spontaneous parametric down-conversion," *Physical Review A,* vol. 63, p. 062301, 05/07/ 2001.
[36] W. P. Grice and I. A. Walmsley, "Spectral information and distinguishability in type-II down-conversion with a broadband pump," *Physical Review A,* vol. 56, pp. 1627-1634, 08/01/ 1997.
[37] Y.-H. Kim, "Coherence properties of entangled two-photon states in quantum interferometry."
[38] B.-S. Shi and A. Tomita, "Generation of a pulsed polarization entangled photon pair using a Sagnac interferometer," *Physical Review A,* vol. 69, p. 013803, 01/09/ 2004.
[39] Y. Shih, "Entangled biphoton source-property and preparation," *Reports on Progress in Physics,* vol. 66, pp. 1009-1044, Jun 2003.
[40] M. Atatüre, A. V. Sergienko, B. E. A. Saleh, and M. C. Teich, "Dispersion-Independent High-Visibility Quantum Interference in Ultrafast Parametric Down-Conversion," *Physical Review Letters,* vol. 84, pp. 618-621, 01/24/ 2000.
[41] D. Pan, W. Donaldson, and R. Sobolewski, "Femtosecond laser-pumped source of entangled photons for quantum cryptography applications," in *International Congress on Optics and Optoelectronics*, 2007, pp. 65830K-65830K-9.
[42] A. Bhaskar, G. Ramakrishna, Z. Lu, R. Twieg, J. M. Hales, D. J. Hagan*, et al.*, "Investigation of Two-Photon Absorption Properties in Branched Alkene and Alkyne Chromophores," *Journal of the American Chemical Society,* vol. 128, pp. 11840-11849, 2006/09/01 2006.
[43] C.-Q. Ma, E. Mena-Osteritz, T. Debaerdemaeker, M. M. Wienk, R. A. J. Janssen, and P. Bäuerle, "Functionalized 3D Oligothiophene Dendrons and Dendrimers— Novel Macromolecules for Organic Electronics," *Angewandte Chemie International Edition,* vol. 46, pp. 1679-1683, 2007.

[44] O. Varnavski, X. Yan, O. Mongin, M. Blanchard-Desce, and T. Goodson, "Strongly Interacting Organic Conjugated Dendrimers with Enhanced Two-Photon Absorption," *The Journal of Physical Chemistry C,* vol. 111, pp. 149-162, 2007/01/01 2006.

[45] M. Drobizhev, F. Meng, A. Rebane, Y. Stepanenko, E. Nickel, and C. W. Spangler, "Strong Two-Photon Absorption in New Asymmetrically Substituted Porphyrins: Interference between Charge-Transfer and Intermediate-Resonance Pathways," *The Journal of Physical Chemistry B,* vol. 110, pp. 9802-9814, 2006/05/01 2006.

[46] P. Macak, Y. Luo, P. Norman, and H. Agren, "Electronic and vibronic contributions to two-photon absorption of molecules with multi-branched structures," *The Journal of Chemical Physics,* vol. 113, pp. 7055-7061, 2000.

[47] J.-D. Guo, C.-K. Wang, Y. Luo, and H. Agren, "Influence of electron-acceptor strength on the resonant two-photon absorption cross sections of diphenylaminofluorene-based chromophores," *Physical Chemistry Chemical Physics,* vol. 5, 2003.

[48] M. Kruk, A. Karotki, M. Drobizhev, V. Kuzmitsky, V. Gael, and A. Rebane, "Two-photon absorption of tetraphenylporphin free base," *Journal of Luminescence,* vol. 105, pp. 45-55, 2003.

[49] J. Peřina, Jr., B. E. A. Saleh, and M. C. Teich, "Multiphoton absorption cross section and virtual-state spectroscopy for the entangled n-photon state," *Physical Review A,* vol. 57, pp. 3972-3986, 1998.

[50] B. E. A. Saleh, B. M. Jost, H.-B. Fei, and M. C. Teich, "Entangled-Photon Virtual-State Spectroscopy," *Physical Review Letters,* vol. 80, pp. 3483-3486, 1998.

[51] O. Roslyak and S. Mukamel, "Multidimensional pump-probe spectroscopy with entangled twin-photon states," *Physical Review A,* vol. 79, p. 063409, 2009.

[52] H.-B. Fei, B. M. Jost, S. Popescu, B. E. A. Saleh, and M. C. Teich, "Entanglement-Induced Two-Photon Transparency," *Physical Review Letters,* vol. 78, pp. 1679-1682, 1997.

[53] C. Katan, F. Terenziani, O. Mongin, M. H. V. Werts, L. Porrès, T. Pons*, et al.*, "Effects of (Multi)branching of Dipolar Chromophores on Photophysical Properties and Two-Photon Absorption," *The Journal of Physical Chemistry A,* vol. 109, pp. 3024-3037, 2005/04/01 2005.

[54] S. A. Lahankar, R. West, O. Varnavski, X. Xie, T. Goodson, L. Sukhomlinova*, et al.*, "Electronic interactions in a branched chromophore investigated by nonlinear optical and time-resolved spectroscopy," *The Journal of Chemical Physics,* vol. 120, pp. 337-344, 2004.

Chapter 4

Virtual State Contribution to ETPA in Diatomic Molecules

Abstract: As computational methods and experimental designs seek to utilize quantum theory to probe molecules, there is a need for more experimental and theoretical data for entangled two-photon absorption processes. With the use of non-classical fields, we hypothesize that entangled photons can differentiate between differing absorption mechanisms of a molecule. Molecules that absorb photons via a virtual state do absorb entangled photons, while those that absorb via a permanent dipole do not. In order to explore this hypothesis further, we utilize a modified entanagled two-photon absorption cross-section to compare homonuclear and heteronuclear diatomic molecules. For this study, we compare the entangled two-photon absorption cross-sections in N2 and NO.

The work presented in this chapter will be submitted for publication as a peer-reviewed journal article with the citation Leslie Upton, Andrew Molina, Paul Zimmerman, Theodore Goodson III, The Journal of Physical Chemistry Letters (submitted, 2015).

4.1 Introduction

The use of non-classical fields may provide spectroscopists with an enhanced tool set to study and probe organic molecules. Such theory predicts the departure from classical multiphoton spectroscopy [1, 2]. This was first experimentally demonstrated by Georgiades et al in trapped atomic cesium [3]. This work was then expanded upon and extended to large organic molecules. It was shown that non-classical experiments could be carried out with ten orders of magnitude less photons and these multiphoton experiments exhibited a linear intensity dependence which both suggest non-classical phenomena [4-6]. Some particularly interesting results showed that some conjugated molecules with large classical two-photon absorption did not exhibit entangled two-photon absorption while other molecules with large classical absorption cross-sections did [7].

This chapter describes the first application of the modified entangled two-photon absorption cross-section to compare diatomic molecular systems. With the use of non-classical fields, we hypothesize that entangled photons can differentiate between differing absorption mechanisms of a molecule. Molecules that absorb photons via a virtual state do absorb entangled photons, while those that absorb via a permanent dipole do not [7]. In order to explore this further, we utilize a modified entangled two-photon absorption cross-section to compare homonuclear and heteronuclear diatomic molecules. For this study, we compare the theoretically calculated entangled two-photon absorption cross-sections in N2, NO and HF.

To better understand entangled two-photon absorption it is critical that both the molecular structures of the molecules and the statistics and parameters of the fields are

understood and well characterized. In order to take the molecular structure into account a modified entangled two-photon absorption cross-section was suggested to account for the differences in the entangled two-photon absorption response. Classically multiphoton absorption can arise from two distinct excitation mechanisms, the first being a non-zero permanent dipole difference between the ground and the excited state, and the second occurring via a virtual state. A schematic of the absorption two absorption mechanisms is given in Figure 4.1.

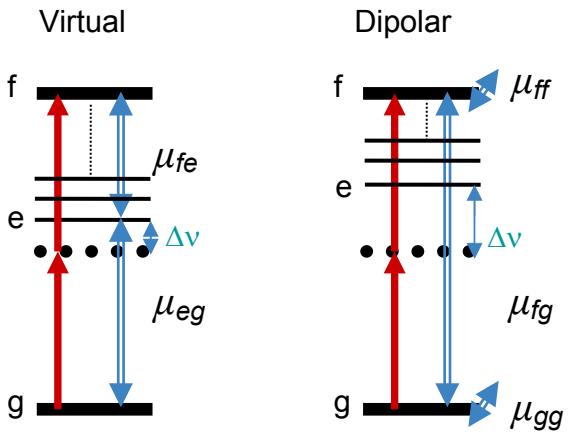

Figure 4.1. Schematic depiction of two-photon absorption pathways. The virtual state (left) and dipolar (right) pathways of classical two-photon absorption are illustrated. Final, intermediate, and ground states are denoted by f, e, and g, respectively. μ is the transition dipole moment is represented as. Photon energies and transition dipole moments are represented by filled and hollow arrows, respectively.

4.1.1 Dipolar Mechanism

In the dipolar mechanism, the ground to final state transition is dipole allowed [8, 9]. In this case, the ground and the final state are coupled to each other. The virtual state is not near a real intermediate state, and thus the detuning between the virtual state and

the intermediate state is large. This can also be thought of as a coherent superposition of the ground and excited states. This is analogous to the classical model for absorption in a molecule with a permanent dipole.

4.1.2 Virtual State Mechanism

Within the virtual state mechanism, the ground state is coupled to some intermediate state. The intermediate state is also coupled to the final state of the system. A virtual state is near a real intermediate state of the molecule and thus the detuning between the field and the state is small. Virtual states generally have lifetimes on the order of 5 fs [8].

Classically the population of excited states can be tuned with the use of two laser beams. This is achieved through manipulating the polarization angle between and the phase difference between the beams [10, 11]. With the use of two beams and the manipulation of the polarization and the phase parameters, one must also consider the interference that arises between the two different absorption mechanisms and the interferences associated with excitation via two beams. We must keep these considerations in mind since the entangled two-photon absorption field is a two beam field composed of the signal and idler beam. Thus the modified entangled two-photon absorption cross-section is given by [7]:

$$\sigma_e = \frac{A}{\hbar^2 \varepsilon_0^2 A_e T_e} \omega_0^2 \delta(\varepsilon_f - \varepsilon_g - 2\omega_0) \left| \frac{1 - e^{-i(\omega_0 + \varepsilon_g - \varepsilon_e)T_e - \kappa_e T_e/2}}{(\omega_0 + \varepsilon_g - \varepsilon_e) - i\kappa_e/2} \mu_{fe} \cdot e_i \mu_{eg} \cdot e_s \right.$$
$$\left. + \frac{1 - e^{-i\omega_0 T_e - \kappa_g T_e/2}}{\omega_0 - i\kappa_g/2} \mu_{fg} \cdot e_i \mu_{gg} \cdot e_s + \frac{1 - e^{i\omega_0 T_e - \kappa_f T_e/2}}{-\omega_0 - i\kappa_f/2} \mu_{ff} \cdot e_i \mu_{fg} \cdot e_s \right|^2$$

where A_E and T_E are entanglement area and entanglement time, respectively, ω_0 is the frequency of the signal and idler photons, e_i, e_s are the polarization of signal and idler, ε_g, ε_e and ε_f are the frequency of the ground, intermediate and excited state, respectively, μ_{ij} are the transition dipole matrix elements and κ_j are the state linewidths.

In the case of the macromolecules studied, the absorption mechanisms and interferences may be very complicated because of conformational changes in the excited states and the presence of many competing pathways [11-14]. Thus it may be quite difficult to determine the exact absorption pathways and isolate interfering pathways. While, large conjugated systems make entangled two-photon absorption a more experimentally viable technique, these molecules do little to illuminate the core interactions of the entangled photons with the excited states of our systems of interest because the exact excited states are not known. Therefore, we shift our focus from these large conjugated systems to small diatomics. We hope that with better knowledge of the excited states, we can uncover fundamental differences between the mechanisms of entangled and classical two-photon absorption, and the roles the detuning and the relative magnitudes of the matrix elements play.

4.2 Computational Results

A theoretical study on the heteronuclear diatomic molecule OH showed the presence of entanglement induced transparency in the hydroxyl radical (OH) [15]. This was demonstrated using an entangled two-photon absorption cross-section derived using second order perturbation theory and neglecting the intermediate state linewidths [16, 17].

$$\sigma_e = \frac{2\,\pi}{\hbar {\epsilon_0}^2 c^2 A_e T_e}\,\omega_1^0 \omega_2^0 \delta\left(\varepsilon_f - \varepsilon_i - \omega_1^0 - \omega_2^0\right) \qquad Equation\ 4.1$$

$$\times \left| \sum_j D_j \left\{ \frac{1 - \exp[-iT_e \Delta_j^1]}{\Delta_j^1} + \frac{1 - \exp[-iT_e \Delta_j^1]}{\Delta_j^1} \right\} \right|^2$$

The selection rule allowed two-photon transitions were determined for the $A^2\Sigma^+$-$X^2\,\Pi$ transition in OH. The initial state is 544.21 cm^{-1}, and the final state is 33,150.15 cm^{-1} [18]. A two-step process was in which the population is excited from the ground to intermediate state (X–X, or X–A) and from the intermediate state to some excited state (X–A, or A–A). These energies were calculated based on the Hamiltonian derived by Luque and Crosley [19]. Both electronic (A–X transitions) and vibrational (X–X or A–A) transition moments, energies and lifetimes were calculated and included in the database. The wave functions used to calculate the potential energy curves were found after solving the the the radial Schrodinger equation. The potential curves were calculated using the Rydberg–Klein–Rees (RKR) method. The rotational centrifugal term was included [15].

The entangled two-photon absorption cross-section was calculated for 53 different intermediate states [20]. We used the same data, re-wrote the QEMASS program in Mathematica, and recalculated and re-plotted the cross-sections in *Figure 4.2*. In order to theoretically compare the original ETPA cross-section with the modified entangled cross-section. By not including the dipolar terms, some important physics may have been missed within the ETPA cross-section.

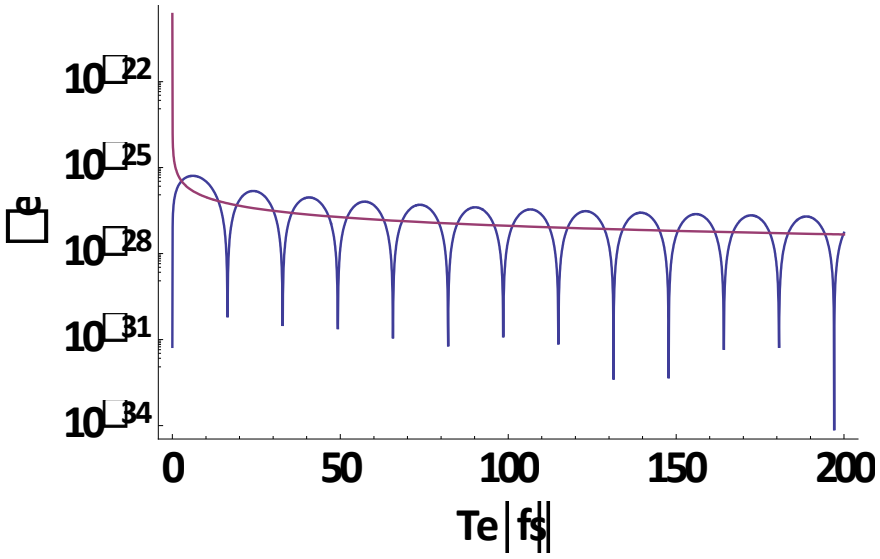

Figure 4.2. The entangled two-photon cross-section for the A-X transition in OH as a function of entanglement time. The pump is degenerate. This is based on the data by Kojima and Nguyen. The graph was reproduced based on their QEMASS method for ETPA cross-section calculation.

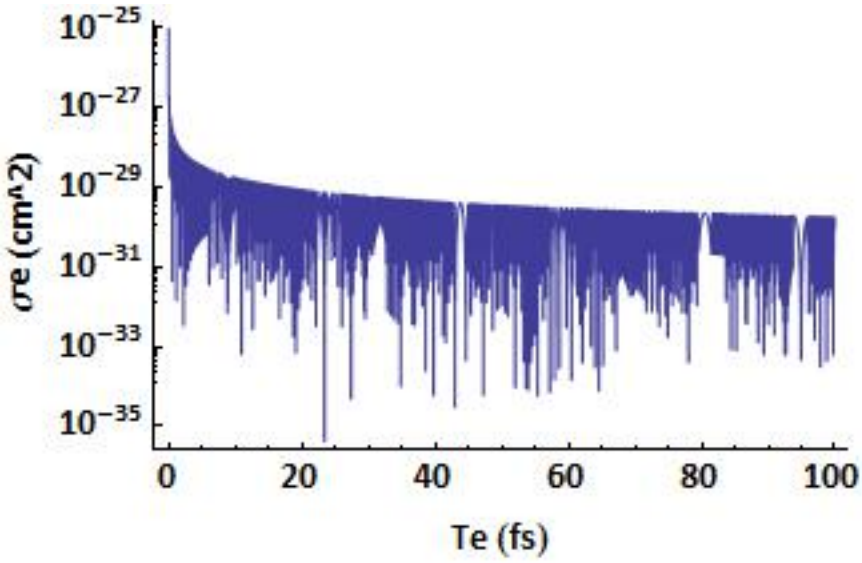

Figure 4.3. Using the transition data from Kojima we compared the original cross-section with the modified cross-section in order to plot the ETPA cross-section as a function of entanglement time.

The period of the oscillations in Figure 4.2 are ~15 fs. The oscillations between the maxima are much smaller for the modified cross-section, which is given in Figure 4.3. The spacings are approximately 10^{-4} fs. This suggests complex interference, since OH is a heteronuclear diatomic molecule.

We now compare a Di-Nitrogen (N2) molecule with Nitric Oxide (NO). As we know, N2 does not have a dipole moment. We probe the $X\ ^1\Sigma_g \rightarrow\ a'\ ^1\Sigma_u\ and\ a'\ ^1\Sigma_u \rightarrow a'\Pi_g$ transition which occurs via the $a'\ ^1\Sigma_u$ transition [21]. For NO, we probe the $X \rightarrow A$ and $A \rightarrow C$ transitions which occur via the A intermediate state [10]. The dipole for NO is 0.153 D. We also consider HF which has a larger dipole moment (1.91 D) than NO. For HF, we probe the $X\Sigma^+ \rightarrow\ ^1\Pi\ and\ \ ^1\Pi \rightarrow\ ^1\Sigma^+$ transitions.

4.2.1 MOLPRO Calculations

In order to complete these calculations, the transition moments are needed. Finding the transition moments for these states was not trivial. While Lifbase does have an extensive collection of energies, transition moments and lifetimes some of the two-photon transitions needed for the molecules studied were not listed or available in this database [18]. While some of the needed values were in the literature, more often than not the transitions needed for this work were not available. Therefore, we sought to calculate these values ourselves using MOLPRO and MRCI methods [22]. We only consider electronic transitions in this work.

These calculations were calculated in aug-cc-pvtz basis sets by Dunning and co-workers [23]. This basis set was used to calculate and obtain the potential energy curves (PECs) for the various states of interest using the method outlined by Peng-Fei et al [24].

The calculations were carried out with Hartree-Fock, CASSCF and MRCI level theory [25-29]. Due to limitations within MOLPRO, the $D_{\infty h}$ and $C_{\infty v}$ symmetry groups of the diatomic molecules studied were simplified to D_{2h} and C_{2v}. A_1 states represent Σ^+ states and A_2 states represent Σ^- states in molecules with C_{2v} symmetry [24]. Degenerate states Δ and Π are represented by A1+A2 and B1+B2. The actual physical excited state transition assignments were deciphered using the given relations. The ground state for N2 is $[1\sigma_g{}^2\ 1\sigma_u^2\ 2\sigma_g{}^2\ 2\sigma_u^2\ 1\,\pi_u{}^4 3\sigma_g{}^2]$, and the active space is enlarged to include two A_g and two B_u states. The ground state for NO is given by $[1\sigma^2\ 2\sigma^2\ 3\sigma^2\ 4\sigma^2\ 1\,\pi^4 5\sigma^2 2\pi^1$. The active space is designated by 4 A_1 states two B_1 states, and two B_2 states. The ground state configuration for HF is $(2s_F)^2(\sigma_b)^2(2p_{xF})^2(2p_{yF})^2$, while the computational active space is an additional A_1 state was added. Further details regarding the calculations can be found in Chapter 5.

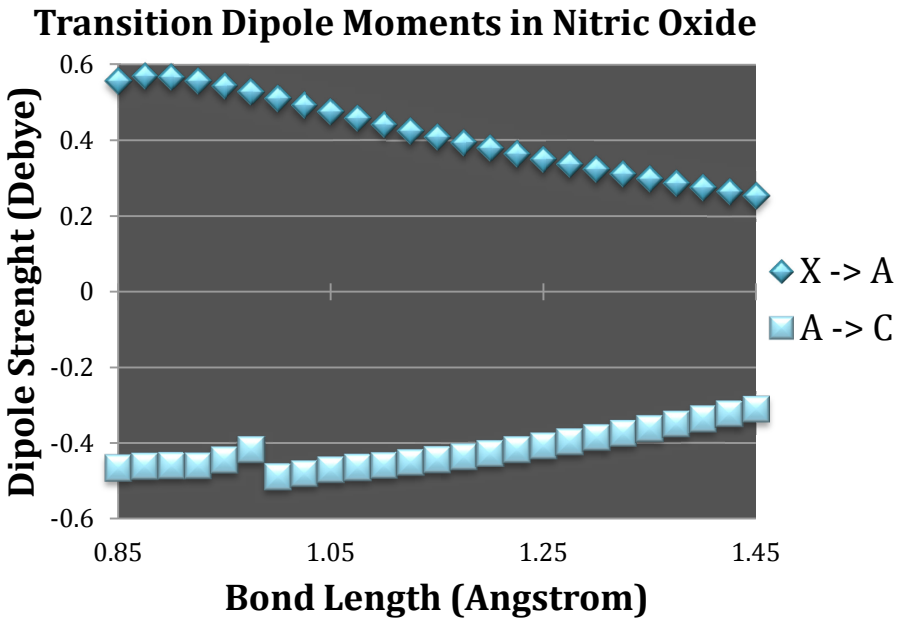

Figure 4.4. The transition dipole moments are plotted as a function of the bond length over the range of 0.85 Ang to 1.45 Ang.

N_2: Transition Dipoles					
abs(DMX)	1.2	2.2	1.5	2.5	3.5
1.1	2.27	0.86	--	--	--
1.6	--	--	0.41	0.80	--
2.6	--	--	0.64	0.80	0.63
abs(DMZ)	1.2	2.2	1.5	2.5	3.5
1.1	--	--	0.17	1.64	2.94
1.6	1.54	0.53	--	--	--
2.6	0.12	0.11	--	--	--

Table 4.1. The absolute values of the x and z components of the calculated transition dipole moments. Dipole moments less than 0.05 D were omitted.

For N2, the calculated transition moments are given in Figure 4.4. The transition dipoles for nitric oxide were calculated at the equilibrium bond length of 1.15 Angstrom. The values for the x and z components are listed in Table 4.1. The transition dipole moments for the transitions in hydrogen fluoride are 1.54 D for the $X\Sigma^+ \rightarrow {}^1\Pi$ transition and 1.77 D for the ${}^1\Pi \rightarrow {}^1\Sigma^+$ transition.

4.3 Mathematica

4.3.1 Comparision Results calculated in Mathematica

Using the basis for the QEMASS program, we now use the calculated transition moments to compare the entangled two-photon absorption cross-sections of different diatomic molecules [15]. We begin by comparing N2 and NO. The choice of molecules was based on the abundance of literature available on these molecule's transitions. The cross-sections were calculated and plotted as functions of the entanglement time [16].

4.3.1.1 N2 versus NO

Because of the time correlations of the entangled photons, the entangled two-photon absorption cross-sections are non-monotonic. The entangled two-photon absorption cross-section of N2 is given in Figure 4.5. The cross-section is on the order of magnitude of 10^{-28} cm^2, this is comparable to other calculated values, which range from 10^{-17}-10^{-32} depending on the transition [15]. The entanglement-induced transparency is very small and the first transparency does not appear until 925 fs. Note that the minima are approximately 1 to 3 orders of magnitude smaller than the maxima. The entangled two-photon absorption cross-section is effectively constant over experimental constraints. The cross-section for nitric oxide is plotted in Figure 4.6. One can see that the frequency of the induced transparencies is increased. It's a bit hard to resolve in Figure 4.6, but the space between the transparencies is 10^{-4} fs. The cross-section is on the order of magnitude of 10^{-26} cm^2. We extend the range of entanglement times, and we re-plot NO with an entanglement time range of 0 to 1000 fs in Figure 4.7.

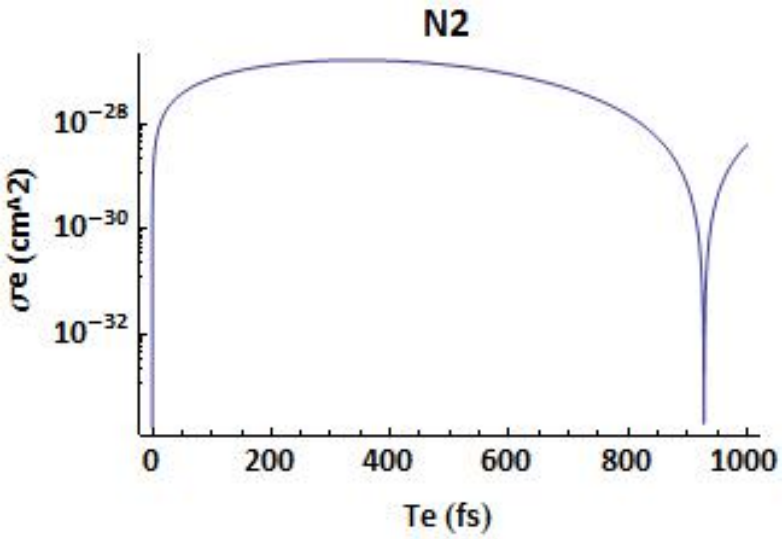

Figure 4.5. The entangled two-photon absorption cross-section as a function of entanglement time for N2.

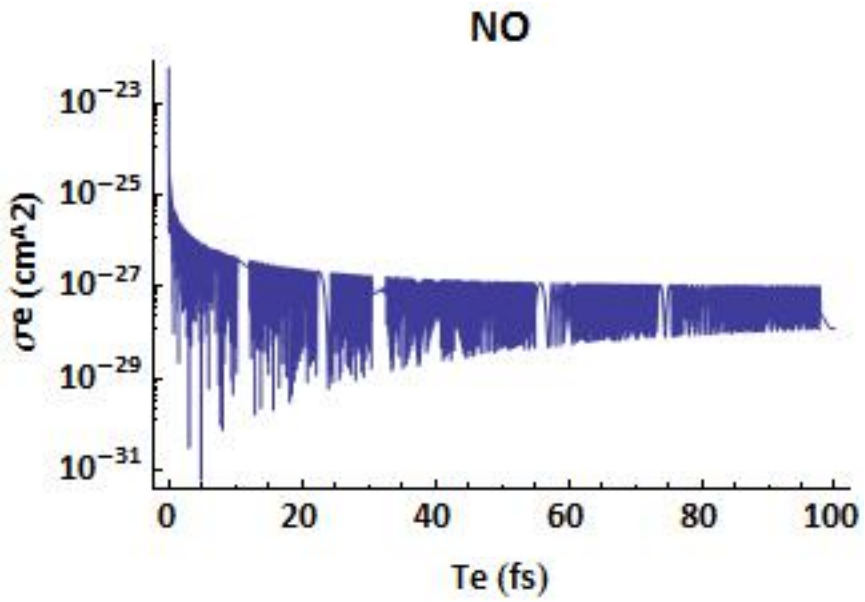

Figure 4.6. The entangled two-photon absorption cross-section as a function of entanglement time for NO.

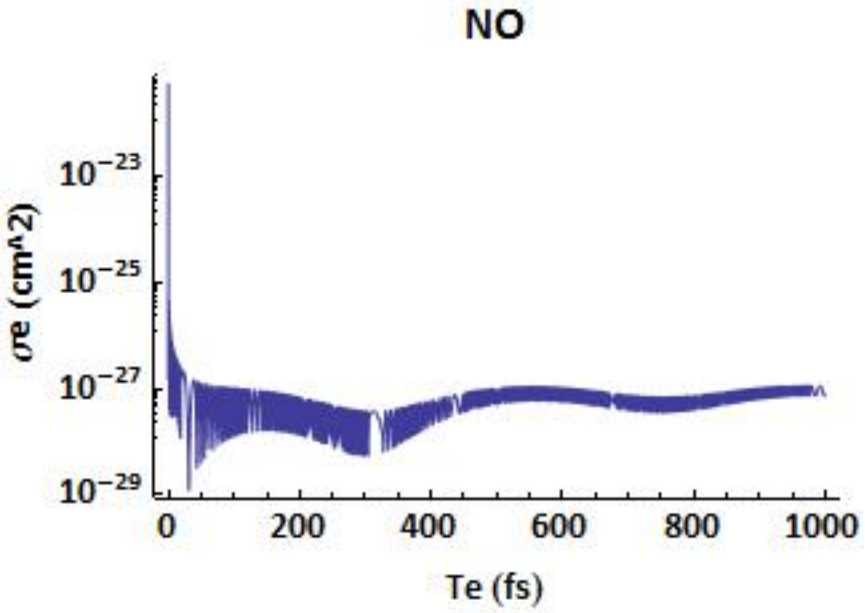

Figure 4.7. The entangled two-photon absorption cross-section as a function of entanglement time for NO from 0 to 1000 fs.

4.3.1.2 Hydrogen Fluoride

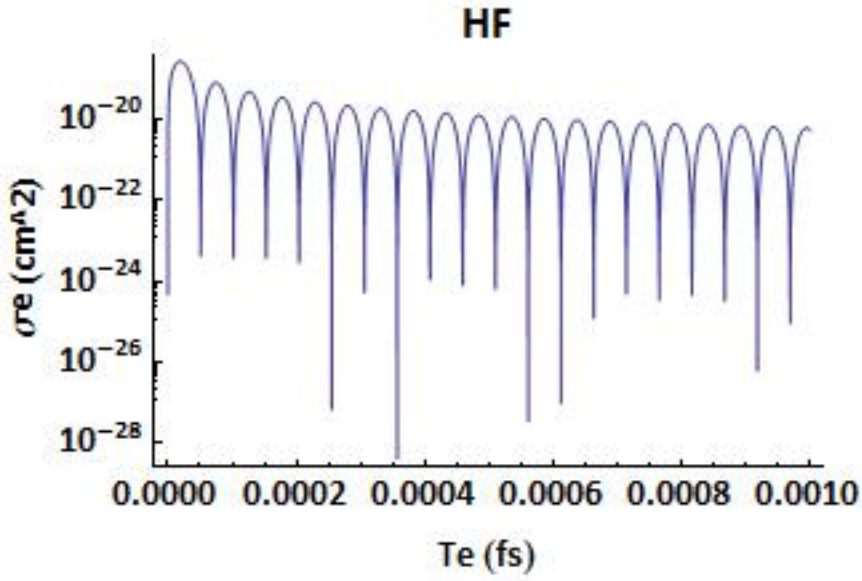

Figure 4.8. The entangled two-photon absorption cross-section as a function of entanglement time for HF.

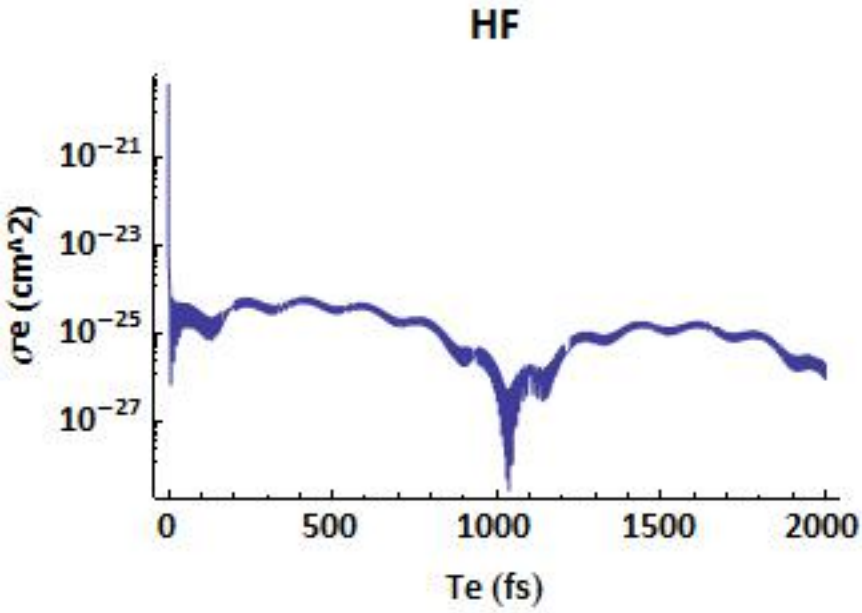

Figure 4.9. The entangled two-photon absorption cross-section as a function of entanglement time for HF from 0 to 2000 fs.

We use the same method to calculate the ETPA cross-section for hydrogen fluoride using the modified cross-sectional equation. The spacings for HF are an order of magnitude smaller than the spacings for NO. If we extend the entanglement time out to 2000 fs, we notice that the plot is similar to the non-degenerate ETPA cross-sectional measurements by Kojima [15]. This perhaps should be explored further.

4.3.2 Importance of relative magnitudes of the matrix elements

The modified cross-section has three terms, a virtual state term and two dipolar terms. Each of these terms are multiplied by either the transition dipole moments or the permanent dipole moments. We explore the effect of the magnitudes of the transition dipole moments for N2.

4.3.2.1 Dependence on Transition Dipole Moments

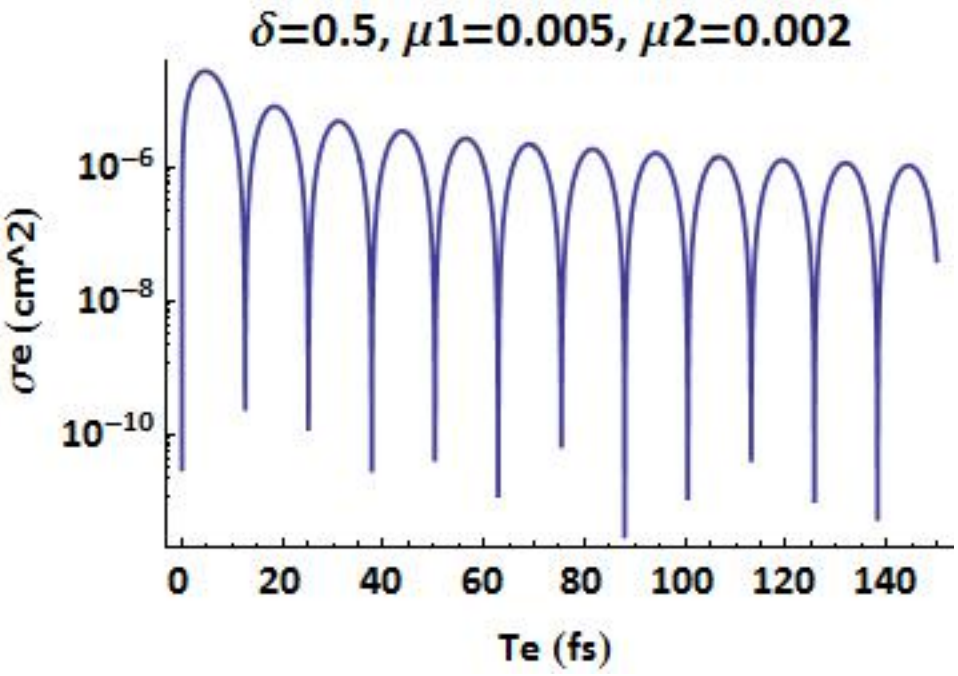

Figure 4.10. The ETPA cross-section of N2 with modified matrix elements (δ=0.5, μ1=10, μ2=10).

We also compare the non-dimensionalized magnitudes of the transition moments with the same detunings. The first example is plotted in Figure 4.10. The detuning is given as 0.5 and first and second transition moments are 10. The second example is given in Figure 4.11, where the detuning is again 0.5 and in this case the first and second transition moments are 0.005 and 0.002 respectively. This combination of transition moments can become even more complicated when permanent dipoles are introduced. In terms of experimental design these quantities all become fair game in tailoring molecules for entangled two-photon absorption in experimental design.

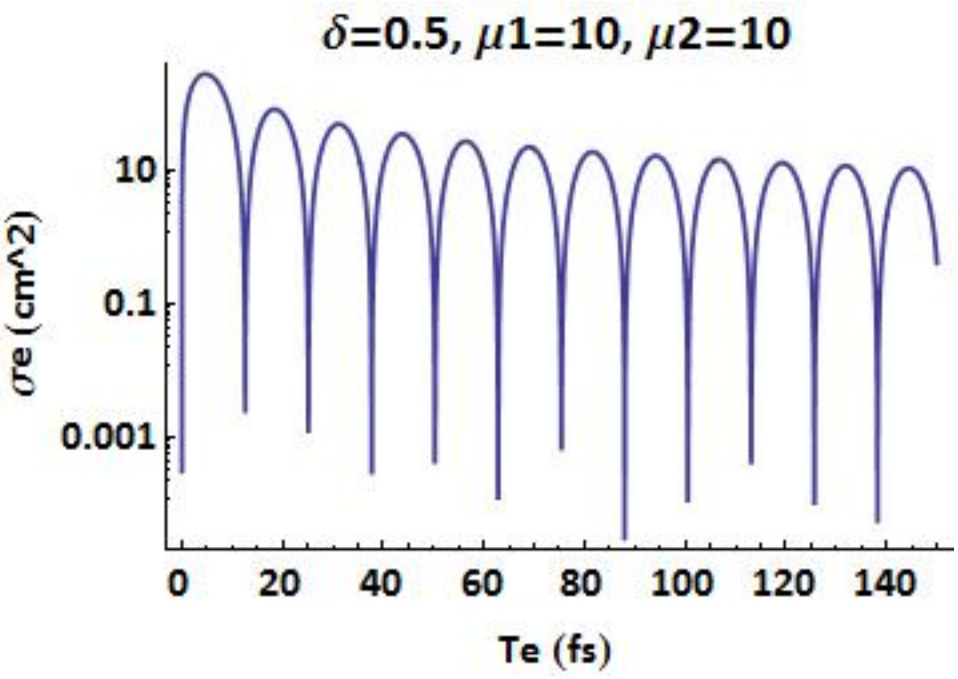

Figure 4.11. The ETPA cross-section of N2 with modified matrix elements (δ=0.5, μ1=0.005, μ2=0.002). The cross-section is now six orders of magnitude smaller.

We compare the entangled two-photon absorption cross-section of N2 as we vary the detuning (δ), where exact two-photon resonance is δ=0. When the detuning is 0.5, the spacings between the entanglement-induced transparencies are on the order of 15 fs. This is shown in Figure 4.12.

4.3.3 Importance of Detuning

Javanainen and Gould suggest that an exact two-photon resonance is needed, as well as an appropriate two-photon transition. In this case, according to Javanainen the requirements for an appropriate transition are a detuning of less than 50 cm^{-1} for a correlation time of 100 fs. The frequency of the oscillations is also decreases are the pump photon energy difference increases [15].

4.3.3.1 The Dependence on Detuning

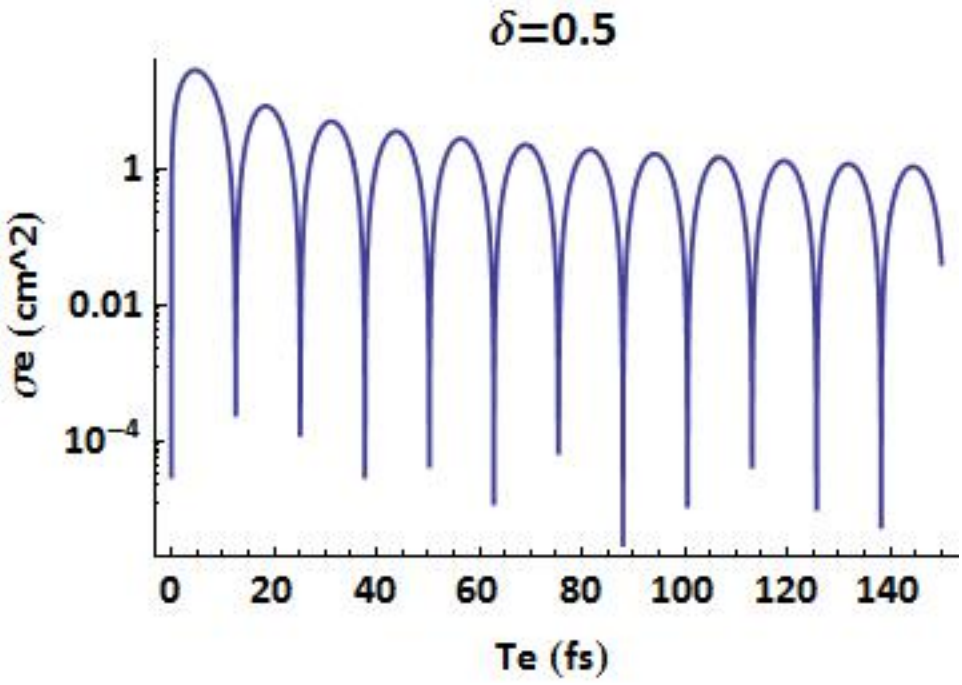

Figure 4.12. The ETPA cross-section of N2 is given as a function of the entanglement time. The detuning is δ = 0.5.

With a detuning of 0.5, the spacing is 10 fs. However, if we can lower the detuning to δ=0.05 than the spacing becomes approximately 125 fs, which is given in Figure 4.13. This suggests that the more on resonance one is with the intermediate state the more "classical" the entangled two-photon absorption cross-section appears over a large range of entanglement times. As δ goes to zero, the entangled two-photon absorption cross-section appears to become almost constant over the relevant experimental entanglement time. We also note the differences in the order of magnitude between the two specified detunings. For δ=0.5 and δ=0.05 the difference is an approximately an order of magnitude. As the detuning decreases and the spacings between the maxima increase, the cross-section also drops an order of magnitude. This suggests that there may be some interplay that experimentalists must maximize between the order of magnitude of the cross-section and the spacing between the transparencies.

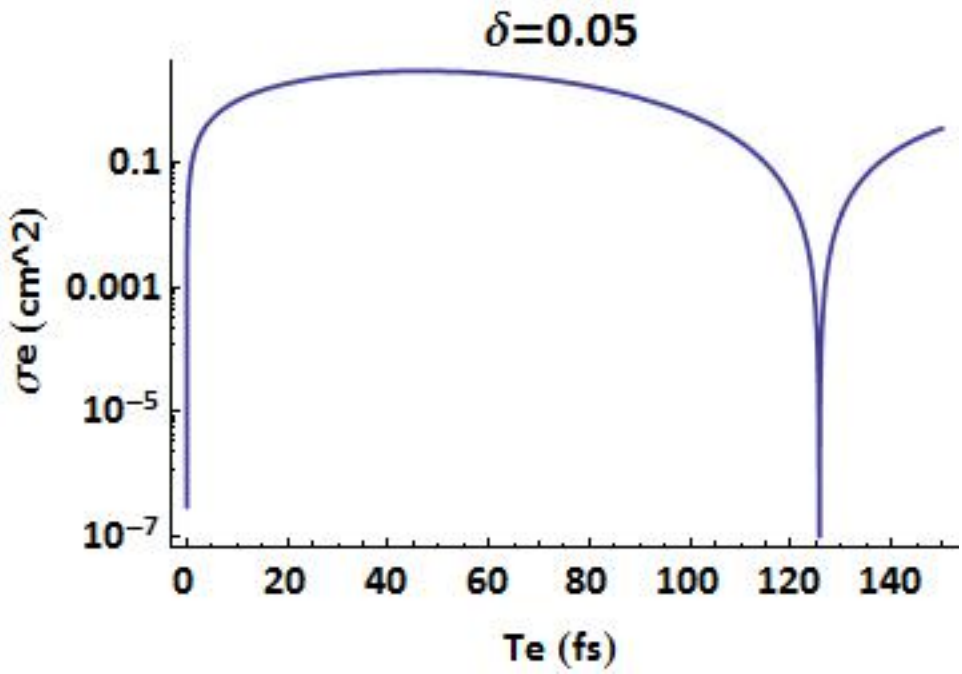

Figure 4.13. The ETPA cross-section of N2 is given as a function of the entanglement time. The detuning is δ = 0.05.

4.4 Conclusions

In conclusion, I have shown that homonuclear and heteronuclear diatomic molecules exhibit very different entangled photon absorption cross-sections when the cross-sections are plotted using the modified entangled two-photon absorption cross-section. The permanent dipole in heteronuclear diatomics adds a competing pathway to what many assume as is the dominant virtual state pathway for ETPA. These competing pathways interfere with each other and create a complex beating pattern, which is seen for NO. This increases the frequency of the cross-sectional maxima oscillations and may require femtosecond resolution to achieve maximum absorption. We also notice that the oscillations of the cross-section for HF are an order of magnitude smaller than those of NO. The differences in the cross-sectional behavior may allow one to utilize the three orders of magnitude difference between the minima and maxima to effectively "turn on" and "turn off" the ETPA signal in molecules such as N2. However, this is not easily achieved in the heteronuclear diatomic molecules in which the oscillations may to be close to resolve with current technology.

Similar to the two-photon absorption process, we also showed that the cross-section is also dependent on the relative magnitudes of the transition dipole moments. However, unlike classical two-photon absorption the ways in which the absorption mechanisms of heteronuclear molecules interfere greatly impact ETPA. Maximizing these parameters in novel organic molecules to reduce interference may be the key to rational material design and the development of molecules with maximized ETPA cross-sections.

References:

[1] J. Javanainen and P. L. Gould, "Linear intensity dependence of a two-photon transition rate," *Physical Review A,* vol. 41, pp. 5088-5091, 1990.

[2] F. Lissandrin, B. E. A. Saleh, A. V. Sergienko, and M. C. Teich, "Quantum theory of entangled-photon photoemission," *Physical Review B,* vol. 69, p. 165317, 2004.

[3] N. P. Georgiades, E. S. Polzik, K. Edamatsu, H. J. Kimble, and A. S. Parkins, "Nonclassical Excitation for Atoms in a Squeezed Vacuum," *Physical Review Letters,* vol. 75, pp. 3426-3429, 11/06/ 1995.

[4] D.-I. Lee and T. Goodson, "Entangled Photon Absorption in an Organic Porphyrin Dendrimer," *The Journal of Physical Chemistry B,* vol. 110, pp. 25582-25585, 2006/12/01 2006.

[5] M. R. Harpham, O. z. n. Süzer, C.-Q. Ma, P. Bäuerle, and T. Goodson, "Thiophene Dendrimers as Entangled Photon Sensor Materials," *Journal of the American Chemical Society,* vol. 131, pp. 973-979, 2009/01/28 2009.

[6] A. R. Guzman, M. R. Harpham, O. z. n. Süzer, M. M. Haley, and T. G. Goodson, "Spatial Control of Entangled Two-Photon Absorption with Organic Chromophores," *Journal of the American Chemical Society,* vol. 132, pp. 7840-7841, 2010/06/16 2010.

[7] L. Upton, M. Harpham, O. Suzer, M. Richter, S. Mukamel, and T. Goodson, III, "Optically Excited Entangled States in Organic Molecules Illuminate the Dark," *Journal of Physical Chemistry Letters,* vol. 4, pp. 2046-2052, Jun 20 2013.

[8] M. Pawlicki, H. A. Collins, R. G. Denning, and H. L. Anderson, "Two-Photon Absorption and the Design of Two-Photon Dyes," *Angewandte Chemie International Edition,* vol. 48, pp. 3244-3266, 2009.

[9] T. Kogej, D. Beljonne, F. Meyers, J. W. Perry, S. R. Marder, and J. L. Brédas, "Mechanisms for enhancement of two-photon absorption in donor–acceptor conjugated chromophores," *Chemical Physics Letters,* vol. 298, pp. 1-6, 12/11/ 1998.

[10] H. Lefebvre-Brion and R. W. Field, *The spectra and dynamics of diatomic molecules*. Amsterdam ; Boston: Elsevier Academic Press, 2004.

[11] B. N. Jagatap and W. J. Meath, "On the competition between permanent dipole and virtual state two-photon excitation mechanisms, and two-photon optical excitation pathways, in molecular excitation," *Chemical Physics Letters,* vol. 258, pp. 293-300, 1996.

[12] B. N. Jagatap and W. J. Meath, "Contributions of permanent dipole moments to molecular multiphoton excitation cross sections," *Journal of the Optical Society of America B,* vol. 19, pp. 2673-2681, 2002/11/01 2002.

[13] M. Hippler, "Interference in two-photon rotational line strengths of diatomic molecules," *Molecular Physics,* vol. 97, pp. 105-116, 1999/07/20 1999.

[14] M. Drobizhev, F. Q. Meng, A. Rebane, Y. Stepanenko, E. Nickel, and C. W. Spangler, "Strong two-photon absorption in new asymmetrically substituted porphyrins: Interference between charge-transfer and intermediate-resonance pathways," *Journal of Physical Chemistry B,* vol. 110, pp. 9802-9814, May 2006.

[15] J. Kojima and Q.-V. Nguyen, "Entangled biphoton virtual-state spectroscopy of the A2Σ+–X2Π system of OH," *Chemical Physics Letters,* vol. 396, pp. 323-328, 2004.

[16] H.-B. Fei, B. M. Jost, S. Popescu, B. E. A. Saleh, and M. C. Teich, "Entanglement-Induced Two-Photon Transparency," *Physical Review Letters,* vol. 78, pp. 1679-1682, 1997.

[17] B. E. A. Saleh, B. M. Jost, H.-B. Fei, and M. C. Teich, "Entangled-Photon Virtual-State Spectroscopy," *Physical Review Letters,* vol. 80, pp. 3483-3486, 1998.

[18] J. L. a. D. R. Crosley, "LIFBASE: database and spectral simulation (version 1.5)," *SRI International Report MP 99-009,* vol. (SRI, 1999).

[19] J. Luque and D. R. Crosley, "Transition probabilities in the A 2Σ+−X 2Πi electronic system of OH," *The Journal of Chemical Physics,* vol. 109, pp. 439-448, 1998.

[20] R. P. Cageao, Y. L. Ha, Y. Jiang, M. F. Morgan, Y. L. Yung, and S. P. Sander, "Calculated hydroxyl A2∑ → X2Π (0, 0) band emission rate factors applicable to atmospheric spectroscopy," *Journal of Quantitative Spectroscopy and Radiative Transfer,* vol. 57, pp. 703-717, 5// 1997.

[21] A. Lofthus and P. H. Krupenie, "The spectrum of molecular nitrogen," *Journal of Physical and Chemical Reference Data,* vol. 6, pp. 113-307, 1977.

[22] H.-J. Werner, P. J. Knowles, G. Knizia, F. R. Manby, and M. Schütz, "Molpro: a general-purpose quantum chemistry program package," *Wiley Interdisciplinary Reviews: Computational Molecular Science,* vol. 2, pp. 242-253, 2012.

[23] T. H. Dunning, "Gaussian basis sets for use in correlated molecular calculations. I. The atoms boron through neon and hydrogen," *The Journal of Chemical Physics,* vol. 90, pp. 1007-1023, 1989.

[24] P.-F. Lu, L. Yan, Z.-Y. Yu, Y.-F. Gao, and T. Gao, "An Accurate Calculation of Potential Energy Curves and Transition Dipole Moment for Low-Lying Electronic States of CO," *Communications in Theoretical Physics,* vol. 59, p. 193, 2013.

[25] P. J. Knowles and H.-J. Werner, "An efficient method for the evaluation of coupling coefficients in configuration interaction calculations," *Chemical Physics Letters,* vol. 145, pp. 514-522, 4/22/ 1988.

[26] H. J. Werner, "Molecular properties from MCSCF-SCEP wave functions. II. Calculation of electronic transition moments," *The Journal of Chemical Physics,* vol. 80, pp. 5080-5084, 1984.

[27] H. J. Werner and P. J. Knowles, "A second order multiconfiguration SCF procedure with optimum convergence," *The Journal of Chemical Physics,* vol. 82, pp. 5053-5063, 1985.

[28] H. J. Werner and P. J. Knowles, "An efficient internally contracted multiconfiguration–reference configuration interaction method," *The Journal of Chemical Physics,* vol. 89, pp. 5803-5814, 1988.

[29] H. J. Werner and E. A. Reinsch, "The self-consistent electron pairs method for multiconfiguration reference state functions," *The Journal of Chemical Physics,* vol. 76, pp. 3144-3156, 1982.

Chapter 5

MOLPRO Methods

5.1 Introduction

The excited state to excited state transition dipole moment calculations were carried out using MOLPRO, an ab initio quantum chemistry package that focuses on electron correlation methods. MOLPRO is a high level program developed by Peter Knowles at Cardiff University and Hans-Joachim at Univeristat Stuttgart. It allows one to calculate excited state to excited state transition moments, which Gaussian, Spartan and other popular commercially available quantum chemistry programs did not allow users to do such high level calculations. The MOLPRO program package specializes in highly accurate calculations. The program utilizes several fast and efficient electron correlation methods and integral direct methods developed by Knowles, Werner and others [1]. The particular transition dipole moment calculations used in the diatomic virtual state theoretical study and presented in this thesis were calculated using Hartree Fock, CASSCF and MRCI methods [2-7].

As computational power has increased and more sophisticated software packages were commercialized ground state calculations became doable even for non-quantum chemists. However, electronic excited state calculations are more difficult to carry out than ground state calculations [8, 9]. Determining the properties of excited state quantities via excited state calculations is often more computationally demanding and

more theoretically involved. Yet, these calculations are necessary for understanding fundamental principles of absorption spectroscopy and these calculations are necessary for the work in this thesis comparing entangled photon absorption mechanisms through intermediate states and by virtue of permanent dipole coupling between states. This chapter will begin by detailing the process of calculating dipole moments followed by the derivation of the wave functions used to carry out these calculations. Background on the various methods used to complete this research will be provided, as well as a detailed outline of how the computational methods were carried out in MOLPRO.

5.2 Dipole Moments

5.2.1 Solving Schrodinger's Equation

The goal of quantum chemistry is to solve Schrodinger's equation. Schrodinger's equation for molecules can be written in the Born Oppenheimer Approximation as [10]:

$$\left[-\frac{1}{2}\sum_i \nabla_i^2 - \sum_{A,i}\frac{Z_A}{r_{Ai}} + \sum_{A>B}\frac{Z_A Z_B}{R_{AB}} + \sum\frac{1}{r_{ij}}\right]\Psi(\vec{r};\vec{R}) = E_{el}\Psi(\vec{r};\vec{R}) \qquad Equation\ 5.1$$

h(i) is the kinetic energy and potential energy for attraction to the nuclei.

$$h(i) = -\frac{1}{2}\nabla_i^2 - \sum_A \frac{Z_A}{r_{iA}} \qquad Equation\ 5.2$$

The nuclei attraction Hamiltonian for the ith electron, which can also be referred to as the one electron operator.

$$H_{el} = \sum_i h(i) + \sum_{i<j} v(i,j) + V_N \qquad Equation\ 5.3$$

The Coulomb term given by the two electron operator

$$v(i,j) = \frac{1}{r_{ij}} \qquad Equation\ 5.4$$

5.2.1.1 The Energy

The electron energy is given as:

$$E_{el} = \langle \Psi | H_{el} | \Psi \rangle \qquad Equation\ 5.5$$

The Hartree-Fock energy can be rewritten as:

$$E_{HF} = \sum_i \langle i|h|i\rangle + \frac{1}{2}[ii|jj] - [ij|ji] \qquad Equation\ 5.6$$

The integral which corresponds to the one-electron operator is

$$\langle i|h|i\rangle = \int d\vec{x}_1\, \chi_i{}^*(\vec{x}_1) h(\vec{r}_1) \chi_j(\vec{x}_1) \qquad Equation\ 5.7$$

$$[ij|kl] \qquad Equation\ 5.8$$

$$= \int d\vec{x}_1\ d\vec{x}_1 \chi_i(\vec{x}_1)\chi_j(\vec{x}_1)\frac{1}{r_{ij}}\chi_k(\vec{x}_2)\chi_l(\vec{x}_2)$$

Solving this eigenvalue problem allows chemists to reconstruct potential energy surfaces, determine the equilibrium geometry, and the vibrational frequency. While determining the wave functions $\Psi(\vec{r};\vec{R})$ allow one to calculate the dipole and multipole moments and the polarizability of molecules. As stated in Chapter 2, the classical electric dipole moment is given as [11]:

$$d_{cl} = \sum_i Q_i r_i \qquad Equation\ 5.9$$

The quantum mechanical operator becomes

$$\widehat{\mathcal{H}}' = -\boldsymbol{E} \cdot \widehat{\boldsymbol{d}} \qquad Equation\ 5.10$$

The electric dipole moment operator is defined as:

$$\widehat{\boldsymbol{d}} = \sum_i Q_i \boldsymbol{r}_i = \boldsymbol{i}\,\hat{d}_{\boldsymbol{x}} + \boldsymbol{j}\hat{d}_{\boldsymbol{y}} + \boldsymbol{k}\hat{d}_{\boldsymbol{z}} \qquad Equation\ 5.11$$

$$\hat{d}_{\boldsymbol{x}} = \sum_i Q_i x_i$$

$$\hat{d}_{\boldsymbol{y}} = \sum_i Q_i y_i$$

$$\hat{d}_{\boldsymbol{z}} = \sum_i Q_i z_i$$

We will now go through the method of calculating the molecular dipole from the wave functions of diatomic molecules. In order to solve for the transition moment, we take the expectation value of the dipole moment operator. The transition dipole moment is given as:

$$\int \psi_a^* \widehat{\boldsymbol{d}} \psi_b d\boldsymbol{r}^3 \qquad Equation\ 5.12$$

The permanent dipole moment is the dipole moment in the absence of an applied electric field.

$$\boldsymbol{d} = \int \psi^{(0)*}\, \widehat{\boldsymbol{d}} \psi^{(0)} d\tau \qquad Equation\ 5.13$$

In order to calculate these values, we must approximate the wave functions for the ground and excited states of the diatomic molecules to be studied N2, NO, and HF. Using such programs and theories that take into consideration electron correlation is

imperative since the transition moment is highly dependent on electron correlation. Geometry of the wave function also pays and important role since the transition moment is geometry dependent [12]. To approximate these wave functions variational methods are used [13].

5.2.2 Self-Consistent Field Methods

The solution to the Hartree-Fock method is found iteratively using the self-consistent field method.

$$f|\chi_a\rangle = \sum_{b=1}^{N} \varepsilon_{ba}|\chi_b\rangle \qquad Equation\ 5.14$$

$$\boldsymbol{f(i)} = -\frac{\mathbf{1}}{\mathbf{2}}\boldsymbol{\nabla^2} - \sum_{\boldsymbol{A=1}}^{\boldsymbol{M}} \frac{\boldsymbol{z_A}}{\boldsymbol{r_{iA}}} + \boldsymbol{v^{HF}(i)}, \qquad Equation\ 5.15$$

where v^{HF} is the field seen by the ith electron. It is dependent upon the spin orbitals of the other electrons [14].

1. Choose a set of orbitals.
2. Calculate the field seen by each electron.
3. Solve the eigenvalue problem for the eigenvectors.
4. Use the new orbitals to calculate the new field.
5. Continue the process until the orbitals used to generate the eigenfunctions are equivalent to the eigenfunctions.

5.2.2.1 Configuration Interaction

Unlike the Hartree-Fock method, which does not take into account electron correlation, configuration interaction (CI) methods do take this important physical constraint into consideration [2, 10]. The CI method is quite simple [15]. Instead of

minimizing just one determinant, the configuration interaction method is based on minimizing linear combinations of different slater determinants. Each determinant represents a different electron configuration. Other determinants are constructed by arranging electrons and placing them in different orbitals. Broadly speaking, one must diagonalize an N-electron Hamiltonian which is represented as a basis of N-electron functionals [10]. In this method, both the expansion coefficients and the orthonormal orbitals are optimized. The linear combination of the configuration state function is given by [10]:

$$\psi = \sum_I c_I \Phi_I = c_0\Phi_0 + c_1\Phi_1 + c_2\Phi_2 + \cdots, \qquad Equation\ 5.16$$

where $c_0\Phi_0$ is the Hartree-Fock/reference configuration and $c_1\Phi_1$is includes singles excitation and $c_2\Phi_2$ includes doubles excitation.

If all configuration state functions are given, then one has the exact wave function, as well as, the ground state and excited state energies [16]. However, completing a full CI treatment is not computationally feasible since it takes into account infinite excited state configurations [11]. Therefore the functions to be included in the linear combination are either chosen manually by the user, automatically by the program of choice or semi-automatically. The method chosen determines how much of the correlation energy is recovered [17].

Practical implementation of the CI method depends on two things: the assumption of a finite basis set and the restriction of the number of excited state electronic configurations [10]. One can assume a frozen core. If this is the case, there are no excited state promotions from the specified core electrons. One can also limit the number of promotions to singles, doubles or triples for example. Another simplification one can

make is only using configuration state functions that have the same symmetry as the state being approximated. For example, for the ground state H_2 configuration $^1\Sigma_g^+$, $\sigma_g\sigma_u$ configurations are not included because of their odd parity. Also, one does not necessarily have to use SCF molecular orbitals [11].

The CI method begins with a Hartree Fock wave function. The Hartree Fock term is used as the leading term in CI expansion wave function. The CI method does require a bit of artistry in choosing which configurations that contribute the most to particular wave functions. The CI method steps as outlined by Levin [11] are:

1. Select a suitable one-electron basis set.
2. Use the Hartree Fock Method to get one-electron orbitals ϕ_i in terms of the basis set chosen.
3. Create many electron Φ_i (configuration functions) using ϕ_i.
4. Generate a wavefuction ψ as a linear combination of the Φ_i.
5. Solve for the energy and the expansion coefficients.

5.2.2.2 Multiconfiguration Self-Consistent Field Method

The Multiconfiguration self-consistent field (MCSCF) method is used for generating reasonable reference states to be used in more complex MRCI calculations [11]. It is another variational method like the Hartree Fock method in which the CI energy of the wave function is minimized. This method is useful when a single Slater determinant is no longer suitable to describe the electronic structure of a particular molecule. This is another self-consistent field method that utilizes multiple configurations, but it limits the length of a CI calculation. These fields are composed of configuration state functions/determinants [11]. However, the MCSCF method which linear combinations of

the configuration state functions (multiple slater determinants) are used to obtain the lowest energy wave functions. MCSCF reduces to the Hartree Fock method when only one determinant is used for the expansion of a closed shell system [10]. The determinants used for calculations are generally selected by hand with this method. MCSCF is a method of limiting a CI expansion. For example the MCSCF wave function of a two electron system is:

$$|\Psi_{MCSCF}\rangle = \sum_{I} c_I |\Psi_I\rangle \qquad Equation\ 5.17$$

For H_2 the MCSCF method becomes

$$|\Psi_{MCSCF}\rangle = c_A|\psi_A\bar{\psi}_A\rangle + c_B|\psi_B\bar{\psi}_B\rangle \qquad Equation\ 5.18$$

the orthonormal orbitals are expanded

$$\psi_i = \sum_{\mu} C_{\mu i}\phi_\mu \quad i = A, B \qquad Equation\ 5.19$$

They are minimized under the constraints below

$$\langle\psi_A|\psi_A\rangle = \langle\psi_B|\psi_B\rangle = 1 \qquad \langle\psi_A|\psi_B\rangle = 0$$

And

$$c_A^2 + c_B^2 = 1$$

This method outlined above is used to determine the best expansion coefficient and an optimum form of the orbitals which is generally governed by the symmetry of the molecule [18]. For H_2 ψ_{MCSCF} is equivalent to the full CI wave function.

5.2.2.3 Complete Active Space Self-Consistent Field Method

The complete active space self-consistent field method is a subset of MCSCF methods. CASSCF fields are based on the number of electrons and the number of orbitals and the linear combination of the configuration state function includes all various

configurations of the electrons among the available orbitals [19]. The orbitals are divided into active and inactive orbitals. The inactive orbitals are not treated in the calculation. The electrons in the active orbitals are given as a linear combination of all configurations state functions distributed among all possible combinations of active states. All possible determinants are calculated within the chosen active space. The user only has to choose the active space and not the individual configurations. This results in better convergence because the program generates the configurations based on the active space chosen by the user. Once this is done, the MCSCF calculation proceeds as usual.

5.2.2.4 Multireference Configuration Interaction

Multireference CI includes excited state determinants in the linear combination which results in better correlation between the ground and excited states. Molpro utilizes efficient MRCI methods developed by Werner and Knowles. Their method is able to achieve this result because of direct CI procedures that are carried out in an internally contracted configuration basis, the utilization of non-orthogonal basis, which lead to simplifications and a method for recalculating coupling coefficients [20].

$$\Psi = \sum_{I} c^{I}\Psi_{I} + \sum_{S}\sum_{a} c_{a}^{S}\Psi_{S}^{a} + \sum_{P}\sum_{ab} C_{ab}^{P}\Psi_{P}^{ab} \qquad Equation\ 5.20$$

where Ψ_I, Ψ_S^a, Ψ_S^a are the internal, singly external and doubly external configurations and a, b are external orbitals and S and P core N-1 and N-2 states. The expansion coefficients are c^I, c_a^S, C_{ab}^P. To simplify things orbitals can be chosen such that all the states of interest may be found using the chosen reference wave functions.

The conventional MRCI method involves the explicit calculation of the

Hamiltonian matrix elements [12] and is an extensive calculation. Therefore, to cut down on the computational costs, it is important to only choose configurations of the wave functions that most greatly contribute to the solution. However, there is room for error if the wrong configurations are chosen. Direct CI methods allow one to avoid the risk of this error by calculating the eigenvectors iteratively without storing all the matrix elements of the Hamiltonian which allows one to use more configurations. Work by Meyer et al sought to develop an efficient direct CI method. The self-consistent electron pairs method calculates the vector $\boldsymbol{g} = (\boldsymbol{H} - E)\boldsymbol{c}$ iteratively which greatly reduces the number of logic operations [21]. Molpro utilizes more sophisticated forms of direct MRCI methods. This method uses SCEP methods similar to the ones described above. The difference lies in the calculations of the internal Coulomb and exchange operators. These operators are linearly combined with factors that have already been calculated instead of using fixed coefficients. These "new" internal coupling coefficients now only depend on a reference functions making them small and independent of the basis set. They are given as functions of the overlap and the transition matrix elements, thus allowing one to calculate these terms much more quickly and efficiently than other closed shell SCEP methods.

5.3 Aug-CC-PVTZ Basis sets

Basis sets are used define the space in which Schrodinger's equation is solved. Most physics problems are solved within a choice of an orthogonal basis. However, in the field of quantum chemistry, the basis sets are composed of the one-electron functions. These one-electron functions can be expanded in a linear combination of atomic orbitals [22]. These linear combinations can be used to build molecular orbitals. Common basis

sets are Slater type orbitals and Gaussian type orbitals. However, these orbitals are generally not ideal for correlated calculations. Dunning et al developed a basis set that incorporated correlated CISD wave functions, Aug-cc-pvtz [23]. The Aug stands for the augmentation of the angular moment component in the basis set. A diffuse function is added to each angular momentum. The cc stands for correlation consistent. Pv stands for polarized valence, and x stands for either double, triple or quadrupole, 5, 6, 7 etc.

5.4 Molpro Input Procedures

Now that we have discussed all the main computational methods that were utilized in this dissertation, we will now turn the discussion to focus on Molpro program procedures, the basic mechanics of the input files and the necessary components for calculating excited state to excited state dipole moments. Of the most popular quantum chemistry programs available such as Spartan, Gaussian and GAMESS, Molpro is probably the least user friendly. Although it does excel in performance and the level of features available. There is no user interface and programs are edited using unix editors such as Emacs and Vim and run via command line prompts. The run a calculation the command "molpro" is followed by the input file.

molpro input.com

molpro input.in

Since our calculations aren't generally computationally demanding, our version of Molpro only takes advantage of one of our processors. One can specify or overwrite the output files via the commands:

molpro –o input.out

molpro –s input.com

The default configurations for the program are given in the file **/usr/local/molpro/versionofmolpro/bin/molpro.rc**. The program defaults can be changed by creating a .molprorc file and saving it to the home directory.

There are three basic components to a MOLPRO output file and those components are: a geometry specification, a basis set and choice of computational method [1]. The input is not case sensitive. Below is a sample input file using the Hartree Fock method to generate electronic orbitals.

```
***NO Molecular Orbitals
```

The title of MOLPRO calculations are denoted with *** at the top of the input file.

```
memory,24,m
```

It is also necessary to state a memory allocation for the job. A memory allocation can be given as 24, m, which means 24 megawords. That is 183.11 megabytes.

```
r=2.1
geometry={
N;
O,N,r;}
```

The geometry is specified. This can be optimized in other programs such as Spartan, etc.

```
basis=cc-pvtz
```

The default basis set is spherical harmonics (5d, 7f, etc.). However, for these calculations as with most high level ab initio calculations a correlation consistent polarized basis set (cc-pvtz) by Dunning and co-workers was used.

```
Hf
```

Hf is the command to run a Hartree-Fock calculation.

5.4.1 Transition Dipole Moment Calculation

Hartree-Fock Calculations are a starting point for calculating excited state to excited state transition moments. It is at the Hartree-Fock level that one begins to define the orbital configurations for later calculations. The configuration information is given by the alpha configuration in the Hartree-Fock output file. The alpha orbitals are the singly occupied orbitals and beta orbitals are those that are doubly occupied.

Once the occupied subspaces are determined from the output file, we can rewrite the code to include the wavefunction information. The calculation is rewritten to include a defined wave function and orbital subspace.

```
***, CO Hartree-Fock Wave Functions
r=1.35

geometry={
 C;
 O,C,r;}

basis=cc-pvtz
```

The input for defining wave functions is given by the WF, *nelec, irrep, spin* command.

```
{hf
wf,14,1,0
occ,4,2,1
closed,2,,,
}
```

Nelec is the number of electrons in the molecule. Irrep is the number of the irreducible representation, for molecules with C_{2v} symmetry 1=A_1, 2=B_1, 3=B_2, 4=A_2. Spin is the total spin quantum number. The wave function input for HF is given by WF, 10, 1, 0, which denotes a 10 electron system occupying an A_1 state. The orbital

subspaces are defined as OCC, m_1, m_2, … , m_8; CORE, co_1, co_2, … , co_8; CLOSED, cl_1, cl_2, … , cl_8.

In HF calculations the occupied, OCC, states are those that contain electrons and occur in any of the configuration state functions. The number of occupied orbitals must add up to the number of valence electrons. If other configurations are chosen such that the number of valence electrons is not correct, an error message similar to this is likely to occur: NUMBER OF ORBITALS ON OCC CARD NOT CORRECT! NOC= 7 and NEL= 8. The m_l terms represent the number of occupied orbitals.

Unfortunately, molecular symmetry options are limited in Molpro. Therefore the $D_{\infty h}$ and $C_{\infty v}$ symmetry groups of the diatomic molecules studied were simplified to D_{2h} and C_{2v}. A_1 states represent Σ^+ states and A_2 states represent Σ^- states in molecules with C_{2v} symmetry. The degenerate states Δ and Π are represented by A1+A2 and B1+B2. These assignments will be used to correctly assess the actual physical excited state transitions studied.

Using C_{2v} symmetry, where m_1 equals the number of occupied A_1 states. CORE gives the number of core orbitals, and CLOSED gives the number of closed shell orbitals. For example, CLOSED, 2, 0, 0, 0 is interpreted for C_{2v} symmetry as two A_1 orbitals are closed and none of the B_1, B_2, or A_2 orbitals are closed.

Once the Hartree-Fock orbitals are generated they are used as a basis for the CASSCF orbitals, which are more complex.

```
***, CO Hartree-Fock Wave Functions
r=1.35

geometry={
 C;
```

```
 O,C,r;}

basis=cc-pvtz
{hf
 wf,14,1,0
 occ,4,2,1
 closed,2,,,
 }
```

The CASSCF orbitals are generated in a black box method in which the complete active space is determined by the user, while MOLPRO generates the configurations.

```
{casscf
 occ,5,2,2,0
 closed,2,,,
 }
```

The CASSCF orbitals are generated to include the potential excited state orbitals to be used in the MRCI calculations. The OCC, states are those that occur in any of the configuration state functions. The CLOSED electrons are not included in the complete active space calculation.

The MRCI calculations are generally the trickiest to calculate and require the rather skilled art of choosing a correct and viable active space. This is often the step where one is most likely to encounter an error message. Unfortunately, while the alpha orbital configuration from the Hartree Fock calculation is often a good place to start; the actual active space orbitals may have to be redefined during the CASSCF calculation. This requires a bit of work in terms of choosing good CASSCF orbitals for one's calculation. The calculation is explained below. Because we are trying to calculate the

transition moments between two-excited states, two MRCI command blocks are necessary.

```
***, CO Hartree-Fock Wave Functions
r=1.35

geometry={
 C;
 O,C,r;}

basis=cc-pvtz
```

Since the MRCI calculations involve excited states it is imperative that the states and the wave functions generated are saved. This is done below.

```
s1=7101.2
s2=7102.2
s3=7103.2


{hf
 wf,14,1,0
 occ,4,2,1
 closed,2,,,
 }

{casscf
 occ,5,2,2,0
 closed,2,,,
 }
```

The first state is generated with the MRCI call function. The same orbital specifications are used as those in the CASSCF calculations.

```
{mrci
 occ,5,2,2,0
```

```
 closed,2,,,
 wf,14,1,0;state,2
 save,s1
 }
```

The second state is generated with another MRCI call function.

```
{mrci
 occ,5,2,2,0
 closed,2,,,
 wf,14,3,0;state,1
 save,s2
 }
```

The transition moment calculations involve all of the discussed elements. However, we must include the transition command. The full code with explanations is given below. In these calculations the ground to excited state dipole is calculated then the excited to excited state dipole is calculated. The first excited state is generated and saved in the first command block, while the second is generated in the second.

```
***, Valence MRCI for CO transition dipole moments
 print,basis,orbitals

 r=1.35
```

The GEXPEC, dm is used to call transition dipole moment calculations in MOLPRO.

```
 gexpec,dm

 geometry={
 C;
 O,C,r;}

 basis=cc-pvtz
```

```
s1=7101.2
s2=7102.2
s3=7103.2

{hf
wf,14,1,0
occ,4,2,1
closed,2,,,
}

{casscf
occ,5,2,2,0
closed,2,,,
}

{mrci
occ,5,2,2,0
closed,2,,,
wf,14,1,0;state,2
save,s1
option,nstati=3
}

{mrci
occ,5,2,2,0
closed,2,,,
wf,14,3,0;state,1
save,s2
}
```

At the end of the calculation a table is created for the x, y, and z components of the transition dipoles. It calculates the one-electron expectation value of the dipole moment. This is the default dipole moment directive for MOLPRO.

```
ci;trans,s1,s2
table,trdmx,trdmy,trdmz
```

This concludes the MOLPRO transition moment calculation.

5.4.2 Errors and Troubleshooting

Now we will go through a few common errors and potential solutions. The first error is CI VECTOR FOR STATE 2 DOES NOT OVERLAP SUFFICIENTLY WITH REFERENCE VECTORS. It may help to increase NSTATI, e.g., use OPTION,NSTATI=3. There are two options in this case. One can either solve this issue by increasing the number of states in the previous CASSCF calculation. Or on the other hand, one can increase the number of NSTATI states. In this case, NSTATI is the number of states calculated in the internal CI. Often increasing NSTATI can solve the problem. Sometimes even after increasing NSTATI another error presents itself. This error convergence error is solved by adding NOCHECK to the MRCI command block. It bypasses MOLPRO's internal convergence checks.

Unfortunately, increasing NSTATI does not always work. At the point at which Molpro suggests increasing NSTATI to 21, it is time to increase the number of states in the CASSCF calculation. In most pre-built binary copies of Molpro the maximum number of NSTATI states allowed is 20. However, manually compiling MOLPRO and customizing the features to include more than 20 NSTATI states can eliminate this issue. The general issue in choosing one's active space is that it is difficult to find orbitals and states which yield smooth potentials for all geometries [24].

The output files for MOLPRO are quite lengthy. Yet, they are broken up into sections by the description of how the basis functions are set, the output from integral information along with symmetry information and the calculation methods that are included the input file. The results for the particular methods used for the calculation are then given. The results for each method are given in separate sections. For example, the alpha and beta electron configurations are given for Hartree-Fock methods, as well as, the lowest energy. Depending on the method detailed orbital information and the lowest energy are given. At the end of the file all of the converged energies are listed.

5.4.3 Molpro Help

The lab chose to implement MOLPRO on a Mac Pro computer. Specifications. The Mac proved to be much easier to operate in the unix system. Other IBM computers needed Cygwin in order to run unix based programs. The linux interface of the mac proved to be much more user-friendly. Assistance with trouble-shooting installation and calculation problems is provided by emailing Peter Knowles or Andy May at molpro@molpro.net. The User's Manual can be found at http://www.molpro.net/pipermail/molpro-user/. There is also a help thread that may contain useful advice for troubleshooting that molpro continues to maintain at http://www.molpro.net/info/2012.1/doc/manual/index.html?portal=user&choice=User%27s+manual

5.5 Distributed computing

Molpro has the capabilities to run on multiple processors using the distributed Global Arrays parallel toolkit package and pure MPI [1, 25]. The program can be compiled three ways: for serial execution only, for parallel execution of single

calculations and serial execution of identical tasks [1]. Generally, in distributed systems parts of calculations are run on different processors and messages are passed back and forth between the processors and the generated data is managed using libraries such as the parallel programming interface distributed data [26]. In our case, the distributed system is composed of the computer's multiple processors with each processor handling a particular part of a calculation, which has been divided up. The processors communicate via message passing in order to in our case complete a calculation.

5.6 MOLPRO Input Files

More detailed calculations were carried out in conjunction with our collaborators in the Zimmerman lab. While many of the computational techniques were new to our lab, we were able to implement these calculations. After our collaborators began the calculations with NO and N2, I was able to extend the work to CO and HF. While dipoles for particular intranuclear distances were found, our collaborators summed over various distances in order to create potential energy surfaces. This was particularly useful because while our estimates for the dipole moments seemed reasonable, at only one bond length it is difficult to determine if that calculation is comparable to dipole moments calculated at other distances. While it seems trivial to calculate the dipole moments over a range of bond lengths, it is not trivial. As stated early in Section 5.4.2, there can often be singularities that arise as the calculations move from the equilibrium bond length to shorter and longer bond lengths. These singularities arise from issues in choice of active space. Our collaborator began calculations at the equilibrium bond length, which was calculated in our lab and from that point either increased or decreased the bond length by a set interval until singularities arose. Once there was an issue of the

singularity, the active space was modified until the calculation was able to terminate without error. The calculation proceeded in this manner until the dipole moment was calculated over an entire potential energy surface. Below are the calculations for the single bond lengths.

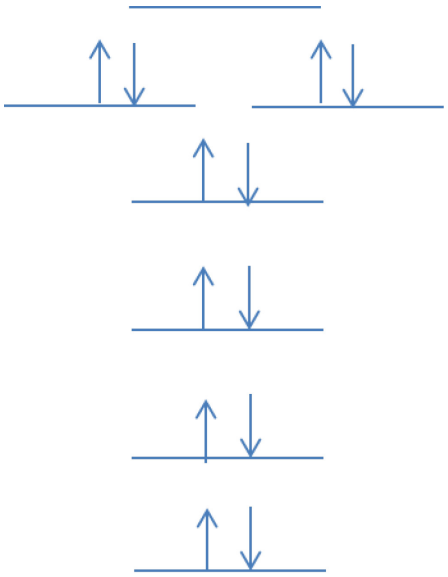

Figure 5.1. The molecular orbital diagram for CO.

```
***, Valence MRCI for CO transition dipole moments
 print,basis,orbitals
 r=1.35
 gexpec,dm

 geometry={
 C;
 O,C,r;}

 basis=cc-pvtz

 s1=7101.2
 s2=7102.2
```

```
 s3=7103.2

 {hf
 wf,14,1,0
 occ,4,2,1
 closed,2,,,
 }

 {casscf
 occ,5,2,2,0
 closed,2,,,
 }

 {mrci,nocheck
 occ,5,2,2,0
 closed,2,,,
 wf,14,1,0;state,2
 save,s1
 option,nstati=3
 }

 {mrci
 occ,5,2,2,0
 closed,2,,,
 wf,14,3,0;state,1
 save,s2
 }

ci;trans,s1,s2,d
table,trdmx,trdmy,trdmz
```

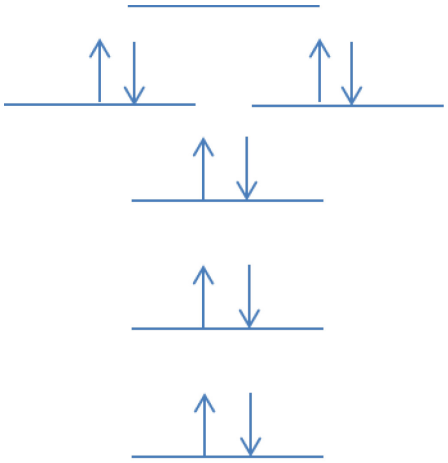

Figure 5.2. The molecular orbital diagram for HF.

```
***,Valence MRCI for NO transition dipole moments

memory,24,m

r=2.1

gexpec,dm


geometry={

N;

O,N,r;}


basis=cc-pvtz

s1=7101.2

s2=7102.2

s3=7103.2
```

```
{hf
wf,15,2,1 !15 e, B1 symm, doublet
occ,5,2,1,0 !A1 B1 B2 A2
closed,2,0,0,0
open,2.2
}

{casscf
occ,5,2,2,0
closed,2,,,}

{mrci;
occ,5,2,2,0
closed,2,,,
wf,15,2,1;state,2;
save,s1;}

{mrci;
occ,5,2,2,0
closed,2,,,
wf,15,4,1;state,1;
save,s2}
```

```
ci;trans,s1,s2,dm;

table,trdmx,trdmy,trdmz
```

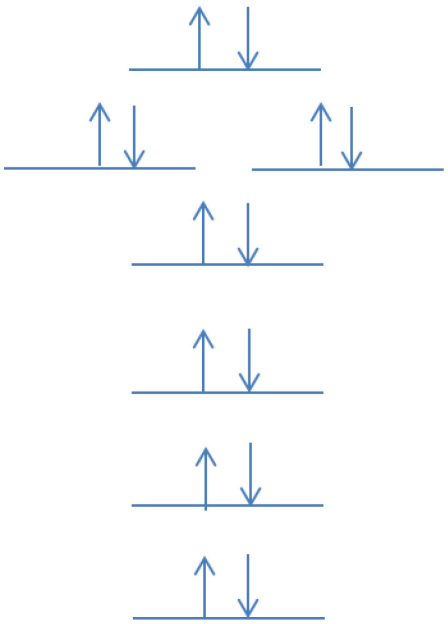

Figure 5.3. The molecular orbital diagram for N2.

```
***,Valence MRCI for N2 transition dipole moments

memory,24,m

r=2.1

geometry={

N;

N,N,r;}


basis=cc-pvtz
```

```
{hf
wf,14,1,0
occ,3,1,1,,2
}

Casscf

{multi;
wf,14,1,0;state,2;
wf,14,5,0;state,2;}
```

5.7 Molecular symmetry and Assignment of states

The first step in carrying out these calculations is the identification of the excited states. In order to do that some basic background on molecular symmetry, basic group theory and Mulliken symbols is necessary. Below the configuration terms are written out and given in terms of symmetry relations. Also given are term symbols that represent specific transitions. Unlike the large molecules studied experimentally, these diatomic molecules allow us to determine the exact states that are spanned in the two-photon absorption process.

$$\Lambda \equiv |M_L|$$

Λ	0	1	2	3	4
letter	Σ	Π	Δ	Φ	Γ

Configuration	Terms
σσ	$^1\Sigma^+$, $^3\Sigma^+$
σπ; σπ^3	$^1\Pi$, $^3\Pi$
ππ; ππ^3	$^1\Sigma^+$, $^3\Sigma^+$, $^1\Sigma^-$, $^3\Sigma^-$, $^1\Delta$, $^3\Delta$
πδ; π^{3}δ; πδ^3	$^1\Pi$, $^3\Pi$, $^1\Phi$, $^3\Phi$
σ	$^2\Sigma^+$,
σ^2; π^4; δ^4	$^1\Sigma^+$
π; π^3	$^2\Pi$
π^2	$^1\Sigma^+$, $^3\Sigma^-$, Δ
δ; δ^3	$^2\Delta$
δ^2	$^1\Sigma^+$, $^3\Sigma^-$, $^1\Gamma$

5.8 MOLPRO Installation Process

Step 1: As root, if there is an existing directory /usr/local/molpro move it to /usr/local/molpro-old

$ mv /usr/local/molpro /usr/local/molpro-old

Step 2: As root, Create new /usr/local/molpro and change owner to labadmin

$ mkdir /usr/local/molpro

$ chown labadmin /usr/local/molpro

Step 3: As a regular user, download the molpro binary distribution from the website (https://www.molpro.net/licensee/?portal=licensee) using the site username and site password used when registering. Click on downloads, go to the binary code section. Find the latest version and patch version for "Darwin" (not "Linux" or other platforms) and download this file. We downloaded, "Version 2012.1 for architecture Darwin/x86_64, standard code, serial (Patchlevel 2)"

Step 4: Once you have the file, move it into /usr/local/molpro directory and un-gzip the file:

$ mv /Users/labadmin/Downloads/molpro-serial-2012.1.2.Darwin_x86_64.sh.gz

/usr/local/molpro

$ cd /usr/local/molpro

$ gzip -d /Users/labadmin/Downloads/molpro-serial-2012.1.2.Darwin_x86_64.sh.gz

Step 5: Start "script" to log the output of the installer:

$ script

$ sh ./molpro-serial-2012.1.2.Darwin_x86_64.sh

"What bin directory"...enter

"What install directory"...enter

"Prompt for user name"... same as site username

"Prompt for password"... same as site password

$ exit # to leave script shell and close the log

Step 6: Set/update the path environment variable to molpro version:

First, find new molpro version name

$ ls /usr/local/molpro

This will show something like "/usr/local/molpro/molpros_2012_1_Darwin_x86_64_i8"

Add the molpro bin directory to the PATH variable by setting this in .bash_profile. Edit the file with

$ vi .bash_profile

export PATH="/usr/local/molpro/molpros_2012_1_Darwin_x86_64_i8/bin:$PATH"

There should only be one "export PATH" line at the end of the file. If there is no such line in the file, add it. For updating molpro, you should only need to change the version number in the path to match the new version.

Step 7: Done with installation, let's test it on one of the example files:

In a new terminal window, locate molpro with

$ which molpro

It should say "/usr/local/molpro/molpros_2012_1_Darwin_x86_64_i8/bin/molpro"

If it does not show this path, there is a problem.

Step 8: Create a temporary folder in the home directory and cd into it.

$ cd

$ mkdir tmp

$ cd tmp

$ cp /usr/local/molpro/molpros_2012_1_Darwin_x86_64_i8/examples/h2.com .

$ molpro h2.com

It should not show any output, but will create the files named h2.out, h2.pun, and h2.xml

5.9 Mathematica Program

Kojima and Nguyen developed the QEMASS Program [27]. This program was modified and utilized by our group to carry out our theoretical comparison of the entangled two-photon absorption cross-sections of diatomic molecules. The modifications to the program were based on previous work from our group. The entangled two-photon absorption cross-section was modified to include the contributions from virtual state absorption and absorption via permanent dipoles. Work by Kojima et al included transitions via vibrational and rotational transitions. In this work, we will only be focusing on electronic transitions of diatomic molecules. It must be noted that several constants and factors must be included in the calculation to ensure consistency.

```
Clear["Global`*"]
fj =;(*1.1 to .6 state from Andrew's calculations*)
ji =;(*1.1 to 1.2 state from Andrew's calculations*)
fi =;
ii =;
ff =;
Dfjji = fj * ji; (*Transition matrix elements from Radial Schrodinger Equation (Level 7.5) calculation with RKR*)
Dfiii = fi * ii; (**)
Dfffi = ff * fi; (**)
ϵi = 0; (* initial state *)
ϵj =; (* intermediate state *)
ϵf =; (* final state *)
κj = 22.46 × 10^-9; (* Literature value *)
κi = 6.161 × 10^-3; (* Literature value *)
κf =;
ωp = ϵf - ϵi; (* the two-photon pump frequency *)
Δp = ωp + ϵi - ϵj; (* energy mismatch *)

(*Modified Entangled Two-photon Absorption cross-section*)
(*Constants*)
c = 3 × 10^10;
τ = 711.6366 × 10^-9;
Δν = 1/(τ c);
δ = 1/π (Δν/2)/((ϵi + ωp) - ϵf)^2 + (Δν/2)^2);
h = 6.626 × 10^-34;
hbar = h/(2 π);
ϵ0 = 8.854 × 10^-12;
cc = 3 × 10^8;
ec = 1.602 × 10^-19;
Ae = 10^-6;
α = cc 10^-15;

(*Equations*)
σent[Te_] = ((1 - Exp[-I Δp Te α - (κj Te α)/2])/(Δp - I κj/2) Dfjji (3.336 × 10^-28)^2 + (1 - Exp[-I ωp Te α - (κi Te α)/2])/(ωp - I κi/2) Dfiii (3.336 × 10^-28)^2 + (1 - Exp[I ωp Te - (κf Te α)/2])/(-ωp - I κf/2) Dfffi (3.336 × 10^-28)^2);

σentSquared[Te_] = 1/(hbar^2 ϵ0^2 c^2 Ae (Te α)) (ωp/2)^2 δ σent[Te] * Conjugate[σent[Te]];
LogPlot[σentSquared[Te], {Te, 0, 1000}, PlotRange → All]
LogPlot[δrandSquared[Te], {Te, 0, 400}]
```

References:

[1] H.-J. Werner, P. J. Knowles, G. Knizia, F. R. Manby, and M. Schütz, "Molpro: a general-purpose quantum chemistry program package," *Wiley Interdisciplinary Reviews: Computational Molecular Science,* vol. 2, pp. 242-253, 2012.

[2] A. P. Scott and L. Radom, "Harmonic vibrational frequencies: An evaluation of Hartree-Fock, Moller-Plesset, quadratic configuration interaction, density functional theory, and semiempirical scale factors," *Journal of Physical Chemistry,* vol. 100, pp. 16502-16513, Oct 1996.

[3] J. C. Slater, "A Simplification of the Hartree-Fock Method," *Physical Review,* vol. 81, pp. 385-390, 02/01/ 1951.

[4] B. O. Roos, P. R. Taylor, and P. E. M. Siegbahn, "A COMPLETE ACTIVE SPACE SCF METHOD (CASSCF) USING A DENSITY-MATRIX FORMULATED SUPER-CI APPROACH," *Chemical Physics,* vol. 48, pp. 157-173, 1980.

[5] B. O. Roos, K. Andersson, M. P. Fulscher, P. A. Malmqvist, L. SerranoAndres, K. Pierloot, *et al.*, "Multiconfigurational perturbation theory: Applications in electronic spectroscopy," *Advances in Chemical Physics, Vol Xciii,* vol. 93, pp. 219-331, 1996.

[6] K. A. Peterson, D. E. Woon, and T. H. Dunning, "BENCHMARK CALCULATIONS WITH CORRELATED MOLECULAR WAVE-FUNCTIONS .4. THE CLASSICAL BARRIER HEIGHT OF THE H+H-2- H-2+H REACTION," *Journal of Chemical Physics,* vol. 100, pp. 7410-7415, May 1994.

[7] K. A. Peterson and T. H. Dunning, "The CO molecule: The role of basis set and correlation treatment in the calculation of molecular properties," *Theochem-Journal of Molecular Structure,* vol. 400, pp. 93-117, Jul 1997.

[8] L. González, D. Escudero, and L. Serrano-Andrés, "Progress and Challenges in the Calculation of Electronic Excited States," *ChemPhysChem,* vol. 13, pp. 28-51, 2012.

[9] P.-F. Lu, L. Yan, Z.-Y. Yu, Y.-F. Gao, and T. Gao, "An Accurate Calculation of Potential Energy Curves and Transition Dipole Moment for Low-Lying Electronic States of CO," *Communications in Theoretical Physics,* vol. 59, p. 193, 2013.

[10] A. Szabo and N. S. Ostlund, *Modern quantum chemistry: introduction to advanced electronic structure theory*. Mineola, N.Y.: Dover Publications, 1996.

[11] I. N. Levine, *Quantum chemistry*. Englewood Cliffs, N.J.: Prentice Hall, 1991.

[12] H. J. Werner, "Molecular properties from MCSCF-SCEP wave functions. II. Calculation of electronic transition moments," *The Journal of Chemical Physics,* vol. 80, pp. 5080-5084, 1984.

[13] D. J. Griffiths, *Introduction to quantum mechanics*. Upper Saddle River, NJ: Pearson Prentice Hall, 2004.

[14] C. D. Sherrill, "An Introduction to Hartree-Fock Molecular Orbital Theory," 2000.

[15] S. R. Langhoff and E. R. Davidson, "CONFIGURATION INTERACTION CALCULATIONS ON NITROGEN MOLECULE," *International Journal of Quantum Chemistry,* vol. 8, pp. 61-72, 1974.

[16] D. Walter, A. Venkatnathan, and E. A. Carter, "Local correlation in the virtual space in multireference singles and doubles configuration interaction," *Journal of Chemical Physics,* vol. 118, pp. 8127-8139, May 2003.

[17] C. David Sherrill and H. F. Schaefer Iii, "The Configuration Interaction Method: Advances in Highly Correlated Approaches," in *Advances in Quantum Chemistry*. vol. Volume 34, J. R. S. M. C. Z. Per-Olov Löwdin and B. Erkki, Eds., ed: Academic Press, 1999, pp. 143-269.

[18] C. Filippi and C. J. Umrigar, "Multiconfiguration wave functions for quantum Monte Carlo calculations of first-row diatomic molecules," *Journal of Chemical Physics,* vol. 105, pp. 213-226, Jul 1996.

[19] J. B. Foresman, A. Frisch, and I. Gaussian, *Exploring chemistry with electronic structure methods*. Pittsburgh, PA: Gaussian, Inc., 1996.

[20] P. J. Knowles and H.-J. Werner, "An efficient method for the evaluation of coupling coefficients in configuration interaction calculations," *Chemical Physics Letters,* vol. 145, pp. 514-522, 4/22/ 1988.

[21] C. E. Dykstra, H. F. Schaefer III, and W. Meyer, "A theory of self-consistent electron pairs. Computational methods and preliminary applications," *The Journal of Chemical Physics,* vol. 65, pp. 2740-2750, 1976.

[22] C. David Sherrill, "Basis Sets in Quantum Chemistry."

[23] J. Chen, Z. H. Levine, J. Y. Fan, and A. Migdall, "Efficient photon pair sources based on Silicon-on-Insulator microresonators," in *Conference on Quantum Communications and Quantum Imaging VIII*, San Diego, CA, 2010.

[24] H. J. Werner and P. J. Knowles, "An efficient internally contracted multiconfiguration–reference configuration interaction method," *The Journal of Chemical Physics,* vol. 89, pp. 5803-5814, 1988.

[25] A. J. Dobbyn, P. J. Knowles, and R. J. Harrison, "Parallel internally contracted multireference configuration interaction," *Journal of Computational Chemistry,* vol. 19, pp. 1215-1228, Aug 1998.

[26] J. Nieplocha, B. Palmer, V. Tipparaju, M. Krishnan, H. Trease, and E. Apra, "Advances, applications and performance of the Global Arrays shared memory programming toolkit," *International Journal of High Performance Computing Applications,* vol. 20, pp. 203-231, Sum 2006.

[27] J. Kojima and Q.-V. Nguyen, "Entangled biphoton virtual-state spectroscopy of the A2Σ+–X2Π system of OH," *Chemical Physics Letters,* vol. 396, pp. 323-328, 2004.

Chapter 6

Summary and Conclusion

I've conducted an in-depth look at the role molecular structure and absorption pathways play in the absorption of entangled photons. I began my dissertation work studying classical two-photon absorption properties. I followed this work by re-evaluating the ETPA cross-sections of different molecules with large TPA cross-sections and also evaluating the ETPA cross-sections of smaller organic molecules. Finally, I conclude this work with a study of diatomic ETPA cross-sections. This body of work only scratches the surface entangled two-photon interactions. However, I hope I've illuminated the importance of virtual states in these interactions. A hypothesis was made based on experimental and theoretical data that not only do virtual states play an important role in entangled two-photon absorption as others have also suggested, but that having a large enough virtual state contribution to overcome the interference of the dipolar contribution may in fact be to the key to observing ETPA in molecules of interest.

6.1 Contributions to the Field

At the basis of entangled two-photon absorption is the theory of classical two-photon absorption. In order to understand these non-classical effects it is important to also have a foundational understanding of classical two-photon absorption. In order to identify new molecular candidates for ETPA, it is necessary to determine first whether molecules undergo two-photon interactions. As such, I began my dissertation work

studying novel molecules with measurable two-photon absorption properties. I worked on and studied different classes of silver nanoclusters and DCDHF fluorophores. I present data on calculated the TPA cross-sections of the silver nanoclusters and also present data highlighting issues of instability in these molecules. Because of these stability issues the DNA-templated nanoclusters were not good candidates for studying ETPA and were not included in future studies using entangled photons.

I also studied and calculated the two-photon absorption cross-sections of DCDHF single molecule fluorophores. Because of their development for single molecule applications, DCDHF fluorophores made very good candidates for studying ETPA. There are particularly exciting potential applications in using these molecules in the development of ETPA microscopy techniques. Such applications take advantage of the estimated absorption enhancements of ETPA due to the correlations of the fields and the low experimental intensities of the entangled fields. These molecules also exhibited moderate TPA absorption cross-sections which made them good candidates to pursue future ETPA studies.

While the ETPA work has been ongoing in our lab, I have sought to ensure a more thorough and sound investigation of these sensitive interactions. Realizing the importance of correct characterization of the fields, I redesigned the optical table to better incorporate visibility and imaging measurements and to ease alignment procedures. I conducted many studies to ensure background was minimized and characterized.

I re-measured and re-calculated the ETPA the ETPA σ_E of several large conjugated systems. This work built upon earlier work in differentiating absorption mechanisms in different molecules. A new entangled two-photon absorption cross-

section equation, analogous to the classical TPA equation that accounts for the material properties of the material systems studied, was developed. It was suggested that accounting for the new terms in the cross-section equation that one may be able to explain the differentiation of the observed experimental results based on interference of the transition moment components.

While much of the work on entangled two-photon interactions with molecules has been on large conjugated systems, these systems often have very complex molecular structures and interactions. Because of their large cross-sections, they may make great candidates for the easy experimental realization at IR wavelenths without the use of vacuum tubes. However, these molecules are not useful in helping determine and decipher exact interactions. Because of this I searched for smaller, more widely studied and fluorescent molecules to use in future studies. I decided to study a stilbene derivative, coumarin 30, and a few of the DCDHF fluorophores. The ETPA data for these molecules is presented. There does seem to be differentiation in the absorption properties of the different molecules based on the varying slopes in the ETPA absorption graphs. These factors were explored in terms of the interference of absorption pathways. However, it is difficult to draw conclusive conclusions from this data. I'm sure that going smaller is the key to experimentally determining the exact interactions of these light matter interactions. Future work includes studies on corolene and naphthalene.

In order to test this hypothesis of interfering pathways, I suggested comparing the theoretical cross-sections of heteronuclear and homonuclear diatomic molecules. While others have looked at the theoretical cross-sections of hydrogen and OH, they used equations that did not take the two-photon absorption pathways into consideration. What

was supposed to a trivial task of looking up and organizing transition moment matrix elements developed into a computational electronic structure enterprise. As such, I utilized Molpro to calculate excited state to excited state transition dipole moments in molecules. Using calculated values, I was able to calculate and compare diatomics. This theoretical work raises further issues for future work. Hopefully, this work will provide keys for molecular design and for developing rules to determine whether molecules absorb entangled photons or not. This knowledge is particularly useful as experimentalists hope to harness non-classical fields.

6.2 Future Work

Future work includes exploring the many potential applications for entangled two-photon absorption. However before this power and the unique spectral and temporal resolution that these non-classical fields hope to offer can be harnessed for these applications, we need a greater understanding of the mechanisms, which drive these processes. That is what this dissertation has sought to do. Hopefully, the work completed in this dissertation on these interactions will provide small steps toward better understanding these interactions. Once these interactions are t, the potential applications are endless. In fact, entangled photons may provide a key into unlocking key insights into electronic molecular structure.

Shaul Mukamel has been on the forefront of theorizing the possible experiments exploring electronic structure, especially in the areas of non-classical 2D interactions. Using entangled photons to probe complex systems may provide key insights into excitonic interactions. His proposed theoretical use of 2-D spectroscopic experiments with entangled photons will utilize the spatial and temporal correlations of entangled

fields as a method of molecular characterization. We hope to use our research as a step towards utilizing quantum fields to gain more information about energy and charge transfer in molecules.

The Goodson group will also continue to work on observing fluorescence from ETPA, which will be the first steps towards the realization of non-classical pump probe spectroscopy and non-classical microscopy. Theoretical work exploring the ETPA cross-sections in larger molecules will also continue. The group will continue to lead the field in studying these interactions from basic research to applications.

Appendices

Appendix A: Instrument Specifications

SENSOR SOLUTIONS

DATASHEET

SPCM-AQRH

Single Photon Counting Module

Single Photon Counting APD - RoHS Compliant

Overview

The new RoHS compliant SPCM-AQRH is a self-contained module that detects single photons of light over the 400 nm to 1060 nm wavelength range - a range and sensitivity that often outperforms a photomultiplier tube.

The SPCM-AQRH uses a unique silicon avalanche photodiode (APD) with a circular active area that achieves a peak photon detection efficiency of more than 65% at 650 nm over a 180 µm diameter. The photodiode is both thermoelectrically cooled and temperature controlled, ensuring stabilized performance despite ambient temperature changes. Circuit improvements have reduced the overall power consumption.

Count speeds exceeding 20 million counts per second (Mc/s) are achieved by the SPCM-AQRH-1X module (> 30 million counts per second on some models). There is a "dead time" of 35 ns between pulses but other values can be set at the factory.

As each photon is detected, a TTL pulse of 2.5 Volts (minimum) high in a 50 load and 15 ns wide is output at the rear BNC connector. To avoid a degradation of the module linearity and stability, a case temperature between 5°C and 40°C should be maintained.

This series of photon counting modules are designed and built to be fully compliant with the European Union Directive 2002/95EEC – Restriction of the use of certain Hazardous Substances in Electrical and Electronic equipment (RoHS).

Features and Benefits

- EU RoHS compliant
- Peak photon detection efficiency at 650 nm: 65% typical
- Active area: 180 µm
- User friendly
- Gated output
- Single +5 V supply

Applications

- LIDAR
- Photon correlation spectroscopy
- Astronomical observation
- Optical range finding
- Adaptive optics
- Ultra sensitive fluorescence
- Particle sizing

www.optoelectronics.perkinelmer.com

PerkinElmer® precisely.

$$ACTUAL\,COUNTRATE_{Photons} = \frac{(OUTPUT\ ModuleCountRate \times CORRECTIONFACTOR\ @\ the\ Module\ CountRate) - DARK\ COUNT\ Module}{PHOTON\ DETECTION\ EFFICIENCY\ Module}$$

The theoretical value, at low count rate, of the Correction Factor follows this equation:

$$Correction\ Factor = \frac{1}{1 - (t_d \times C_R)}$$

Where: t_d = Module Dead Time

C_R = Output Count Rate

The deviation from an ideal linear system is another way of looking at the saturation effect. The following equations show how to calculate this departure from the linearity:

$$LINEARITY = \left[\frac{OUTPUT\ ModuleCountRate}{(PHOTONS\ Actual\ Count\ Rate \times PHOTON\ DETECTION\ EFFICIENCY\ Module) + DARK\ COUNT\ Module}\right]^{-1}$$

$$= \left[\frac{1}{Correction\ Factor}\right]^{-1}$$

Table 1. Specifications of SPCM-AQRH-1X , @ 22 °C, all models, unless otherwise indicated.

Parameter		Min	Typ	Max	Unit
Supply current			0.3	1.2	A
Supply voltage [1]		4.75	5.0	5.25	V
Power cable total resistance			0.1	0.2	Ω
Case operating temperature [1, 3]		5		40	°C
Active area (diameter) at minimum Pd		170	180		µm
Photon detection efficiency (Pd) at:	400nm	2	5		%
	650nm	50	65		%
	830nm	35	45		%
	1060nm	1	2		%
Pd variation at constant case temperature (2hrs at 25 °C)			± 1	± 3	%
Pd variation from 5 °C to 40 °C			± 4	± 10	%
Dark Count [4, 5, 6]	SPCM-AQRH-10			1500	Counts /second
	SPCM-AQRH-11			1000	
	SPCM-AQRH-12			500	
	SPCM-AQRH-13			250	
	SPCM-AQRH-14			100	
	SPCM-AQRH-15			50	
	SPCM-AQRH-16			25	
Average dark count variation at constant case temperature (6 hrs at 25 °C) [4, 5, 6]					
	SPCM-AQRH-10, 11, 12, 13			± 10	%
	SPCM-AQRH-14, 15, 16			± 1	σ

Parameter	Min	Typ	Max	Unit
Average dark count variation at 5 °C to 40 °C case temperature for [4, 5, 6] SPCM-AQRH-10, 11, 12, 13 SPCM-AQRH-14, 15, 16			 ± 20 ± 2	 % σ
Single photon timing resolution		Contact factory for availability		ps
Dead time (count rate below 5M/c)		32	40	ns
Output count rate before saturation[8]	20	29		Mc/s
Linearity correction factor [7] at 200 Kc/s 1 Mc/s 5 Mc/s 10 Mc/s 20 Mc/s 25 Mc/s		1 1.03 1.2 1.48 2.8 4.5		
Afterpulsing probability		0.5		%
Setting time following power up (1% stability) at 1 Mc/s and 25 °C		15	20	s
Threshold setting required on counter for digital output pulse (terminate in 50□)		1.0		V
Output pulse width [9]		15		ns
Gating turn on/off (50□ output) Disable = TTL low (<0.8V) Enable = TTL high (>2.0V)		 26 52	 32 61	ns
Gating threshold voltage (at V supply = 5V) Low level (sink current >90mA) High level (sink current >30mA)	 0 2.0		 0.4 5.25	V

Refer to Operating Instructions for noted items

Table 2. Absolute Maximum Ratings

Supply voltage [1]	5.5 V
Maximum count rate	Maximum count rate can be sustained if case temperature is maintained within limit specified limits.
Peak light intensity	10^{4} photons per pulse and pulse width < 1ns
Case temperature [3]	-20 °C/+70 °C storage, +5 °C /+40 °C operating (+50°C at reduced count rates).

Table 3. SPCM Ordering Guide

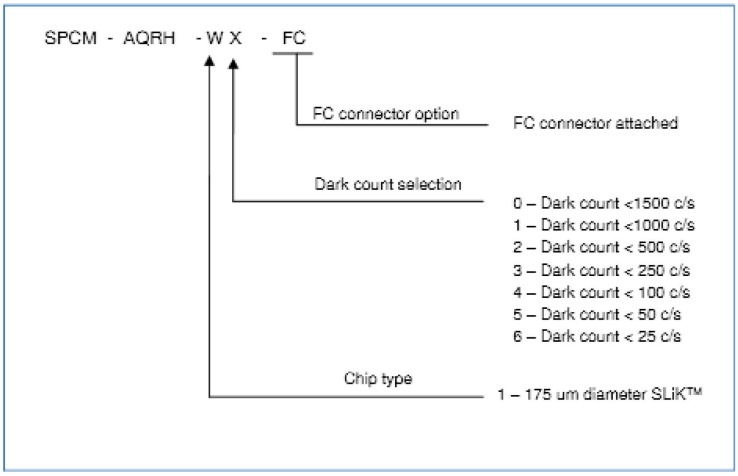

Table 4. Fiber Ordering Guide

Part Number	Fiber Type	Connector Type	Diameter			Numerical Aperature
			Core	Cladding	Outer	
SPCM-QC4	Multimode	FC / Bare	62.5 µm	125 µm	2.5 mm	0.27
SPCM-QC6	Multimode	FC / Bare	100 µm	140 µm	2.5 mm	0.29
SPCM-QC8	As SPCM-QC6 but 905 SMA on free end, 100 microns core fiber					
SPCM-QC9	As SPCM-QC6 but FC connector on free end, 100 microns core fiber					

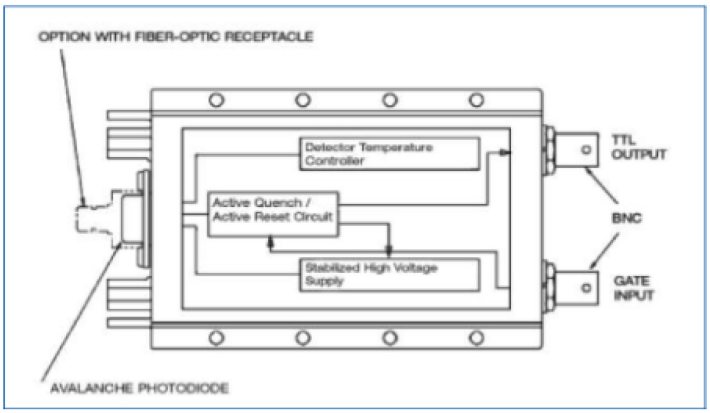

Figure 1.
Module Block Diagram

OUTPUT CONNECTOR
The digital OUTPUT pulse (BNC connector, TTL levels, >2.0v) should be terminated into a 50 ohm load to avoid distortion and ringing. A 1.0 volt triggering level is recommended on counters and oscilloscopes to avoid triggering on noise. Note that TTL stands for Transistor Transistor Logic.

GATE CONNECTOR
The GATE input (BNC connector) impedance is 50 ohms and internally connected to the +5 volt supply through a pull-up resistor (standard module versions). It can be driven by standard TTL level signals.

POWER CONNECTOR
The +5volt power connector is a standard barrel connector (2.5mm I.D., 5.5mm O.D.) with an 18 AWG cable. The center stripe corresponds to the center of the barrel and connects to the positive terminal of the 5 volt supply. Reversal of the wires may damage the module.

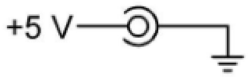

Figure 2.
Electrical Connections

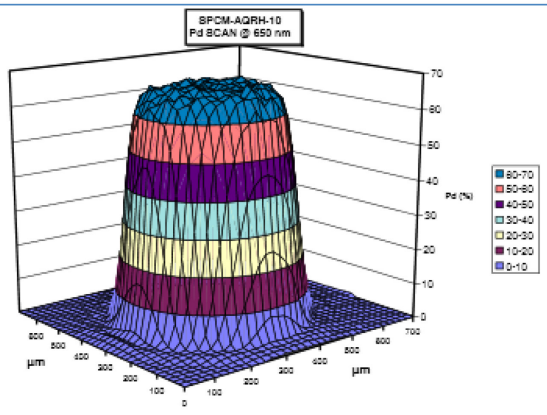

Figure 3.
Typical Pd Scan

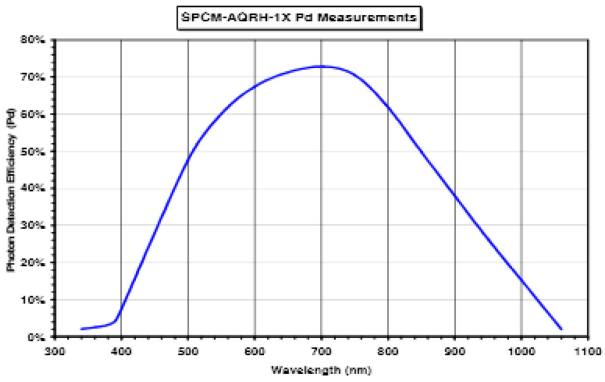

Figure 4.
Typical Photon Detection Efficiency (Pd) vs. Wavelength

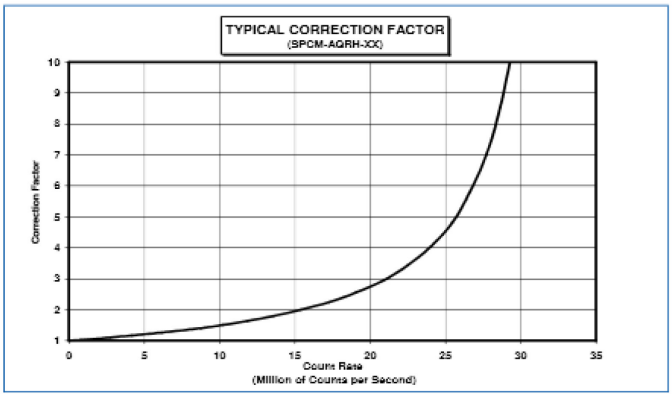

Figure 5.
Typical Correction Factor

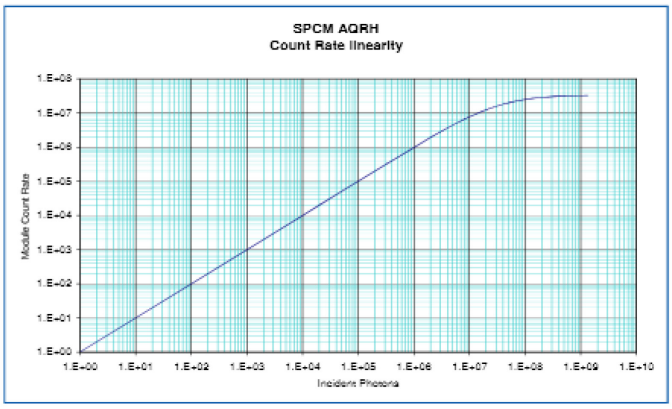

Figure 6.
Count Rate Linearity

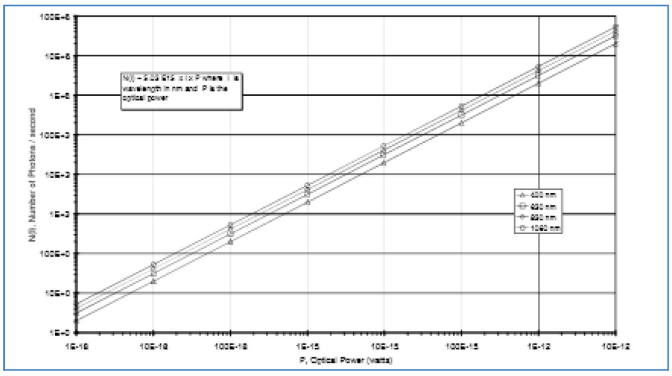

Figure 7.
Optical Power vs. Number of Photons

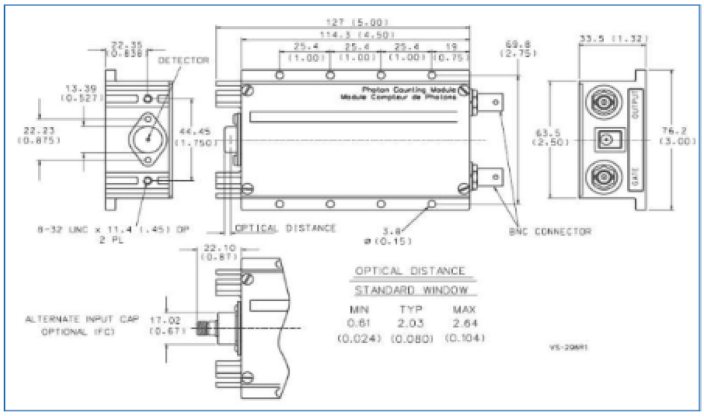

Figure 8.
Dimensional Outline

Your Partner of Choice

With a broad customer base in all major markets, built on ninety years of solid trust and cooperation with our customers, PerkinElmer is recognized as a reliable partner that delivers high quantity, customized, and superior "one-stop" solutions. Our products – from single photocells to complex x-ray inspection systems - meet the highest quality and environmental standards.
Our worldwide Centers of Excellence, along with our Customer and Technical Support teams, always work with you to find the best solutions for your specific needs.

PerkinElmer Optoelectronics

PerkinElmer Optoelectronics is a global technology leader providing market-driven, integrated solutions for a wide range of applications which leverage our lighting, sensors, and imaging expertise. Our technologies, services and support are enhancing our customers' productivity, optimizing performance, and accelerating time to market.

So contact us and put PerkinElmer's expertise to work in your demanding applications. We will show how our innovations will help you deliver the perfect product.

Worldwide Headquarters
PerkinElmer Optoelectronics
44370 Christy Street
Fremont, CA 94538-3180
Telephone: +1 510-979-6500
Toll free: (North America) +1 800-775-OPTO (6786)
Fax: +1 510-687-5190
Email: opto@perkinelmer.com
www.optoelectronics.perkinelmer.com

European Headquarters
PerkinElmer Optoelectronics
Wenzel-Jaksch-Str. 31
65199 Wiesbaden, Germany
Telephone: (+49) 611-492-247
Fax: (+49) 611-492-170
Email: opto.Europe@perkinelmer.com

Asia Headquarters
PerkinElmer Optoelectronics
47 Ayer Rajah Crescent #06-14
Singapore 139947
Telephone: (+65) 6775-2022
Fax: (+65) 6775-1008
Email: opto.Asia@perkinelmer.com

PerkinElmer® precisely.

USER'S GUIDE

Large-Area Photoreceivers

Models 2031, 2032, 2033, & 2034

NEW FOCUS®
Smart Optics for Networks™

5215 Hellyer Ave. • San Jose, CA 95138-1001 • USA
phone: (408) 284–6808 • fax: (408) 284–4824
e-mail: contact@newfocus.com • www.newfocus.com

Operation

Introduction

The Model 203X is a general-purpose, battery-powered photoreceiver with a large-area photodetector. There are four versions of the Model 203X receiver, each based on a different photodetector:

Model	Wavelength	Type	Diam.
2031	400–1070 nm	silicon	8 mm
2032	190–1100 nm	UV-enhanced silicon	5.8 mm
2033	800–1750 nm	germanium	5 mm
2034	800–2200 nm	extended-λ InGaAs	1 mm

Note: *Complete specifications for the Model 203X large-area photoreceivers begin on page 23.*

The large area of the photodetector makes it easy to couple light from a variety of sources (including diode lasers, broadband sources, and light from optical fibers) onto the detector without requiring precise optical alignment or focusing. Figures 1 and 2 on the following page show the typical responsivity curves for the different detectors.

Figure 1: Typical responsivities of the Model 2031 & 2033 photodiodes

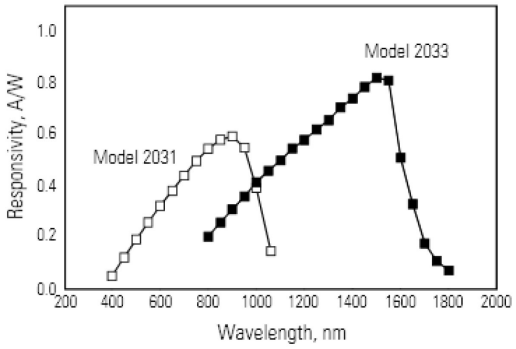

Figure 2: Typical responsivities of the Model 2032 & 2034 photodiodes

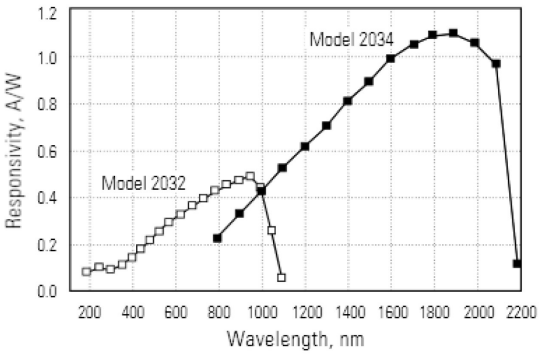

Note: *For more information on frequency response and noise, see page 13.*

The photoreceiver's slim casing, shown on the next page, makes it easy to position it in a set-up between closely spaced optics. The switches and BNC output connector are located on top of the receiver for easy access.

Figure 3: The Model 203X casing

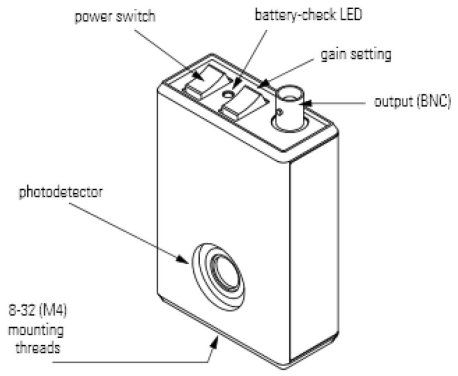

Note: *A full mechanical diagram of the Model 203X casing is available on page 23.*

Using the Photoreceiver

1. **Check the battery voltage.** The Model 203X is powered by a single 9-volt alkaline battery. To check the battery condition, push the red power switch to the BATT CHK position. If the green LED lights up, the battery is in good condition; if the LED does not light, the battery needs to be replaced (see page 8).
2. **Mount the photoreceiver.** Use the 8-32 thread (M4 for metric versions) on the bottom of the casing to mount the photoreceiver to a post or pedestal.

CAUTION! *The threading is seated in a non-conductive plastic pad to reduce the electrical noise associated with ground loops. Be careful not to over-tighten when attaching the casing to a post or pedestal, or the threaded insert can strip out of the plastic pad.*

3. **Connect the receiver output.** Connect your voltmeter, oscilloscope, or other instrument to the **Output** BNC connector on top of the receiver.

4. **Turn the power switch to "on."** The output voltage should register on your scope or instrument.
5. **Align an optical beam onto the detector.** Be careful to keep the optical power under the maximum optical power of 10 mW to avoid damaging the photodetector.
6. **Adjust the gain.** Use the black switch on top of the receiver to set the gain to low, medium, or high. The bandwidths vary with the gain setting (the label on the front of the photoreceiver indicates the gain and bandwidth values).
7. **Turn the receiver off.** When you are finished with the receiver, return the power switch to the "off" position.

Checking the Battery

The Model 203X is powered by a single, standard 9-volt alkaline battery. Under normal operating conditions with low light levels and a high impedance load attached to the BNC connector, the photoreceiver draws about 1 mA from the battery, and the battery lifetime is approximately 500 hours.

To check the condition of the battery, push the red power switch to the BATT CHK position. If the green LED lights up, the battery is in good condition.

When the battery voltage falls below about 6.5 volts, the green LED will not light up, and the battery should be replaced.

Replacing the Battery

1. Turn the red power switch to "off" to prevent damage to the receiver.
2. Remove the screw on the back of the photoreceiver casing and remove the back cover.

3. Unplug the old battery by rotating it away from the circuit board about the snap-on terminal contacts
4. Install a new 9-volt alkaline battery.
5. Reinstall the back cover and screw.
6. Test the new battery's status by pushing the power switch to the BATT CHK position.

Appendix B: Derivation of Modified ETPA Cross-Section

The modified entangled two-photon absorption equation is based on a three level system. Like classical two-photon absorption the derivation is based on second order perturbation theory. The more complex nature of the entangled two-photon fields does add complexity to the calculation.

Figure A1. This is a schematic of the three level system that is covered in this derivation with the transition of interest being from the ground to some final excited state.

To start, we begin with Bebb and Gold's treatment of multiphoton absorption [1]. The probability of a transition is

$$W_{f,g}(t) = |\langle f|U_I(t)|g\rangle|^2$$

The time evolution operator is

$$U_I(t) = 1 + (i\hbar)^{-1}\int^t H_I'(t')U_I(t')dt'$$

$$U_I(t) = 1 + \sum_{n=1}^{\infty} U_I^{(n)}(t)$$

Depending on the number of interactions, the time evolution operator can be written as

$$U_I^{(n)}(t) = (i\hbar)^{-n} \int_0^t dt_n \int^{t_n} dt_{n-1} \dots \int^{t_2} dt_1 \, H_I'(t_n) H_I'(t_{n-1}) \dots H_I'(t_1)$$

$$\left\langle f \left| U_I^{(N)}(t) \right| g \right\rangle = (i\hbar)^{-N} \int_0^t d^N t \, \langle f | H_I'(t_N) H_I'(t_{N-1}) \dots H_I'(t_1) | g \rangle$$

In our case, for two-photon absorption this becomes:

$$b_{f,g} = \left\langle f \left| U_I^{(2)}(t) \right| g \right\rangle = (i\hbar)^{-2} \int_0^t dt_2 \langle f | H_I'(t_2) | j \rangle \langle j | H_I'(t_1) | g \rangle$$

The probability of transition is $W_{f,g}(t) = \left| \left\langle f \left| U_I^{(2)}(t) \right| g \right\rangle \right|^2$. Utilizing the dipole approximation, our interaction Hamiltonian is

$$H_{int} = -\mu \cdot E\left(\vec{R}\right)$$

Using the procedure by Meath and Power [2] outlining the importance of permanent moments, the matrix elements for absorption of two photons from same mode can be written in similar fashion as the matrix elements above as the product of two single photon transitions that occur via intermediate states.

$$M_{f \leftarrow i}^2 = \frac{\left\langle f \left| H^{int} \right| I \right\rangle \left\langle I \left| H^{int} \right| g \right\rangle}{E_i - E_I}$$

where the energy level differences can be defined as:

$$E_2 - E_1 = E_{21} \cong 2\hbar\omega$$

for two photons

$$E_g = E_1 + 2\hbar\omega$$

$$E_I = E_p + \hbar\omega$$

$$E_f = E_2$$

$$M^2_{f\leftarrow i} = i^2\left(\frac{2\pi\hbar\omega_\lambda}{V}\right)[N(N-1)]^{1/2}\sum_p \frac{\langle 2|\vec{\mu}|p\rangle\langle p|\vec{\mu}|1\rangle}{E_1 + 2\hbar\omega - (E_p + \hbar\omega)}$$

$$= -\left(\frac{2\pi\hbar\omega_\lambda}{V}\right)[N(N-1)]^{1/2}\sum_p \frac{\vec{\mu}_{2p}\vec{\mu}_{p1}}{E_1 - E_p + \hbar\omega}$$

$$= -\left(\frac{2\pi\hbar\omega_\lambda}{V}\right)[N(N-1)]^{1/2}\sum_p \frac{\vec{\mu}_{2p}\vec{\mu}_{p1}}{\hbar\omega - E_{p1}}$$

We then sum over the intermediate states, p.

$$M^2_{f\leftarrow i} = \left(\frac{2\pi\hbar\omega_\lambda}{V}\right)[N(N-1)]^{\frac{1}{2}}\left(\frac{(\vec{\mu}_{22} - \vec{\mu}_{11})\vec{\mu}_{21}}{\hbar\omega}\right) - \sum_{p\neq 1,2}\frac{\vec{\mu}_{2p}\vec{\mu}_{p1}}{\hbar\omega - E_{p1}}$$

The modified entangled two-photon absorption cross-section will include similar matrix elements in that we will take into account not only the intermediate state transition moments, but the permanent moments, as well. However, it must be noted that the matrix elements above assume that both photons are in the same mode. This is not the case for type-II SPDC, where the signal and idler photons are in different modes. When the photons are in different modes the matrix elements become [2]:

$$M^2_{f\leftarrow i} = \frac{-2\pi\hbar}{V}(\omega\omega')^{1/2}(NN')^{1/2}\left(\sum_n \frac{\vec{\mu}_{2n}\cdot\hat{e}'\vec{\mu}_{n1}\cdot\hat{e}}{\hbar\omega - E_{n1}} + \sum_n \frac{\vec{\mu}_{2n}\cdot\hat{e}\vec{\mu}_{n1}\cdot\hat{e}'}{\hbar\omega' - E_{n1}}\right)$$

$$= \frac{-2\pi\hbar}{V}(\omega\omega')^{1/2}(NN')^{1/2}\left(\frac{\vec{\mu}_{21}\cdot\hat{e}'\vec{\mu}_{11}\cdot\hat{e}}{\hbar\omega - E_{n1}} + \frac{\vec{\mu}_{21}\cdot\hat{e}\vec{\mu}_{11}\cdot\hat{e}'}{\hbar\omega' - E_{n1}} + \frac{\vec{\mu}_{22}\cdot\hat{e}'\vec{\mu}_{21}\cdot\hat{e}}{\hbar\omega - E_{n1}}\right.$$

$$\left. + \frac{\vec{\mu}_{22}\cdot\hat{e}\vec{\mu}_{21}\cdot\hat{e}'}{\hbar\omega' - E_{n1}} + \sum_{n\neq 1,2}\frac{\vec{\mu}_{2n}\cdot\hat{e}'\vec{\mu}_{n1}\cdot\hat{e}}{\hbar\omega - E_{n1}} + \sum_{n}\frac{\vec{\mu}_{2n}\cdot\hat{e}\vec{\mu}_{n1}\cdot\hat{e}'}{\hbar\omega' - E_{n1}}\right)$$

For simplification, we assume that the signal acts first and then the idler acts on the system. In actuality, we need to consider all contributions as in the example above to have a complete cross-sectional equation that takes into account all interactions. This derivation provides an overview of the steps taken to produce a modified entangled two-photon absorption cross-section. This is based on work done by Richter et al [3] with portions related to the SPDC field from Keller [4]. Similar to the examples above, we begin looking at the interactions in the molecule by focusing on the matrix elements. We begin with the transition probability in terms of the interaction Hamiltonian.

$$b_{f,g}(t_1) = (i\hbar)^{-2}\int_{t_0}^{t} dt_2 \langle f|H_I'(t_2)|j\rangle\langle j|H_I'(t_1)|g\rangle e^{i\omega_g(t_1-t_0)}$$

$$= (i\hbar)^{-2}\int_{t_0}^{t} dt_2 \mu_{fj}E(t_1)e_j^{-i\omega_j(t_1-t_2)}\mu_{jg}E(t_2)e^{i\omega_g(t_2-t_0)}\, e^{i\omega_g(t_1-t_0)}$$

After collecting terms for t_1 and t_2 , we can integrate over t_1 and ω_1. We also use the relations to integrate and rewrite equations:

$$2\pi\delta(\omega-\omega') = \int_{-\infty}^{\infty} e^{i(\omega-\omega')t}\, dt$$

$$\int f(t)\delta(t-a)dt = f(a)$$

At which point, we expand and sum over intermediate states, to get

$$= -\frac{i}{\hbar}\frac{1}{2\pi}\sum_j \int d\omega_2 \frac{1}{i\left(\omega_g - \omega_j + \omega_2\right)}\mu_{fj}E\left(\omega_f - \omega_g - \omega_2\right)\mu_{jg}E(\omega_2)$$

$$= -\frac{i}{\hbar}\frac{1}{2\pi}\int d\omega_2 \left\{\begin{array}{c} \frac{1}{i(\omega_2)}\mu_{fj}E(\omega-\omega_2)\mu_{jg}E(\omega_2) \\ +\frac{1}{i\left(\omega_g - \omega_e + \omega_2\right)}\mu_{fj}E(\omega-\omega_2)\mu_{jg}E(\omega_2) \\ +\frac{1}{i\left(\omega_g - \omega_f + \omega_2\right)}\mu_{fj}E(\omega-\omega_2)\mu_{jg}E(\omega_2) \end{array}\right\}$$

We now look at the contribution from the entangled fields $\langle E(\omega-\omega_2)E(\omega_2)\rangle$. The signal and idler beam are given as [4]:

$$E_1^+ = \frac{1}{\sqrt{2}}\sum_\omega e_\omega a\big(k(\omega)\big)e^{-i\omega t},$$

where the amplitude of these fields is just $A(t_+, t_{12}) = \langle 0|E_2^+E_1^+|\psi\rangle$. If filters with a central wavelength of $\Omega_s = \Omega_i$ are used, then $A(t_+, t_{12})$ can be rewritten in the following form:

$$A(t_+, t_{12}) = v(t_+)u(t_{12})w(t_+, t_{12})$$

where

$$t_+ = \frac{1}{2}(t_1 + t_2)$$

$$t_{12} = t_1 - t_2$$

$$v(t) = v_0 e_p^{-\Omega t}$$

$$u(t) = \Pi(t)$$

$$w(t, t') = \tilde{E}\left(0, t - t'\frac{D_+}{D}\right)$$

$$\Pi(t) = \begin{cases} \frac{1}{DL} \; for \; 0 < t < DL \\ 0 \qquad otherwise \end{cases}$$

The physical meaning of these terms is related to the crystal and the transit times of the signal and idler in the crystal. The signal and idler biphoton center of momentum arrive at the output face of the crystal at time t_+, and t_{12} is the between the times when the signal and idler arrive at the same face [4]. The length DL is the difference in the transit times of the signal and idler traveling through the crystal. The term, w(t,t'), contains information pertaining to the pulse width and its effect on the SPDC fields. D and D_+ are related to the group velocities of the signal and idler [4].

$$D = \frac{1}{u_o(\Omega_i)} - \frac{1}{u_e(\Omega_s)}$$

$$D_+ = \frac{1}{2}\left(\frac{1}{u_o(\Omega_i)} + \frac{1}{u_e(\Omega_s)}\right)$$

Now that all the terms have been defined, we write $A(t_+, t_{12})$ as:

$$A(t_+, t_{12}) = v_0 e^{-i\Omega_p \frac{t_1+t_2}{2}} E_p\left(\frac{t_1+t_2}{2} - (t_1 - t_2)\frac{D_+}{D}\right)\Pi(t_1 - t_2)$$

We can now plug this into our equation

$$= \sum_j \left(-\frac{i}{\hbar}\right)\mu_{fj}$$

$$\cdot e_i \int_{t_0}^{t_1} dt_2 e^{-i\omega_j(t_1-t_2)}\mu_{jg} \cdot e_s e^{-i\omega_g(t_2-t_0)} e^{i\omega_g(t_1-t_0)} v_0 \, e^{-i\Omega_p \frac{t_1+t_2}{2}} E_p\left(\frac{t_1+t_2}{2}\right.$$

$$\left. - (t_1 - t_2)\frac{D_+}{D}\right)\Pi(t_1 - t_2)$$

$$= \sum_j \left(-\frac{i}{\hbar}\right)\mu_{fj}$$

$$\cdot e_i \int_{t_0}^{t_1} dt_2 e^{-i\omega_j(t_1-t_2)}\mu_{jg} \cdot e_s e^{-i\omega_g(t_2-t_1)} v_0\, e^{-i\Omega_p \frac{t_1+t_2}{2}} E_p\left(\frac{t_1+t_2}{2}\right.$$

$$\left. -(t_1-t_2)\frac{D_+}{D}\right)\Pi(t_1-t_2)$$

$$\frac{1}{2\pi}\int d\omega_1 \sum_j \left(-\frac{i}{\hbar}\right)\mu_{fj}$$

$$\cdot e_i \int_{t_0}^{t_1} dt_2 e^{-i\omega_j(t_1-t_2)}\mu_{jg}$$

$$\cdot e_s e^{-i\omega_g(t_2-t_1)} v_0\, e^{-i\Omega_p \frac{t_1+t_2}{2}} E_p(\omega_1) e^{-i\omega_1\left(\frac{t_1+t_2}{2}-(t_1-t_2)\frac{D_+}{D}\right)}\Pi(t_1-t_2)$$

Reorganizing terms:

$$\frac{1}{2\pi}\int d\omega_1 \sum_j \left(-\frac{i}{\hbar}\right)\mu_{fj}$$

$$\cdot e_i \int_{t_0}^{t_1} dt_2 e^{i(\omega_g-\omega_j-\frac{\Omega_p}{2}-\frac{\omega_1}{2}+\frac{\omega_1 D_+}{D})t_1}\mu_{jg}$$

$$\cdot e_s v_0\, E_p(\omega_1) e^{i(\omega_j-\omega_g-\frac{\Omega_p}{2}-\frac{\omega_1}{2}-\frac{\omega_1 D_+}{D})t_2}\Pi(t_1-t_2)$$

If we integrate over t_1 and ω_1, and sum over intermediate states the equation becomes:

$$\frac{1}{2\pi}\sum_j \left(-\frac{i}{\hbar}\right) v_0 E_p(\omega-\Omega_p)\frac{1-e^{-i\left(-\frac{\omega}{2}-\frac{\Omega_{pD_+}}{2}+\frac{\omega_1 D_+}{D}\right)T_e}}{\left(-\frac{\omega}{2}-\frac{\Omega_{pD_+}}{2}+\frac{\omega_1 D_+}{D}\right)T_e}\mu_{fg}\cdot e_i\mu_{gg}\cdot e_s$$

$$+\frac{1-e^{-i\left(\omega_g-\omega_e-\frac{\omega}{2}-\frac{\Omega_{pD_+}}{2}+\frac{\omega_1 D_+}{D}\right)T_e}}{\left(\omega_g-\omega_e-\frac{\omega}{2}-\frac{\Omega_{pD_+}}{2}+\frac{\omega_1 D_+}{D}\right)T_e}\mu_{fe}\cdot e_i\mu_{eg}\cdot e_s$$

$$+\frac{1-e^{-i\left(\omega_g-\omega_f-\frac{\omega}{2}-\frac{\Omega_{pD_+}}{2}+\frac{\omega_1 D_+}{D}\right)T_e}}{\left(\omega_g-\omega_f-\frac{\omega}{2}-\frac{\Omega_{pD_+}}{2}+\frac{\omega_1 D_+}{D}\right)T_e}\mu_{ff}\cdot e_i\mu_{fg}\cdot e_s$$

This is similar to the form of the entangled two-photon transition probability amplitude that is given in Fei et al [4] given below.

$$S_{fi}$$

$$=\frac{\pi N l}{2A_q}\sqrt{\omega_1^0\omega_2^0}exp\left[-\frac{(\varepsilon_f-\varepsilon_i-\omega_p)^2}{\Delta\omega_p^2}\right]$$

$$\times\sum_j\left\{\begin{array}{l} D_{21}^{(j)}\dfrac{1-exp\{T_e(\varepsilon_j-\varepsilon_i-\omega_1^0)+(T_0-T_e/2)(\varepsilon_f-\varepsilon_i-\omega_1^0-\omega_2^0)-iT_e\kappa_j/2\}}{T_e(\varepsilon_j-\varepsilon_i-\omega_1^0)+(T_0-T_e/2)(\varepsilon_f-\varepsilon_i-\omega_1^0-\omega_2^0)-iT_e\kappa_j/2} \\ +D_{12}^{(j)}\dfrac{1-exp\{T_e(\varepsilon_j-\varepsilon_f-\omega_1^0)-(T_0-T_e/2)(\varepsilon_f-\varepsilon_i-\omega_1^0-\omega_2^0)-iT_e\kappa_j/2\}}{T_e(\varepsilon_j-\varepsilon_f-\omega_1^0)-(T_0-T_e/2)(\varepsilon_f-\varepsilon_i-\omega_1^0-\omega_2^0)-iT_e\kappa_j/2}\end{array}\right\}$$

From this probability amplitude the cross-section can be calculated as such

$$\sigma_e=\left|S_{fi}\right|^2A_q^2/A_e$$

Like our equation this equation is also complicated, however with a few assumptions it can be simplified. The simplified non-modified entangled two-photon absorption cross-section equation is given below.

$$\sigma_e=\frac{\pi}{4A_eT_e}\omega_1^0\omega_2^0\delta(\varepsilon_f-\varepsilon_i-\omega_1^0-\omega_2^0)$$

$$\times\left|\sum_j D_{21}^{(j)}\frac{1-exp\left[-iT_e\Delta_1^j-\frac{T_e\kappa_j}{2}\right]}{\Delta_1^j-\frac{i\kappa_j}{2}}-D_{21}^{(j)}\frac{1-exp\left[-iT_e\Delta_1^j-\frac{T_e\kappa_j}{2}\right]}{\Delta_1^j-\frac{i\kappa_j}{2}}\right|^2$$

The modified ETPA equation can be simplified as [5]:

$$\sigma_e = \frac{A}{\hbar^2 \varepsilon_0^2 A_e T_e} \omega_0^2 \delta(\varepsilon_f - \varepsilon_g - 2\omega_0) \left| \frac{1 - e^{-i(\omega_0 + \varepsilon_g - \varepsilon_e)T_e - \kappa_e T_e/2}}{(\omega_0 + \varepsilon_g - \varepsilon_e) - i\kappa_e/2} \mu_{fe} \cdot e_i \mu_{eg} \cdot e_s \right.$$
$$\left. + \frac{1 - e^{-i\omega_0 T_e - \kappa_g T_e/2}}{\omega_0 - i\kappa_g/2} \mu_{fg} \cdot e_i \mu_{gg} \cdot e_s + \frac{1 - e^{i\omega_0 T_e - \kappa_f T_e/2}}{-\omega_0 - i\kappa_f/2} \mu_{ff} \cdot e_i \mu_{fg} \cdot e_s \right|^2$$

References:

[1] H. B. Bebb and A. Gold, "Multiphoton Ionization of Hydrogen and Rare-Gas Atoms," *Physical Review,* vol. 143, pp. 1-24, 03/04/ 1966.

[2] W. J. Meath and E. A. Power, "On the importance of permanent moments in multiphoton absorption using perturbation theory," *Journal of Physics B: Atomic and Molecular Physics,* vol. 17, p. 763, 1984.

[3] M. Richter, "Modified Entangled Two-Photon Absorption Cross-Section," ed, 2009, p. 8.

[4] T. E. Keller and M. H. Rubin, "Theory of two-photon entanglement for spontaneous parametric down-conversion driven by a narrow pump pulse," *Physical Review A,* vol. 56, pp. 1534-1541, 08/01/ 1997.

[5] L. Upton, M. Harpham, O. Suzer, M. Richter, S. Mukamel, and T. Goodson, III, "Optically Excited Entangled States in Organic Molecules Illuminate the Dark," *Journal of Physical Chemistry Letters,* vol. 4, pp. 2046-2052, Jun 20 2013.